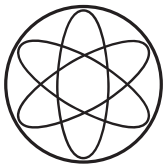

In-Trap Decay Spectroscopy for $\beta\beta$ Decays

Dissertation
von

Thomas Brunner

Lehrstuhl E12 für Experimentalphysik

Technische Universität München

Technische Universität München
Physik-Department E12

In-Trap Decay Spectroscopy for $\beta\beta$ Decays

Thomas Brunner

Vollständiger Abdruck der von der Fakultät für Physik der Technischen Universität München zur Erlangung des akademischen Grades eines

Doktors der Naturwissenschaften (Dr. rer. nat.)

genehmigten Dissertation.

Vorsitzender:	Univ.-Prof. Dr. A. Ibarra
Prüfer der Dissertation:	
	1. Univ.-Prof. Dr. R. Krücken
	2. Univ.-Prof. Dr. P. Fierlinger

Die Dissertation wurde am 14.12.2010 bei der Technischen Universität München eingereicht und durch die Fakultät für Physik am 18.01.2011 angenommen.

Zusammenfassung

Im Rahmen dieser Arbeit wurde am TRIUMF in Vancouver, Kanada, eine neue Methode entwickelt, die zum Ziel hat, Elektroneneinfangintensitäten (ECBR) von Übergangskernen in $\beta\beta$ Zerfällen zu bestimmen. Diese Messung trägt zum tieferen Verständnis der dem $\beta\beta$ Zerfall zu Grunde liegenden Kernphysik bei.

Die neuartige Methode verwendet eine Penning-Ionenfallen des TITAN (TRIUMF's Ion Traps for Atomic and Nuclear science) Experiments für die Zerfallsspektroskopie. Hierbei werden radioaktive Ionen in der Ionenfalle gespeichert und deren radioaktive Zerfälle beobachtet. Das starke Magnetfeld der Falle führt die aus β Zerfällen stammenden Elektronen entlang der Feldlinien aus der Falle, während einem Elektroneneinfang folgende Röntgenstrahlen isotrop abgestrahlt werden. Dies ermöglicht eine räumliche Trennung von Röntgen- und β Detektion, wobei es für die Elektronen aufgrund des starken magnetischen Feldes nicht möglich ist, den Röntgendetektor zu erreichen. Dies ermöglicht es, sehr schwache ECBR zu messen. Zudem werden die Ionen in der Falle gespeichert, ohne sie in ein Trägermaterial zu implantieren. Dadurch werden die emittierten Röntgenquanten nicht zusätzlich abgeschwächt. Dies, und die räumliche Trennung von β und Röntgendetektion, bieten deutliche Vorteile gegenüber herkömmlichen Methoden.

Diese Methode wurde im Rahmen dieser Arbeit implementiert und deren Machbarkeit wurde mit der Messung der Elektroneneinfangverzweigungsverhältnisses von ^{107}In und ^{124}Cs demonstriert. Im Fall von ^{124}Cs wurde ^{126}Cs während des selben Experimentes gemessen. Die gemessenen Röntgenintensitäten von ^{126}Cs wurden dann verwendet, um die Nachweiseffizienz des Röntgendetektors zu bestimmen. Hierbei wurden bis zu $2.65(32) \cdot 10^5$ Ionen pro Puls in der Falle gespeichert und deren Zerfall beobachtet. Die gemessene Intensität des Elektroneneinfanges bei ^{124}Cs beträgt $(17.8 \pm 2.5(\text{stat.}) \pm 15(\text{syst.}))\%$ und stimmt mit dem Literaturwert von 10(9)% [NND10] überein. Durch unterschiedliche Impedanzen von Vorverstärker und Datenaufnahme ergibt sich die systematische Unsicherheit von 15%. Trotzdem konnte der statistische Fehler um einen Faktor drei reduziert werden. Während dieser Messungen wurde das erste Mal ein Elektroneneinfang an Kernen gemessen, die in einer Penningfalle gespeichert waren. Durch diese erfolgreichen Messungen wurde demonstriert, dass die Zerfallsspektroskopie an in einer Penningfalle gespeicherten Ionen möglich ist und in zukünftigen Messungen die Elektroneneinfangintensitäten von Übergangskernen in $\beta\beta$ Zerfällen gemessen werden können.

Abstract

The presented work describes the implementation of a new technique to measure electron-capture (EC) branching ratios (BRs) of intermediate nuclei in $\beta\beta$ decays. This technique has been developed at TRIUMF in Vancouver, Canada. It facilitates one of TRIUMF's Ion Traps for Atomic and Nuclear science (TITAN), the Electron Beam Ion Trap (EBIT) that is used as a spectroscopy Penning trap.

Radioactive ions, produced at the radioactive isotope facility ISAC, are injected and stored in the spectroscopy Penning trap while their decays are observed. A key feature of this technique is the use of a strong magnetic field, required for trapping. It radially confines electrons from β decays along the trap axis while x-rays, following an EC, are emitted isotropically. This provides spatial separation of x-ray and β detection with almost no β-induced background at the x-ray detector, allowing weak EC branches to be measured. Furthermore, the combination of several traps allows one to isobarically clean the sample prior to the in-trap decay spectroscopy measurement.

This technique has been developed to measure ECBRs of transition nuclei in $\beta\beta$ decays. Detailed knowledge of these electron capture branches is crucial for a better understanding of the underlying nuclear physics in $\beta\beta$ decays. These branches are typically of the order of 10^{-5} and therefore difficult to measure. Conventional measurements suffer from isobaric contamination and a dominating β background at the x-ray detector. Additionally, x-rays are attenuated by the material where the radioactive sample is implanted. To overcome these limitations, the technique of in-trap decay spectroscopy has been developed.

In this work, the EBIT was connected to the TITAN beam line and has been commissioned. Using the developed beam diagnostics, ions were injected into the Penning trap and systematic studies on injection and storage optimization were performed. Furthermore, Ge detectors, for the detection of x-rays, were tested and installed. Several β detectors were tested and mounted on especially designed holders. The feasibility of the in-trap decay spectroscopy technique has been demonstrated by successfully measuring the EC branching ratios of ^{107}In and ^{124}Cs. In the latter case, ^{126}Cs was measured at the same time as ^{124}Cs and used to calibrate the detection efficiency of the x-ray detector. During this measurement, up to $2.65(32) \cdot 10^5$ ions/bunch were stored in the trap while their decays were observed. Based on this measurement, the ECBR of ^{124}Cs was determined to be $(17.8 \pm 2.5(\text{stat.}) \pm 15(\text{syst.}))\%$. The large systematic uncertainty arises from an impedance mismatch between preamplifier and x-ray detector that was discovered after the experiment. Nevertheless, the new value agrees with the literature value of 10(9)% [NND10] and the statistical error was reduced by a factor of three. These measurements demonstrated the feasibility of this new method of in-trap decay spectroscopy. It was for the first time that an electron capture decay was observed of ions stored in a Penning trap. In the future, this technique will be applied to perform ECBR measurements of transition nuclei in double beta decays.

Contents

List of Figures

List of Tables

Chapter 1

Introduction and Theoretical Description

The Standard Model of particle physics (SM) is very well established and explains the existence and relations of all known elementary particles. However, among all particle groups one of the most mysterious known particles is the neutrino ν. It was first introduced by Pauli as a massless particle in order to preserve energy and momentum conservation in β decays. Within the SM of particle physics, the neutrino is a massless lepton existing in three distinct flavors ν_e, ν_μ, and ν_τ. Recent experiments have found evidence for neutrino oscillations in atmospheric, solar, reactor, and accelerator-produced neutrinos [Wal04]. These oscillations are only possible if the neutrino has mass. However, these oscillation experiments can only provide $\left|\Delta m^2\right|$, the squared mass difference of the neutrino mass eigenstates. They can determine neither the absolute neutrino mass scale nor the character of the neutrino, i.e., whether the neutrino is a Dirac or Majorana particle. If the neutrino is a Majorana particle it is identical with its anti-particle.

This recent evidence, that neutrinos are massive particles, increased interest in the neutrino less double β decay ($0\nu\beta\beta$). It is forbidden within the SM as it violates lepton number conservation. If this decay is observed, the neutrino is its own anti-particle and thus a Majorana particle. Then, the effective Majorana neutrino mass $\langle m_{\beta\beta}\rangle$ could be deduced from the half life of the decay,

$$\left(T^{0\nu}_{1/2}\right)^{-1} = G^{0\nu}(Q,Z)\left|M^{0\nu}\right|^2\langle m_{\beta\beta}\rangle^2\,, \tag{1.1}$$

with $G^{0\nu}(Q,Z)$ being the phase space factor in $\mathrm{y}^{-1}\mathrm{eV}^{-2}$, and $M^{0\nu}$ the nuclear matrix element (NME). This relation is only true if the neutrino is a light particle and no other process beyond the SM contributes to the decay. The phase space factor $G^{0\nu}(Q,Z)$ is well understood. However, the NME $M^{0\nu}$ is purely based on theoretical calculations. Depending on the theoretical model applied, calculated $M^{0\nu}$ vary by a factor of 2-3. Thus, in order to be able to extract an accurate effective neutrino mass from the $0\nu\beta\beta$ decay half life, it is necessary to better confine $M^{0\nu}$. Additional insight on this subject can be gained from the SM-allowed and observed $2\nu\beta\beta$ decay which allows one to test the underlying nuclear physics. The transition via $2\nu\beta\beta$ is described by $M^{2\nu}$ and is dominated by intermediate 1^+ states. A deeper understanding of the nuclear physics

in theoretical $\beta\beta$ decay models can be gained by measuring the decay branches of the short-lived ($T_{1/2} < 1\,\mathrm{h}$) intermediate nuclei in $\beta\beta$ decays, as this measurement directly determines parts of the $2\nu\beta\beta$ decay transition matrix element $M^{2\nu}$. In special cases, where a so-called single-state dominance (SSD) [Aba84] is present, the transition via the lowest 1^+ state accounts for the whole matrix element $M^{2\nu}$.

The scope of the present work is the development and implementation of a new and independent technique to measure these branching ratios (BRs) in intermediate short-lived $\beta\beta$ decay transition nuclei; in particular, the electron-capture (EC) branch to the $\beta\beta$ decay mother isotope. A difficulty for conventional measurements is the fact that this branch is typically of the order 10^{-5}. Due to its signature, the emission of an x-ray, and background from the dominating β decay, this branch is difficult to measure. A key feature of the developed technique within this work is the use of a strong magnetic field to spatially separate x-ray and β detection. The strong magnetic field is provided by a Penning trap where the ions are stored backing free, i.e., without the implantation into a backing material, while their decays are observed.

The feasibility of this technique has been proven in two measurement campaigns with radioactive ^{107}In and ^{124,126}Cs at the TITAN Penning trap setup located at the ISAC radioactive beam facility at TRIUMF, Vancouver, Canada. These isotopes were chosen because of their large electron capture branching ratios (ECBRs) which allowed for systematic investigations. During these measurements, ECBRs were determined for the first time on ions stored in a Penning trap.

This chapter provides an introduction to neutrino physics and discusses the difficulties in calculating $M^{0\nu}$. Chapter 2 presents the TITAN setup at TRIUMF. The developed technique to measure ECBRs is implemented in one of TITAN's ion traps, the spectroscopy Penning trap. This spectroscopy Penning trap is introduced in detail in Chapter 3, while Chapter 4 presents systematic studies that were performed in order to optimize the system. The measurement of ECBRs in ^{107}In and ^{124,126}Cs is summarized in Chapter 5. The obtained results and feasibility of ECBR measurements of intermediate nuclei in $\beta\beta$ decays applying the developed technique are discussed in Chapter 6.

1.1 The neutrino in modern physics

The neutrino provides one of the great challenges of modern physics. Its existence was first suggested by Wolfgang Pauli in his letter titled 'Liebe Radioactive Damen und Herren' (eng: 'Dear Radioactive Ladies and Gentlemen') [Pau30] dated December 4, 1930. In his letter, Pauli proposed that a neutral particle with spin 1/2 and no larger than 1% of the proton mass is emitted during β decays. Such a particle was postulated to save the laws of angular momentum and energy conservation. Four years later,

Enrico Fermi included this particle into his successful theory of β decay and called it the neutrino [Fer34]. Nevertheless, it took another 19 years before this neutrino was first observed experimentally by Reines and Cowan in 1953. They detected anti-neutrinos $\overline{\nu}_e$ produced at the Savannah River Plant, SC, USA, in a water tank surrounded by scintillators [Cow56]. The anti-neutrino was detected by the reaction of an inverse β decay

$$\overline{\nu}_e + \mathrm{p} \rightarrow \mathrm{n} + \mathrm{e}^+. \tag{1.2}$$

To enhance the signature of an anti-neutrino event, ^{113}Cd, which has a high neutron-capture cross section, was added to the water. The neutron created in the inverse β decay, was captured by ^{113}Cd and produced γ rays in the reaction

$$\mathrm{n} + ^{113}\mathrm{Cd} \rightarrow ^{114}\mathrm{Cd}^* \rightarrow ^{114}\mathrm{Cd} + \gamma. \tag{1.3}$$

The observation of this reaction proved the existence of neutrinos. Moreover, the non-observation of the process $\overline{\nu}_\mathrm{e} + ^{37}\mathrm{Cl} \rightarrow ^{37}\mathrm{Ar} + \mathrm{e}^-$ [Dav55] verified that ν_e and $\overline{\nu}_\mathrm{e}$ are distinct particles.

Within the SM, the neutrino is a mass less particle existing in three flavor eigenstates ν_e, ν_μ and ν_τ. However, the neutrino-oscillation experiments SuperKamiokande [Fuk98, Fuk01, Ash04], SNO [Ahm01, Ahm02], KamLAND [Egu03], MINOS [Mic06], and K2K [Ahn06] provided experimental evidence of neutrino oscillations, i.e., the oscillation of one neutrino flavor into another. These oscillations are only possible if the neutrino is a massive particle. In the two-neutrino form, the oscillation probability can be expressed by [Nak10]

$$P\left(\nu_a \rightarrow \nu_b\right) = \sin^2(2\theta)\, \sin^2\left(\Delta m^2\, L/4\, E\right) \tag{1.4}$$

where θ is the mixing angle, E the neutrino's kinetic energy, and L the travel distance of the neutrino. With the observation of ν oscillations, a new era of 'Physics beyond the Standard Model' [Kuo89] had begun.

The definite neutrino flavor eigenstates $\nu_e,\ \nu_\mu$ and ν_τ differ from the neutrino mass eigenstates $\nu_1,\ \nu_2$, and ν_3. Similar to the CKM matrix in the quark sector, these eigenstates are transformed into each other by the so-called Pontecorvo-Maki-Nagagawa-Sakata (PMNS) matrix [Pon67,Mak62]. The three generation eigenstates are connected to the mass eigenstates via

$$\begin{pmatrix} \nu_e \\ \nu_\mu \\ \nu_\tau \end{pmatrix} = \begin{pmatrix} U_{e_1} & U_{e_2} & U_{e_3} \\ U_{\mu_1} & U_{\mu_2} & U_{\mu_3} \\ U_{\tau_1} & U_{\tau_2} & U_{\tau_3} \end{pmatrix} \begin{pmatrix} \nu_1 \\ \nu_2 \\ \nu_3 \end{pmatrix}, \tag{1.5}$$

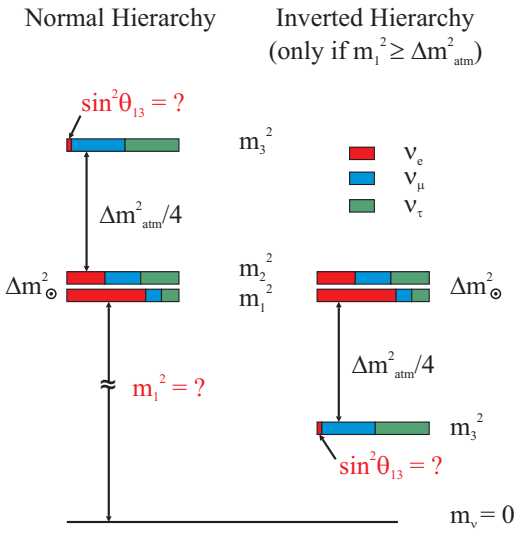

Figure 1.1: The schematic shows the neutrino mass eigenstates m_i as a composition of the neutrino flavor eigenstates. The absolute mass scale is unknown as long as m_1^2 remains unknown.

with U being the PMNS matrix. The latter is a unitary matrix and thus can be written as (see for example [Car09, Nak10])

$$U = \underbrace{\begin{pmatrix} 1 & 0 & 0 \\ 0 & c_{23} & s_{23} \\ 0 & -s_{23} & c_{23} \end{pmatrix}}_{\text{I}} \underbrace{\begin{pmatrix} c_{13} & 0 & s_{13}e^{-i\delta} \\ 0 & 1 & 0 \\ -s_{13}e^{i\delta} & 0 & c_{13} \end{pmatrix}}_{\text{II}} \underbrace{\begin{pmatrix} c_{12} & s_{12} & 0 \\ -s_{12} & c_{12} & 0 \\ 0 & 0 & 1 \end{pmatrix}}_{\text{III}} \underbrace{\begin{pmatrix} e^{i\alpha_1/2} & 0 & 0 \\ 0 & e^{i\alpha_2/2} & 0 \\ 0 & 0 & 1 \end{pmatrix}}_{\text{IV}}, \quad (1.6)$$

where $c_{ij} = \cos\theta_{ij}$ and $s_{ij} = \sin\theta_{ij}$, with the three mixing angles θ_{12}, θ_{23} and θ_{13}. If neutrino oscillation violates CP symmetry, the phase factor δ is non-zero. The factors α_1 and α_2 are so-called Majorana phases and require the neutrino to be a Majorana particle. However, they do not contribute to oscillation phenomena regardless of the neutrino's nature. Part I of the PMNS matrix in Eq. (1.6) is determined from atmospheric neutrino oscillation and long baseline disappearance measurements, while part II is extracted from short baseline reactor and long baseline accelerator experiments. Part III is determined based on the measurement of solar neutrino oscillations and

$\sin^2(2\,\theta_{12})$	$=$	0.87 ± 0.03
Δm^2_{21}	$=$	$(7.59 \pm 0.20) \cdot 10^{-5}\,\mathrm{eV}^2$
$\sin^2(2\,\theta_{23})$	$>$	0.92
Δm^2_{32}	$=$	$(2.43 \pm 0.13) \cdot 10^{-3}\,\mathrm{eV}^2$
$\sin^2(2\,\theta_{13})$	$<$	0.15, CL $= 90\%$

Table 1.1: Most recent values of θ_{ij} and Δm^2 deduced from oscillation experiments [Nak10].

long baseline reactor oscillations. A description of various experiments and the neutrino eigenstate mixing is presented for example in [Abe08, Les08, Nak10]. The latest values of θ_{ij} and Δm^2_{ij} are presented in Table 1.1. The parameters known from oscillation experiments are displayed in Fig. 1.1 together with the unknown ones. Since only Δm^2_{ij} is determined in oscillation experiments, three scenarios of mass hierarchy are possible, namely normal, inverted and degenerate hierarchy. The neutrino mass hierarchy as well as their absolute mass scale remain unknown in oscillation experiments. Both, normal and inverted hierarchy, are displayed in Fig. 1.1. Also, the nature of the neutrino, i.e., whether it is a Dirac or Majorana particle, cannot be determined in oscillation experiments.

The measurement of β decay end-point energies is a direct measurement of the electron neutrino's mass. Typically, tritium ($T_{1/2} = 12.32(2)\,\mathrm{y}$ [NND10]) is the isotope of choice because of its low Q value of 18.6 keV. Furthermore, it consists of only three nucleons and therefore nuclear corrections in the decay are well understood. Previous β end-point measurements provided an upper limit of $m_{\nu_e} < 2\,\mathrm{eV}$ [Yao06, Ott08]. A new spectrometer, KATRIN, is currently being built and expected to be operational soon. The KATRIN experiment is aiming at a resolution limit of 200 meV. A review on KATRIN is given in [Ott08, Ott10]. These end-point energy measurements are sensitive to the electron neutrino mass but are insensitive to the character of the neutrino.

A different approach to determine the absolute neutrino mass is the search for $0\nu\beta\beta$ decays. The Feynman diagrams of both $2\nu\beta\beta$ and $0\nu\beta\beta$ decay are illustrated in Fig. 1.2. An experimental observation of this decay would determine:

- a lepton number non-conservation,

- the nature of the neutrino being a Majorana particle,

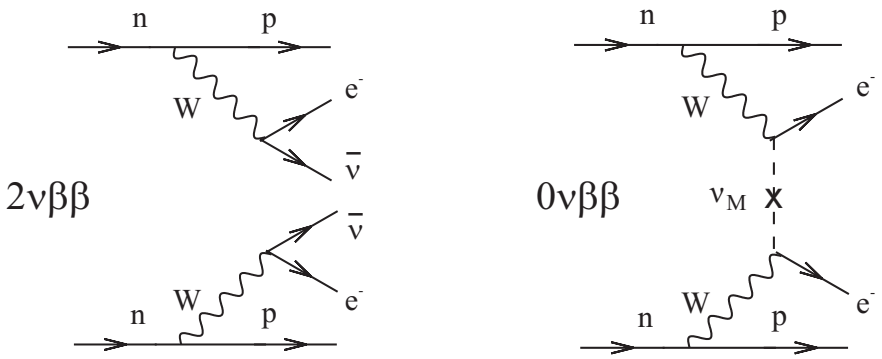

Figure 1.2: Feynman diagrams of $2\nu\beta\beta$ and $0\nu\beta\beta$ decay.

- the effective Majorana neutrino mass

$$\langle m_{\beta\beta} \rangle = \left| \sum_i U_{e_i}^2 \, m_i \right| , \tag{1.7}$$

  in terms of the mixing matrix elements U_{e_i}, the corresponding mass eigenvalues m_i, and the so-called Majorana phases α_i in U_{e_i},

- and the neutrino mass hierarchy, i.e., normal, inverted or degenerate hierarchy.

Based on constraints from oscillation experiments, certain $\langle m_{\beta\beta} \rangle$ can be excluded in Eq.(1.7). Fig. 1.3 illustrates allowed $\langle m_{\beta\beta} \rangle$ regions dependent on the lightest neutrino mass eigenstate m_{min}.

A worldwide search for $0\nu\beta\beta$ decays is ongoing. One positive observation is claimed for the isotope ^{76}Ge by part of the Heidelberg-Moscow Collaboration [KK04, KK06]. However, this claim is controversial and not accepted by the '2β-decay community' (see footnote in [Bar10a]). In the following section, $\beta\beta$ decay and its implications are presented. Additional information can be found in [Hax84,Doi85,Avi08,Vog08,Bar10a], as well as in several books, for example 'Neutrino Physics' [Zub04].

1.2 Double beta decay and its implications

Double beta ($\beta\beta$) decay is a second order weak process, in which the proton number Z changes by two units while the mass A stays constant. The condition for the appearance of $\beta\beta$ decays is nicely illustrated by the Weizsäcker mass formula [vW35]. This formula determines the Z-dependence of the nuclear mass $M_A(Z, A)$ and thus whether a nucleus

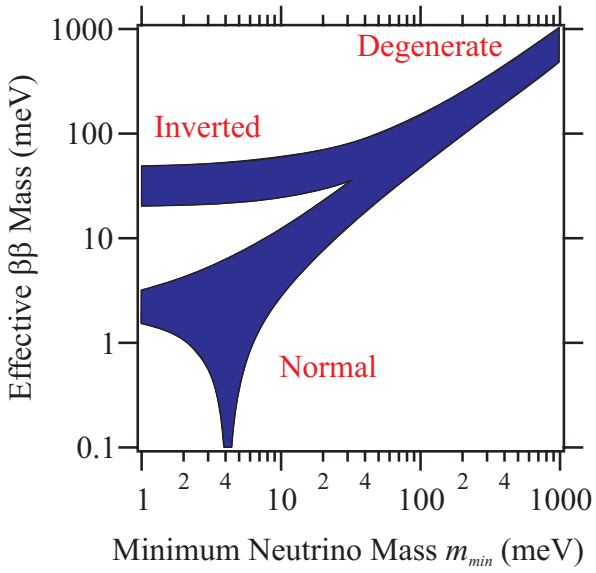

Figure 1.3: Effective $\langle m_{\beta\beta} \rangle$ as a function of the lightest mass eigenstate m_{min}. Graph from [Avi08].

close to stability is stable or will undergo β decay. The nuclear mass is determined by

$$M_A(Z,A) = constant + a_{sym}\frac{(A/2-Z)^2}{A} + a_{Coul}\frac{Z^2}{A^{1/3}} + m_e Z + \delta_P, \tag{1.8}$$

with the symmetry energy coefficient $a_{sym} = 93.15\,\text{MeV}$, the Coulomb energy coefficient $a_{Coul} = 0.714\,\text{MeV}$ [Pov04], and the effect of the pairing force δ_P [Boh75]:

$$\delta_P \approx \begin{cases} -12\,\text{MeV}\,A^{-1/2} & \text{for even-even nuclei,} \\ 0 & \text{for even-odd and odd-even nuclei,} \\ +12\,\text{MeV}\,A^{-1/2} & \text{for odd-odd nuclei.} \end{cases} \tag{1.9}$$

For isobars with odd A, the pairing term in Eq. (1.8) vanishes and $M_A(Z,A)$ is described by a parabola with typically only one stable isotope for a given A. In the case of even A, two parabolae exist shifted by $\pm\delta_P$ from the odd A parabola. These two parabolae are displayed in Fig. 1.4 for the $A = 136$ isobars.

Double β decay takes place in cases where single β decay is either energetically forbidden, i.e., when

$$M(Z,A) > M(Z+2,A) \text{ and } M(Z,A) < M(Z+1,A), \tag{1.10}$$

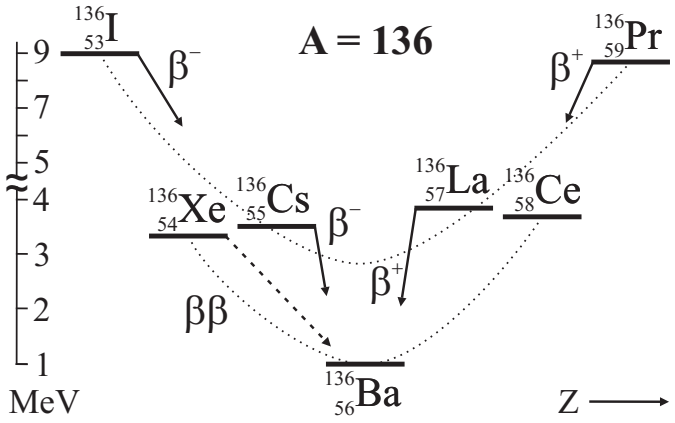

Figure 1.4: Atomic masses of the isotopes with mass $A = 136$. For the nuclei ^{136}Ce and ^{136}Xe, ordinary β decay is energetically not possible. However, $\beta\beta$ decay to the daughter isotope ^{136}Ba is possible.

or strongly suppressed by a large spin difference of the involved nuclear states such as for ^{48}Ca. Typically, $\beta\beta$ decays are $0^+ \rightarrow 0^+$ transitions from the ground state of the mother nucleus to the ground state of the daughter. Only in the cases of ^{100}Mo and ^{150}Nd $2\nu\beta^-\beta^-$ decay, transitions to the first excited 0^+ state have also been observed [Vog08, Bar10a].

Double β^- decays of neutron-rich isotopes provide the motivation for this work. Therefore if not stated otherwise, $\beta\beta$ refers to $\beta^-\beta^-$ decays. It is expected to happen in at least two modes: the two neutrino $\beta\beta$ decay and the neutrino less $\beta\beta$ decay. Both cases are explained in the following sections and reviews on this topic are presented in [Hax84, Doi85, Suh98, Ell02].

Other exotic decay mechanisms beyond the SM are also discussed in literature but exceed the scope of this thesis. Ref. [Bar10a] discusses one possible alternative decay, $0\nu\chi^0\beta\beta$, that requires the existence of a Majoron χ^0. The reader is referred to this article and references therein.

1.2.1 Two neutrino double beta decay

The decay mode via the simultaneous but uncorrelated decay of two neutrons in a nucleus, i.e., $2\nu\beta\beta$ decay, was first suggested by Goeppert-Mayer in 1935 [GM35] with the process

$$(Z, A) \rightarrow (Z + 2, A) + 2e^- + 2\overline{\nu}_e. \tag{1.11}$$

This second-order weak interaction is allowed within the SM as it conserves lepton number. The transition rate is proportional to G_F^4 and as a consequence, extremely slow. Such a transition was first observed in the $2\nu\beta\beta$ decay of ^{82}Se in geochemical experiments (see [Mar85] for a review of geochemical experiments), and later confirmed by the direct observation of the decay in a time-projection chamber with a half life of $T_{1/2} = 1.1^{+0.8}_{-0.3} \cdot 10^{20}$ y (68% confidence level) [Ell87]. Since then, it has also been observed in other isotopes with half lives typically on the order of 10^{20} years. Besides proton decay, this decay is among the rarest on earth [Zub04]. A list of observed $2\nu\beta\beta$ decay half lives is presented in Table 1.2.

The $2\nu\beta\beta$ decay rate is derived starting from Fermi's Golden Rule for second order weak transitions:

$$\lambda_{2\nu} = \frac{2\pi}{\hbar} \left| M^{2\nu} \right|^2 \delta \left(E_f - E_i \right), \tag{1.12}$$

where the delta function takes into account that the transition happens to discrete energy levels and the matrix element $M^{2\nu}$ connects the initial and final energy states E_i and E_f, respectively. The matrix element is the sum of all transitions via intermediate states m in the transition nucleus, and is given by

$$M^{2\nu} = \sum_m \frac{\langle f | H_{if} | m \rangle \langle m | H_{if} | i \rangle}{E_i - E_m}, \tag{1.13}$$

with H_{if} being the weak Hamiltonian operator. In the latter equation, one has to take into account that the electron-neutrino combinations in the intermediate step cannot be distinguished. Therefore, one has to sum over all possible configurations, $E_m = E_{Nm} + E_{e_a} + E_{\nu_b}$, of the energy of the intermediate state E_{Nm}, the electron energy E_{e_a} and the neutrino energy E_{ν_b} of leptons $a, b = \{1, 2\}$ [Zub04]. Based on Eq.(1.12) and Eq.(1.13) and applying the Primakoff-Rosen approximation [Pri59] to simplify the Fermi function, one obtains the electron spectrum of both electrons [Zub04]:

$$\frac{\mathrm{d}N}{\mathrm{d}K} \approx K \left(Q - K \right)^5 \left(1 + 2K + \frac{4K^2}{3} + \frac{K^3}{3} + \frac{K^4}{30} \right), \tag{1.14}$$

with $K = T_{e_1} + T_{e_2}$ and Q being the sum of both electrons' kinetic energy and Q value, respectively, in units of the electron mass. The decay rate can be approximated by [Zub04]

$$\lambda_{2\nu} \approx Q^7 \left(1 + \frac{Q}{2} + \frac{Q^2}{9} + \frac{Q^3}{90} + \frac{Q^4}{1980} \right). \tag{1.15}$$

This rate and the total electron energy spectrum in Eq.(1.14) are independent of the charge Z of the isotopes involved, depending only on the energy Q released in the decay. It is noted that the decay rate scales with Q^{11}.

The half life of this decay can be expressed by the phase space factor $G^{2\nu}(Q,Z)$ and the matrix elements $M^{2\nu}_{GT}$ and $M^{2\nu}_{F}$ in the form

$$\left(T^{2\nu}_{1/2}\right)^{-1} = G^{2\nu}(Q,Z)\left|M^{2\nu}_{GT} + \frac{g_V^2}{g_A^2}M^{2\nu}_{F}\right|^2 . \tag{1.16}$$

The involved Gamow-Teller and Fermi matrix elements are

$$M^{2\nu}_{GT} = \sum_j \frac{\langle 0^+_f|\tau\sigma|1^+_j\rangle\langle 1^+_j|\tau\sigma|0^+_i\rangle}{E_j + Q/2 + m_e - E_i}\,, \text{ and} \tag{1.17}$$

$$M^{2\nu}_{F} = \sum_j \frac{\langle 0^+_f|\tau|1^+_j\rangle\langle 1^+_j|\tau|0^+_i\rangle}{E_j + Q/2 + m_e - E_i}\,, \tag{1.18}$$

with $\tau\sigma$ and τ being the Gamow-Teller and Fermi interaction, respectively. Fermi transitions in $2\nu\beta\beta$ are strongly suppressed due to selection rules and $M^{2\nu}_{GT}$ in Eq.(1.17) dominantly contributes to Eq.(1.16). Selection rules only allow transitions via virtual 1^+ states in the intermediate nuclei. The above equations and their derivations are presented in Ref. [Zub04].

1.2.2 Neutrino less double beta decay

Another possible $\beta\beta$ decay mode is the lepton number violating decay without the emission of any neutrino, the neutrino less double beta decay $0\nu\beta\beta$. This decay mode is forbidden in the SM as it changes the lepton number by two units. In this transition two correlated neutrons decay via

$$(Z,A) \rightarrow (Z+2,A) + 2\mathrm{e}^-. \tag{1.19}$$

This decay was first suggested by Furry [Fur39] after Majorana published a paper on two-component neutrinos [Maj37]. A positive observation of this decay would imply that the neutrino is a massive Majorana particle, independent of the processes involved [Sch82, Tak84]. This is called Schechter-Valle theorem and is illustrated in Fig. 1.5. In fact, an experimental observation of any lepton number violation process would require the neutrino to be a Majorana particle (see for example [Vog08]). The decay rate of $0\nu\beta\beta$ can be estimated by [Zub04]

$$\lambda_{0\nu} \propto \left(\frac{Q^5}{30} - \frac{2Q^2}{3} + Q - \frac{2}{5}\right) \tag{1.20}$$

and is proportional to Q^5. Compared to the $2\nu\beta\beta$ rate this decay would be enhanced by about Q^6 but $0\nu\beta\beta$ is highly suppressed due to its lepton number violating nature.

Nuclide	Transition	Q-value [keV]	Nat. ab. [%]	$\left(G^{0\nu}\right)^{-1}$ [y]	$\left(G^{2\nu}\right)^{-1}$ [y]	$T^2_{1/2}$ [y]	Experiment
^{48}Ca $\rightarrow^{48}$ Ti	$0^+ \rightarrow 0^+$	4271	0.187	$4.10{\cdot}10^{24}$	$2.52{\cdot}10^{16}$	$4.4^{+0.6}_{-0.5} \cdot 10^{19}$	NEMO-III [Arn05]
							CANDLES [Ume06]
^{76}Ge $\rightarrow^{76}$ Se	$0^+ \rightarrow 0^+$	2039	7.8	$4.09{\cdot}10^{25}$	$7.66{\cdot}10^{18}$	$(1.5 \pm 0.1) \cdot 10^{21}$	HEID.-MOSC. [KK01]
							GERDA [Abt04]
							MAJORANA [The03]
^{96}Zr $\rightarrow^{96}$ Mo	$0^+ \rightarrow 0^+$	3350	2.8	$4.46{\cdot}10^{24}$	$5.19{\cdot}10^{16}$	$(2.3 \pm 0.2) \cdot 10^{19}$	NEMO-III [Arn05]
^{100}Mo $\rightarrow^{100}$ Ru	$0^+ \rightarrow 0^+$	3034	9.6	$5.70{\cdot}10^{24}$	$1.06{\cdot}10^{17}$	$(7.1 \pm 0.4) \cdot 10^{18}$	NEMO-III [Arn05]
^{116}Cd $\rightarrow^{116}$ Sn	$0^+ \rightarrow 0^+$	2802	7.5	$5.28{\cdot}10^{24}$	$5.28{\cdot}10^{24}$	$(2.8 \pm 0.2) \cdot 10^{19}$	NEMO-III [Arn05]
							COBRA [Daw09]
^{130}Te $\rightarrow^{130}$ Xe	$0^+ \rightarrow 0^+$	2533	34.5	$5.89{\cdot}10^{24}$	$2.08{\cdot}10^{17}$	$\left(6.8^{+1.2}_{-1.1}\right) \cdot 10^{20}$	CUORICINO [And10]
							CUORE [Arn08]
							NEMO-III [Arn05]
							COBRA [Daw09]
^{136}Xe $\rightarrow^{136}$ Ba	$0^+ \rightarrow 0^+$	2479	8.9	$5.52{\cdot}10^{24}$	$2.07{\cdot}10^{17}$		*EXO-200* [Leo08]
							EXO [Dan00]*XMASS* [Kim06]
							KamLAND-ZEN [Ter08]
^{150}Nd $\rightarrow^{150}$ Sm	$0^+ \rightarrow 0^+$	3367	5.6	$1.25{\cdot}10^{24}$	$8.41{\cdot}10^{15}$	$(8.2 \pm 0.9) \cdot 10^{18}$	NEMO-III [Arn05]
							SNO+ future [Che08]

Table 1.2: $\beta\beta$ decay candidates. Listed are Q values, natural abundance and phase space factors (from [Zub04], references therein) as well as the latest recommended $T^{2\nu}_{1/2}$ (from [Bar10b], references therein). Experiments currently starting to take data or still under construction are displayed in *italic*.

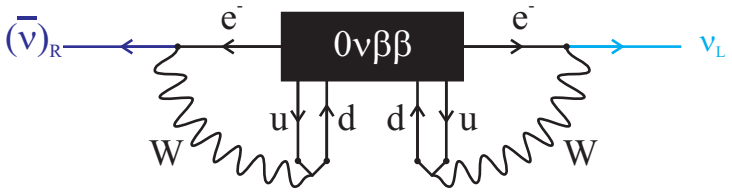

Figure 1.5: $0\nu\beta\beta$ Feynman diagram. The Schechter-Valle theorem [Sch82] states that $0\nu\beta\beta$ decay requires a finite neutrino Majorana-mass term, independent of the process.

The energy spectrum can be approximated by [Zub04]

$$\frac{\mathrm{d}N}{\mathrm{d}T_e} \propto (T_e + 1)^2 \, (Q + 1 - T_e)^2 \,, \tag{1.21}$$

with T_e being the kinetic energy of a single electron. Based on Fermi's Golden Rule, the half life of the decay derives to

$$\left(T^{0\nu}_{1/2}\right)^{-1} = G^{0\nu}(Q, Z) \, |M^{0\nu}_{GT} - M^{0\nu}_{F}|^2 \left(\frac{\langle m_{\nu_e} \rangle}{m_{\beta\beta}}\right)^2 , \tag{1.22}$$

with the Gamow-Teller and Fermi matrix elements

$$M^{0\nu}_{GT} = \sum_{m,n} \langle 0^+_f | \tau_{-m} \tau_{-n} \, H_{GT}\,(r) \, \sigma_m \sigma_n | 0^+_i \rangle \,, \text{ and} \tag{1.23}$$

$$M^{0\nu}_{F} = \sum_{m,n} \langle 0^+_f | \tau_{-m} \tau_{-n} \, H_{F}\,(r) \, | 0^+_i \rangle \left(\frac{g_V}{g_A}\right)^2 . \tag{1.24}$$

Here, $r = |r_m - r_n|$ is the distance between two nucleons in the nucleus and $H(r)$ describes the neutrino potential. Calculated values for the phase space factor $G^{0\nu}(Q, Z)$ are listed in [Cow06]. The latter acts on the nuclear wave function and describes the exchange of virtual neutrinos. Since the interaction is a short range interaction, the momentum transfer involved is large ($O(0.5)\,\mathrm{fm}^{-1}$ [Fre07]). Therefore, the transition can happen via many virtual states with any spin in the intermediate nucleus and many transitions contribute to $M^{0\nu}$. The 'Anatomy of the $0\nu\beta\beta$ nuclear matrix element' is discussed in detail in [Š08] as well as contributions of different transition states to $M^{0\nu}$.

Current and future experiments searching for neutrino less double beta decay are listed in Table 1.2. 'Sense and sensitivity of double beta decay experiments' are discussed in [GC10].

1.2.3 $\beta^+\beta^+$, β^+EC, and ECEC decay

In addition to $\beta^-\beta^-$ decay, $\beta^+\beta^+$ decay is also of relevance. This process occurs along with β^+EC and ECEC decay and the following channels are possible:

$$(Z, A) \rightarrow (Z-2, A) + 2\mathrm{e}^+ \,(+2\nu_e) \qquad \left(\beta^+\beta^+\right) \qquad (1.25)$$

$$\mathrm{e}^-_B + (Z, A) \rightarrow (Z-2, A) + \mathrm{e}^+ \,(+2\nu_e) \qquad \left(\beta^+\mathrm{EC}\right) \qquad (1.26)$$

$$2\mathrm{e}^-_B + (Z, A) \rightarrow (Z-2, A)\,(+2\nu_e)\,. \qquad (\mathrm{ECEC}) \qquad (1.27)$$

Some isotopes known to decay via $\beta^+\beta^+$ decay are ^{78}Kr, ^{96}Ru, ^{106}Cd, ^{124}Xe, ^{130}Ba, and ^{136}Ce. A complete list including limits on decay half lives is presented in Ref. [Bar10a]. In the case of ^{130}Ba a half life of $(2.2 \pm 0.5) \cdot 10^{21}$ y (68% C.L.) for all weak 2ν processes was determined in a geochemical experiment [Mes01].

In general, $\beta^+\beta^+$, β^+EC, and ECEC decays are of less experimental interest because for $\beta^+\beta^+$, the Q-value is reduced by $4m_ec^2$ due to the Coulomb barrier. Therefore, predicted half lives are of the order of $\sim 10^{27}$ years for $\beta^+\beta^+$, $\sim 10^{22}$ years for β^+EC ($Q - 2m_ec^2$) and $\sim 10^{21}$ years for ECEC processes [Bar10a]. Furthermore, an ECEC decay only creates vacancies in the atomic shell that are hard to detect (either by x-ray or Auger-electron emission).

In some cases of 0νECEC decay, a resonance condition can exist that is expected to enhance the transition rate [Win55]. For a resonance condition, the daughter nucleus is required to have an excited level E with $Q - E$ close to zero. In [Suj04], several cases were investigated. For the isotope ^{112}Sn, the 0νECEC rate was estimated to be enhanced by $\sim 5 \cdot 10^5$ and a detailed discussion of this case is presented in [Kid08]. The measured limits for 0νECEC and other β^+EC and ECEC processes in ^{112}Sn are $T_{1/2} > 4.7 \cdot 10^{20}$ y and $T_{1/2} > (0.6 - 8.7) \cdot 10^{20}$ y [Bar09], respectively (90% C.L.). The most recent measurement of the 0^+_4 energy level in the ^{112}Sn-daughter ^{112}Cd [Gre09], and a high precision Penning-trap measurement of the Q value [Rah09], showed that the resonance condition is not given in ^{112}Sn. Therefore, a minimum half life of $T_{1/2} = 5.9 \cdot 10^{29}/m_\nu^2$ y eV^2, with m_ν being the effective neutrino mass in units of eV, is estimated [Rah09]. Nevertheless, if $0\nu\beta^-\beta^-$ is detected, one can gain information on the underlying processes even from the limits of $0\nu\beta^+$EC [Hir94].

The focus of current $\beta\beta$ decay experiments lies on the detection of the $2\nu\beta^-\beta^-$ and $0\nu\beta^-\beta^-$ decay modes. Hence, $\beta^+\beta^+$, β^+EC, and ECEC are only briefly mentioned here and not considered further in this work.

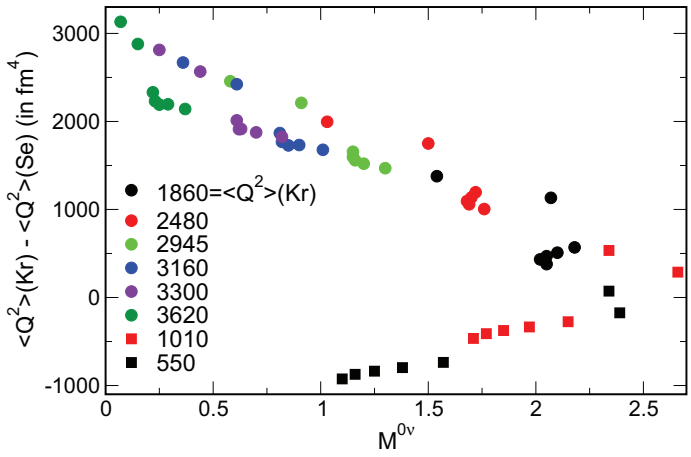

Figure 1.6: Calculated $M^{0\nu}$ as function of artificially introduced nuclear quadrupole deformation. Picture from [Vog08].

1.3 $\beta\beta$ decay and the matrix element problem

As already mentioned, if $0\nu\beta\beta$ decay is observed the neutrino has to be a Majorana particle independent of the underlying process. However, an observation does not imply in general that the effective neutrino mass can be deduced from Eq.(1.1). If $0\nu\beta\beta$ decay happens via the exchange of unknown gauge bosons or if new particles are created during the decay, the neutrino mass can no longer be deduced simply from Eq.(1.1). So far, no indication has been found for a non-standard interaction of the neutrino. Therefore, one assumes that the neutrino only interacts via the electro-weak exchange particles W and Z, and hence, the effective Majorana neutrino mass can be deduced from Eq.(1.1). For a more detailed discussion the reader is referred to [Vog08, Avi08].

Under the assumption that $0\nu\beta\beta$ decay is the only $\beta\beta$ decay mode without the emission of a neutrino, and assuming that the neutrino is a light neutrino, one can extract the effective Majorana neutrino mass from the half life of the decay. To determine meaningful neutrino masses one needs to calculate $M^{0\nu}$ with an uncertainty of less than 20% [Aki97]. These calculations are performed within the framework of proton-neutron quasi-particle random phase approximation (pn-QRPA, see for example [Hal67, Eng88, Suh88, Mut88, Geh07]), shell modell calculation (see for example [Hax84, Cau96, Cau08, Eng09]), and interacting boson model (IBM-2, [Bar09]). Recently, calculations have been published applying projected Hartree-Fock-Bogoliubov in limited configuration spaces and schematic interactions [Cha08] as well as density functional methods using the Gogny D1S functional [Rod10]. The difficulties in these calculations arise from large parameter spaces and deformation of the nuclei involved. Shell Model calculations studying deformation effects are published in [Cha09, Rat09] and

QRPA calculations accounting for deformation are presented in [You09, Mor09, Fan10]. In Ref. [Men09], the initial nucleus in the transition ^{82}Se $\rightarrow^{82}$Kr was artificially deformed by adding unrealistic quadrupole-quadrupole interactions to the Hamiltonian in order to investigate the influence of deformation. In Fig. 1.6, the resulting $M^{0\nu}$ are plotted against the squared quadratic quadrupole moment deformation. With an increasing difference in deformation between mother and daughter nucleus, given by a non-zero $\langle Q^2 \rangle$(Kr) $-$ $\langle Q^2 \rangle$(Se), the calculated matrix element decreases. This demonstrates that the NME strongly depends on nuclear deformation.

If one compares NMEs for different elements calculated in different theoretical frameworks, deviations up to a factor of 2-3 arise [Rod06, Geh07, Rod09]. Some recently calculated $M^{0\nu}$ are displayed in Fig. 1.7 to illustrate the situation. All matrix elements were calculated using the parameters $R = r_0 \cdot A^{1/3}$ with $r_0 = 1.2\,\mathrm{fm}^{-1}$ and an axial-vector coupling $g_A = 1.25$. If different parameters are used in calculations, the NMEs can be compared with each other by normalizing them to $M'^{0\nu} = \left(\frac{g_A}{1.25}\right)^2 \left(\frac{1.2}{r_0}\right) \mathrm{fm}^{-1}\, M^{0\nu}$ (see for example [Men10]).

Typically, experimental results from $2\nu\beta\beta$ decays are used to benchmark theoretical calculations. This is especially the case in the framework of pn-QRPA. In this theoretical description, a particle-particle parameter g_{PP} is introduced to the Hamiltonian. This parameter is used to tune calculated half lives to experimental values. Since $2\nu\beta\beta$ only happens via intermediate 1^+ states, g_{PP} is only sensitive to these transitions via intermediate states up to $\approx$5 MeV. Then, this g_{PP} is used in the calculation of $M^{0\nu}$. However, as $0\nu\beta\beta$ happens via all virtual transition states up to $\approx$100 MeV, $M^{0\nu}$ is rather insensitive to g_{PP} [Š10, Fre07]. In shell model calculations, no tunable parameter exists but calculations are still judged on how well they reproduce experimental $2\nu\beta\beta$ results.

Additional experimental information on the underlying nuclear processes can be gained by measuring the EC and β^- branching ratios of intermediate nuclei in $\beta\beta$ decays. By measuring these BRs, the transition strength via the ground state in $M^{2\nu}$ (see Eq.(1.17)) is determined directly. This knowledge can then be used to benchmark theoretical models because the measurement directly probes the nuclear wave function. Thus, ECBR measurements are important for all models as they provide details on the involved nuclear physics.

In the framework of QRPA, a comparison of g_{PP} extracted from $2\nu\beta\beta$ to g_{PP} extracted from measured EC and β^- BRs shows a huge discrepancy indicating inconsistencies in the theoretical description. This is discussed in detail in [Suh05].

In some cases of $2\nu\beta\beta$ decay, a so-called single-state dominance (SSD) is expected to be present, where the transition via the lowest lying intermediate 1^+ state accounts for a majority of the strength in the $M^{2\nu}$ matrix element [Aba84]. Currently, an SSD is experimentally observed in the $\beta\beta$ decay of ^{100}Mo [Mor09]. In the decay of ^{116}Cd,

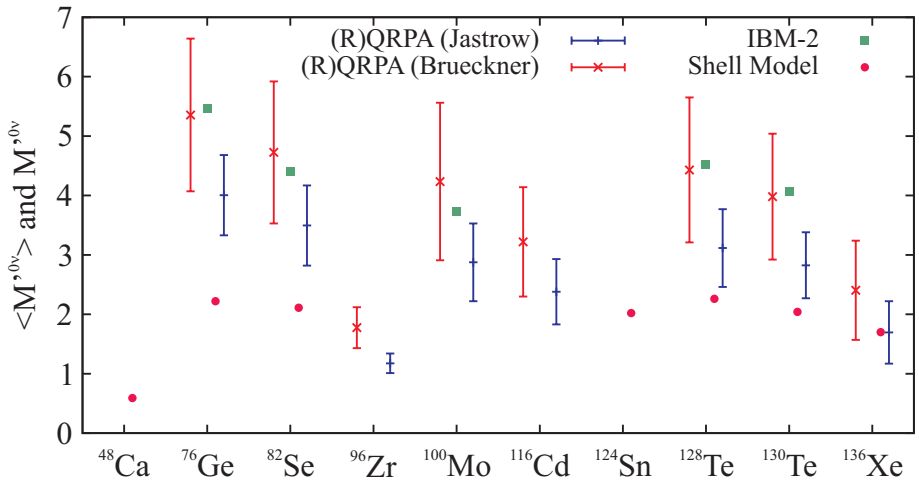

Figure 1.7: Calculated $M'^{0\nu}$. ((R)QRPA) Average $\langle M'^{0\nu}\rangle$ calculated within the renormalized QRPA applying different treatments of short-range correlations (from [Š09]) and averaging over different parameter sets. The error bars were obtained by varying the initial parameter set. (IBM-2) $M'^{0\nu}$ calculated in the Interacting Boson Model [Bar09]. (Shell Model) NME calculated within the Shell Model [Cau08].

an SSD is expected but experimental uncertainties are not sufficiently small to allow a definite claim [Dom05, Mor09]. If an SSD is present, the Gamow-Teller matrix element $M^{2\nu}_{GT}$ presented in Eq.(1.17) can be approximated by [Mor09]

$$M^{2\nu}_{GT}(SSD) = \frac{M(GT^-)M(GT^+)}{\left(Q_{\beta^-} + Q_{EC}\right)/2} + \frac{1}{\sqrt{ft_{EC}}}\frac{1}{\sqrt{ft_{\beta^-}}}\frac{6\,D}{g_A^2\left(Q_{\beta^-} + Q_{EC}\right)}, \tag{1.28}$$

where $D = 6147$ and $g_A = 1.25$ is the axial-vector coupling strength. Q_{EC} and Q_{β^-} are the EC and β^- Q values of the intermediate nucleus and ft_{EC} and ft_{β^-} are the ft values of EC and β branches, respectively. In the case of an SSD, $M^{2\nu}$ can be determined completely by measuring the Gamow-Teller matrix elements $M(GT^-)$ and $M(GT^+)$. $M(GT^-)$ can be determined in charge exchange reactions such as (p,n) and $(^3\mathrm{He},\mathrm{t})$, while $M(GT^+)$ can be determined in (n,p) and $(d,^2\mathrm{He})$ charge exchange reactions (see for example Ref. [Vog08, Mor09]). The interpretation of transfer reactions is, however, model-dependent. A model-independent way of determining $M(GT^\pm)$ is by measuring EC and β^- BRs of the short-lived transition nucleus in $\beta\beta$ decays. The difficulty in determining these ECBRs is their suppression by five orders of magnitude compared to β^- branches. Additionally, the signature of an EC is the emission of an x-ray which is difficult to detect in the presence of dominantly abundant β particles. These two facts make ECBR measurements challenging. So far, the ECBRs of ^{100}Tc [Gar93] and ^{116}In [Bha98] have been determined in tape station experiments. Furthermore,

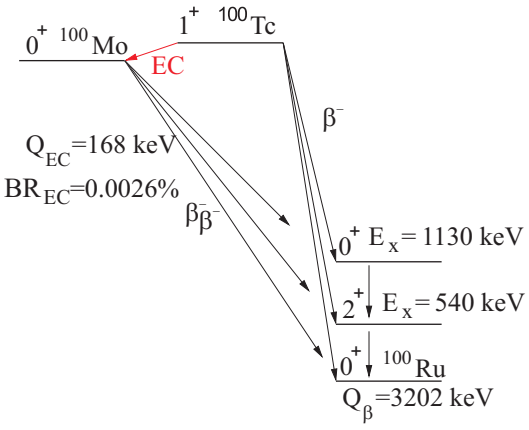

Figure 1.8: Decay scheme of ^{100}Mo. Knowledge of the electron capture branching ratio of ^{100}Tc is crucial in the determination of $M_{2\nu}$. Picture courtesy of [Sju08a].

^{100}Tc has been re-measured applying the technique of Penning trap assisted decay spectroscopy [Sju08b]. Both techniques are briefly discussed hereafter.

1.4 Conventional electron-capture branching ratio techniques

The conventional technique of determining ECBRs is the use of tape stations. In this technique, a radioactive sample is implanted on a tape and then moved in front of one or several detectors that detect x-rays and β particles. After a measurement period, a new sample is implanted on the tape and moved in front of the detector. This technique has been applied to determine the ECBR of ^{100}Tc, the intermediate transition nucleus of ^{100}Mo $\beta\beta$ decay [Gar93]. The latter decay scheme is illustrated in Fig. 1.8. The difficulties of this method arise from isobaric contaminations in the sample, the β background from dominating β branches, and x-ray attenuation in the carrier material.

The second ECBR measurement of ^{100}Tc was improved by performing trap assisted decay spectroscopy. This experiment was set up by S.K.L. Sjue and performed in Jyväskylä [Sju08b]. There, the sample was isobarically purified in a Penning trap by means of a mass-selective buffer gas cooling technique [Sav91]. Afterwards, the sample was implanted into the cavity of a plastic scintillator. A low energy Ge detector was placed as close as $\approx 0.32\,\mathrm{cm}$ to the implanted sample and recorded x-rays and γ rays from the decay of ^{100}Tc (see Fig. 1.9). Electrons from the dominating β decay were detected by the plastic scintillator and used to discriminate photons detected by the low energy Ge detector. With this technique, the ECBR of ^{100}Tc was determined to be $BR(EC) = (2.60 \pm 0.34 \pm 0.20) \cdot 10^{-5}$ [Sju08b] and is in agreement with [Gar93]. The

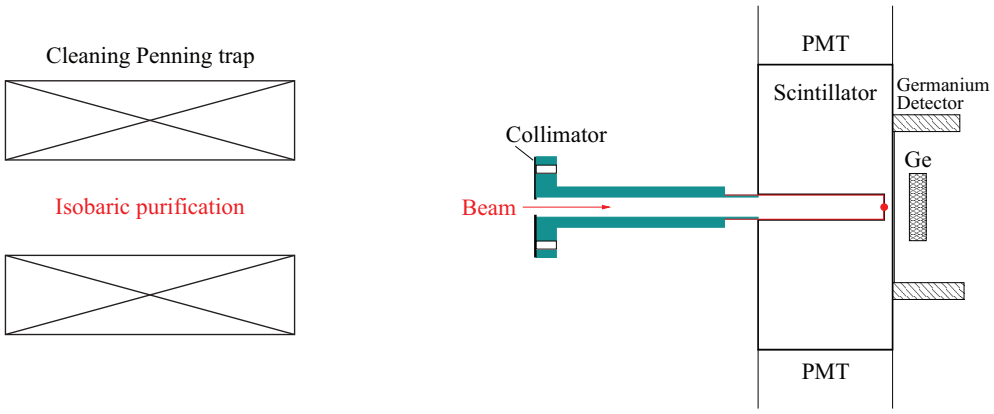

Figure 1.9: Schematic of the detector setup used in [Sju08b] to measure the ECBR of ^{100}Tc. Picture courtesy of [Sju08a].

resulting Gamow-Teller strength $B(GT;^{100}\,\mathrm{Mo} \rightarrow^{100}\,\mathrm{Tc}) = 0.95 \pm 0.16$ is about 80% larger than the value extracted from charge exchange reaction. However, Gamow-Teller strengths calculated with QRPA range from $4 \leqslant B(GT;^{100}\,\mathrm{Mo} \rightarrow^{100}\,\mathrm{Tc}) \leqslant 6$ [Sju08b].

A limiting factor of this method is the x-ray attenuation of the scintillator and the Al foil where the ions are implanted. The veto of β particles reduces the β induced background but cannot suppress it completely. A dominant background in the x-ray region due to e^- bremsstrahlung remains present.

To overcome these drawbacks of β-dominated background and isobaric contamination and solve the discrepancy in determined ECBRs between charge exchange reactions and decay spectroscopy, motivated the development of a new technique to measure ECBRs of intermediate $\beta\beta$ decay nuclei. The aim of this technique is the measurement of these transitions with uncertainties comparable to the ones achieved in [Sju08b]. Furthermore, it will resolve the discrepancy between previously measured ECBRs.

1.5 TITAN-EC – electron-capture branching ratio measurements at TITAN

A novel technique of in-trap decay spectroscopy has been proposed to measure the ECBRs of transition nuclei in $2\nu\beta\beta$ decays [Fre07] with an uncertainty of $\sim 10\%$. The basic concept of this proposed technique is to perform decay spectroscopy on ions stored inside a Penning trap. The trap's strong magnetic field guides all electrons originating from dominating β decays out of the trap where they are detected. X-rays following an EC are emitted isotropically. Therefore, with x-ray detectors positioned radially

ECBR mother	Transition	ECBR daughter	K_α	Half life
^{76}As	$2^- \rightarrow 0^+$	^{76}Ge	9.9 keV	26.2 h
^{82m}Br	$2^- \rightarrow 0^+$	^{82}Se	11.2 keV	6.1 min
^{100}Tc	$1^+ \rightarrow 0^+$	^{100}Mo	17.5 keV	15.8 s
^{110}Ag	$1^+ \rightarrow 0^+$	^{110}Pd	21.2 keV	24.6 s
^{114}In	$1^+ \rightarrow 0^+$	^{114}Cd	25.3 keV	71.9 s
^{116}In	$1^+ \rightarrow 0^+$	^{116}Cd	25.3 keV	14.1 s
^{128}I	$1^+ \rightarrow 0^+$	^{128}Te	27.5 keV	25.0 min

Table 1.3: A list of isotopes that are proposed to be measured with TITAN-EC.

around the trap center one can determine the ECBR of stored isotopes with ideally no β background contribution in the x-ray detector.

This technique requires an isotope production facility capable of producing intermediate $\beta\beta$ transition nuclei as well as a Penning trap with visible access to the trap center. Both are present at TRIUMF's Ion Trap for Atomic and Nuclear science (TITAN). One of TITAN's ion traps, the electron beam ion trap (EBIT), can be operated as an open access spectroscopy Penning trap, i.e. without the electron beam. In this operation mode, the electron gun is retracted and replaced by a β detector placed along the trap axis and used to detect β particles guided out of the trap.

The trap's magnetic field is created by a pair of superconducting coils in a quasi-Helmholtz configuration. This configuration allows one to have access-ports between the coils. Additionally, the central trap electrode where the ions are stored, is segmented with slit-apertures. This setup allows one to install up to seven x-ray detectors radially around the trap, installed either inside or outside the vacuum vessel. In the latter case, Be windows with little x-ray attenuation separate the vacuum from the external atmosphere. A schematic of TITAN-EC, the experiment designed to measure ECBRs at TITAN, is shown in Fig. 1.10. In this figure, the pair of coils in the quasi-Helmholtz configuration, the central trap electrode, two x-ray detectors and the β detector are illustrated. Radioactive ions are injected into the spectroscopy Penning trap from the left. While ions are stored, their x-ray decays are observed radially (wavy arrow) while β particles are guided out of the trap along its axis (cone).

The scope of this work was the development and implementation of the in-trap decay spectroscopy technique proposed in [Fre07]. All nuclei that are proposed to be measured with this new technique are listed in Table 1.3.

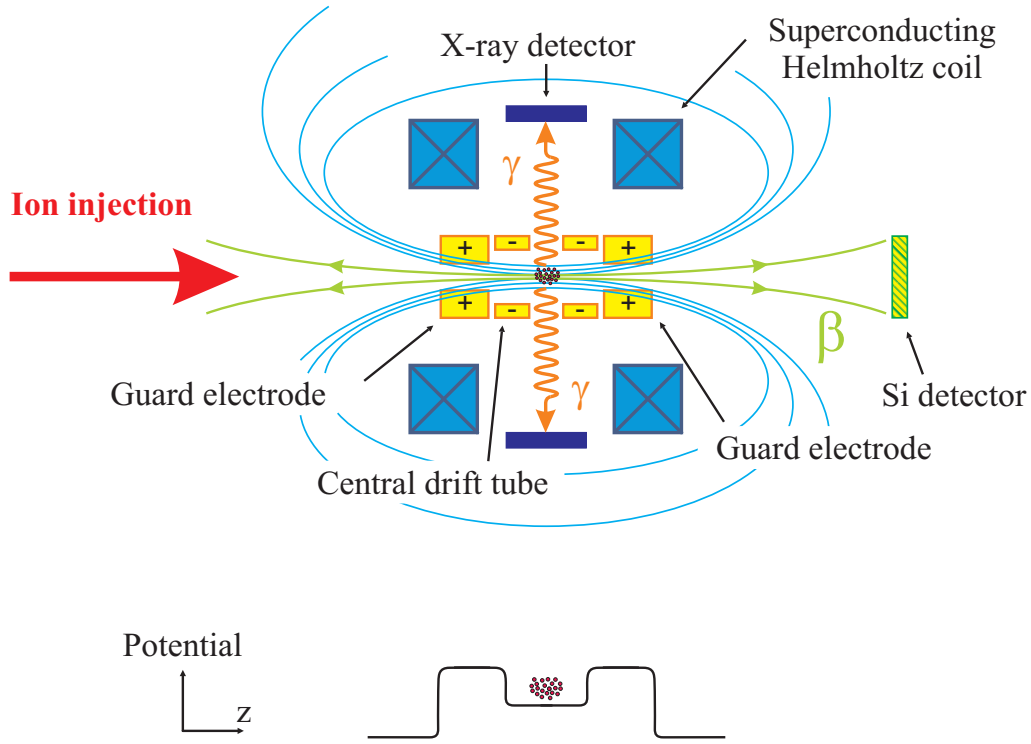

Figure 1.10: Schematic of the electron capture branching ratio measurement setup with electric potential applied to the trap electrodes (guard electrodes and central drift tube).

Chapter 2

TITAN Overview

The TRIUMF Ion Traps for Atomic and Nuclear science (TITAN) facility is located at TRIUMF's Isotope Separation and Acceleration (ISAC) facility (Fig. 2.1). It is dedicated to high precision experiments on short-lived radioactive isotopes. The TITAN setup presently consists of a digitally driven Radio Frequency Quadrupole (RFQ) ion beam cooler and buncher [Smi06], a high-precision mass measurement Penning trap (MPET) [Bro09], and an Electron Beam Ion Trap (EBIT) [Lap10]. The system has been successfully used for precision mass measurements, in particular, for the light neutron-rich nuclei ^{8}He [Ryj08], ^{11}Li [Smi08], and ^{11}Be [Rin09]. These nuclei are referred to as neutron halos. Additionally, the mass of ^{12}Be has been determined to evaluate the isobaric mass multiplet equation for the lowest lying $T = 2$ multiplet for the $A = 12$ system [Ett10b]. The uniqueness of the TITAN mass measurement system versus other on-line systems stems from the EBIT. The EBIT can be used for charge breeding to enhance the precision of mass measurements and has been operational on-line for the first time for the mass measurement of $^{48}\mathrm{K}^{4+}$ ($t_{1/2} = 6.8(2)$ s [NND10]) [Lap10].

The special design of the EBIT allows one to use it as a spectroscopy Penning trap and not as a charge breeder, i.e., without the electron beam. The magnetic field is produced by a pair of coils in a quasi-Helmholtz configuration that, in combination with a trap electrode configuration that has slit-apertures, allows direct visible access to the trap center. This unique setup offers the possibility to perform spectroscopy on ions injected into the spectroscopy EBIT which, in the case of operation without the electron beam, functions as a spectroscopy Penning trap. One of the possible spectroscopy experiments is the newly developed technique to perform in-trap electron capture decay spectroscopy for double beta decay. This technique aims to measure electron capture decays of intermediate nuclei in double β decays. Its feasibility has been demonstrated in the framework of this thesis during two campaigns with the radioactive isotopes ^{107}In [Ett09, Bru10b] and ^{124,126}Cs [Bru10a].

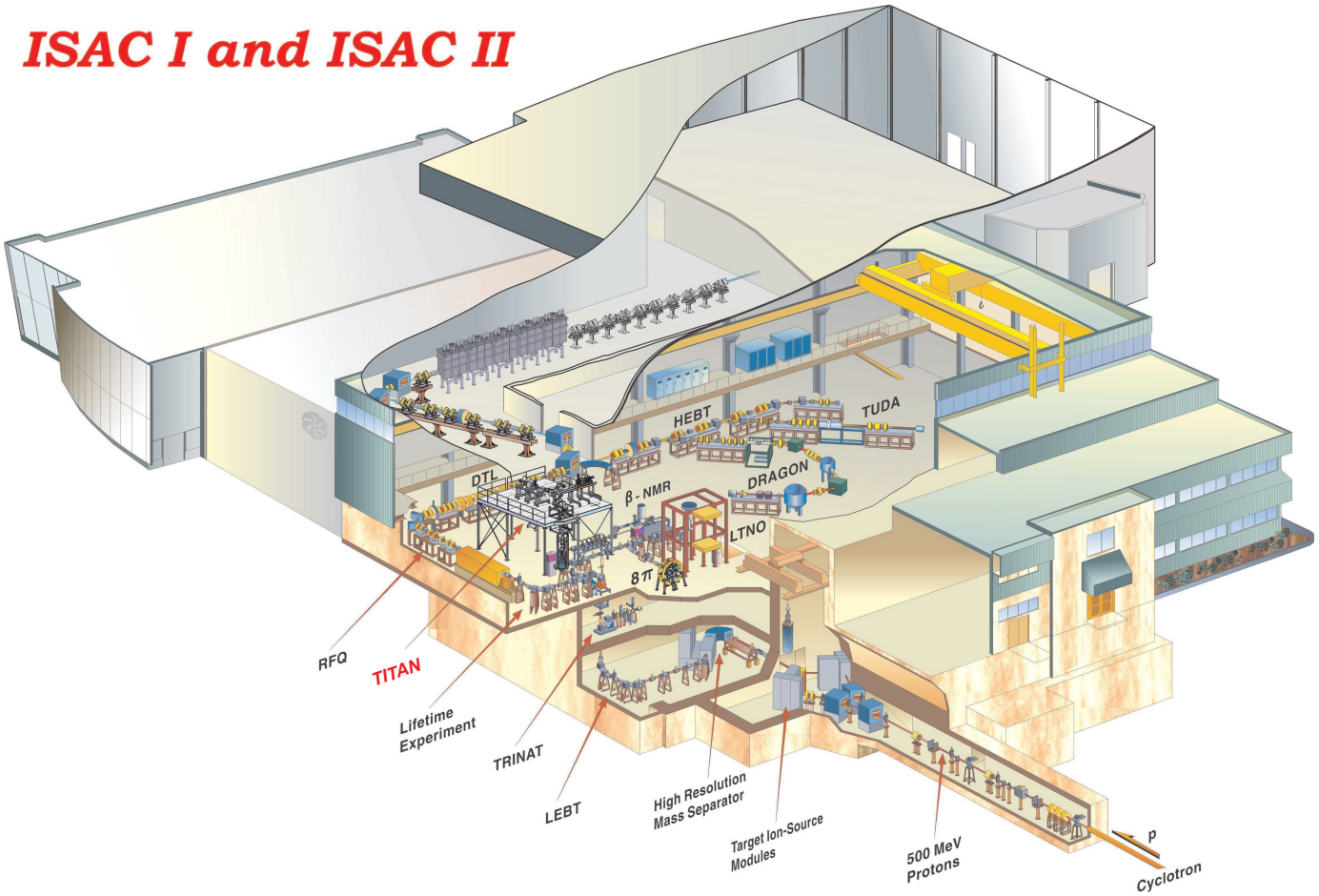

Figure 2.1: ISAC experimental hall at TRIUMF. TITAN is situated on a platform in the low energy area of ISAC I (source: www.triumf.ca).

2.1 Radioactive isotope production at ISAC

The heart of TRIUMF forms its cyclotron that accelerates H^- to a kinetic energy of up to 520 MeV. To extract protons from the cyclotron, a graphite foil is placed in the beam path. This strips off the two electrons from H^- and leaves a bare proton. The change in polarity changes the direction of the proton in the cyclotron's magnetic field, i.e., the protons are bent out of the cyclotron and extracted.

Proton beams with typically 500 MeV and up to 100 µA are then delivered to TRIUMF's ISOL-type isotope facility ISAC [Dom00, Dom02]. The protons impinge on one of the two targets. Fig. 2.1 presents the overall layout of the ISAC facility; the design of a target is shown in Fig. 2.2. Inside the target, stable and radioactive isotopes are produced. They diffuse to the surface, and eventually evaporate. A hot tube guides these isotopes to the ion source where they are ionized. Currently, three ion sources are available at TRIUMF, namely a laser ionization ion source (TRILIS) [Wen03], a surface ion source, and an electron cyclotron resonance (FEBIAD) ion source [Bri08].

The ionized isotopes are extracted out of the ion source by electrostatic potentials. Depending on the combination of target material and ion source, a broad range of isotopes leave the ion source from which they are extracted with a variable potential ranging from 12 keV up to 60 keV. This isotope cocktail is then cleaned by two dipole magnets in combination with a slit setup. Depending on their mass-to-charge ratio m/q and velocity v, the ions pass through the magnet on different radii $r = m\,v/q\,B$ and are thus spatially separated with a typical resolution of $R \sim 3000$. A birds eye view of target area and mass separator setup is also illustrated in Fig. 2.2.

The ion beam is then guided electro-statically to the experimental area in ISAC where they are either used directly in experiments such as TITAN (see Fig. 2.1) or further accelerated for experiments in ISAC-I or ISAC-II.

2.2 The TITAN facility

TITAN is a setup currently consisting of the three ion traps displayed in Fig. 2.3: a digitally driven Radio Frequency Quadrupole ion beam cooler and buncher (RFQ), a high-precision mass measurement Penning trap (MPET), and an Electron Beam Ion Trap (EBIT).

During a measurement, the ion beam coming from ISAC or the TITAN off-line ion source is first cooled and bunched in the RFQ. Afterwards, the ion bunches can be sent either to the MPET or EBIT. With the MPET, high precision mass measurements are performed. If an increase in precision is required, the ions are injected into the EBIT for charge-breeding prior to the mass measurement. In the case of an ECBR

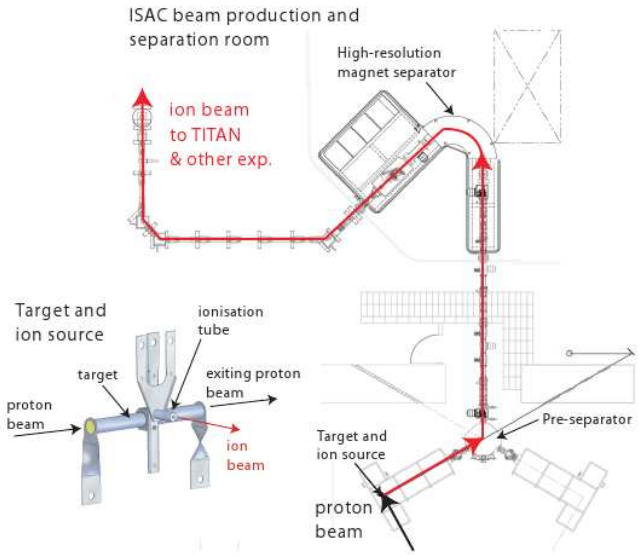

Figure 2.2: ISAC target area and mass separator in bird's eye view. The inset shows a model of target and ionization tube. Picture courtesy of J.-P. Lavoie.

measurement, the ion bunches are sent directly into the spectroscopy Penning trap, i.e., the EBIT without the electron beam, where they are captured and stored.

2.2.1 Ion trapping techniques at TITAN

The TITAN experiment uses three types of ion traps to create a three-dimensional confinement for ions; namely, Penning trap, Paul trap, and electron beam ion trap. These first two techniques will be introduced in the following sections. A detailed description of the principle of an EBIT is given in [Gil01, Cur03]

Paul trap

One possible configuration of a Paul trap is based on a quadrupole electrode structure. It consists of opposite facing electrodes at the same electric potential whereas neighboring electrodes are at a different potential. This electrode configuration creates an electrostatic quadrupole field that focuses charged particles along one axis and de-focuses them along a second axis perpendicular to the first. A schematic view of a quadrupole and the resulting potential is displayed in Figure 2.4. By applying a radio-frequency (RF) to the electrodes, the quadrupole field rotates along the geometrical axis ϕ and thus creates a confining potential. The ion motion in a linear quadrupole

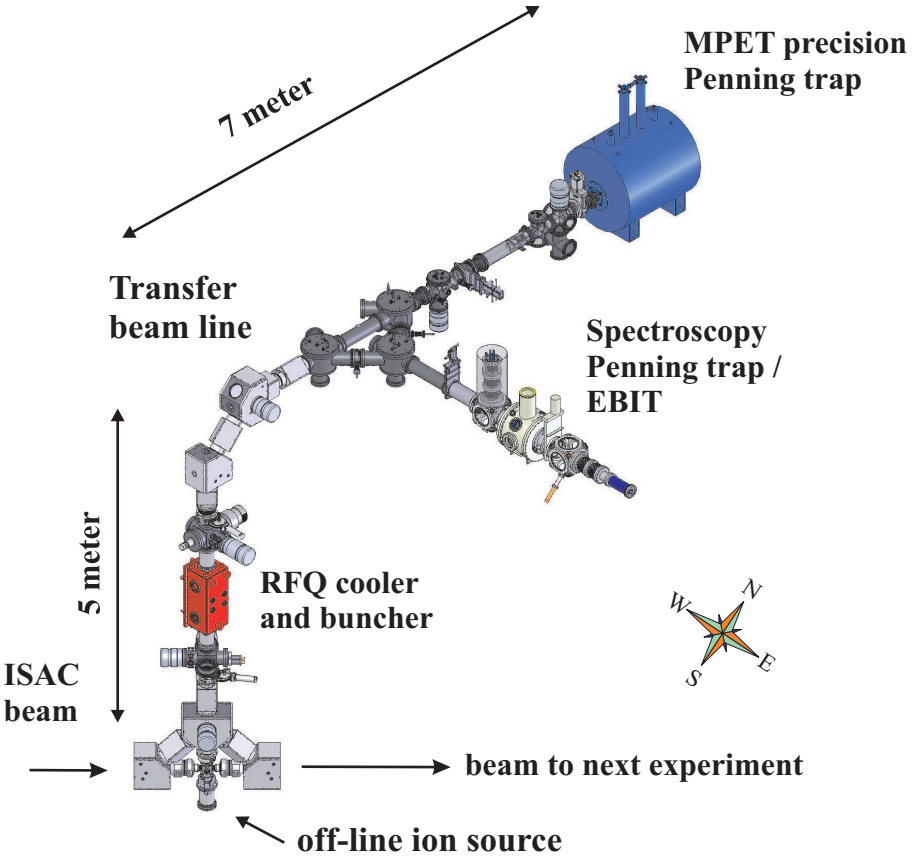

Figure 2.3: The TITAN facility with its ion traps RFQ, MPET and EBIT. A description is given in the text.

Paul trap consists of a macro-motion and micro-motion for which the equations of motion can be solved analytically [Maj04]. The ion motion depends on the ion mass m, the RF amplitude V applied to the electrodes at a distance $2 \cdot r_0$, and the RF frequency ω_{RF}.

A stability parameter, see for example [Gho95],

$$q = \frac{4\,Z\,e\,V}{m\,\omega_{RF}^2\,r_0^2} \tag{2.1}$$

indicates whether an ion with charge Z is on a stable motion in the Paul trap. For sinusoidal driven RFQs, the ion motion is typically stable for $\sim 0.2 < q <\sim 0.9$. TITAN's RFQ is a digitally driven square-wave RFQ with stable operation in the region $\sim 0.2 < q <\sim 0.7$ [Smi05]. In Fig. 2.5, the solution for the ion motion is displayed for $q = 0.2$ and $q = 0.6$ for TITAN's digital driven RFQ. For $q = 0.6$, the micro-motion is larger than for $q = 0.2$; for $q > 0.7$ no macro-motion exists, hence the ion is lost in the trap. In both figures, the pure harmonic macro-motion is also displayed for comparison. A detailed description of TITAN's RFQ is given in [Smi05] while a general description of Paul traps is given in [Daw95, Maj04].

Paul traps are commonly used as ion guides [Pau58] or for ion cooling and bunching [Her01], but decay-spectroscopy of $^6He^+$ in a transparent Paul trap has also been performed [Flé08]. TITAN uses a linear Paul trap to cool, clean, and bunch DC ion beams delivered from ISAC or an off-line ion source [Smi05, Smi06].

Penning trap

In a Penning trap ions are confined by a combination of static electric and magnetic fields. The magnetic field forces the ions on a circular orbit by the Lorentz force $\vec{F}_L = q\vec{v} \times \vec{B}$ and thus confines radially. The ions with a charge-to-mass ratio q/m oscillate with a cyclotron frequency

$$\nu_C = \frac{1}{2\,\pi}\frac{q}{m}\,B \tag{2.2}$$

perpendicular to the magnetic field $\vec{B}$. Along the magnetic field axis the ions are confined by a static electric field (see. Fig. 2.6). This electric field can either be created by hyperboloidal or cylindrical shaped electrodes [Bro82, Maj04]. This leads to a three-dimensional confinement of the ions. The condition for stable confinement of particles with charge-to-mass q/m in an ideal Penning trap with dimension $d = \sqrt{z_0^2/2 + \rho_0^2/4}$ (see Fig. 2.6), magnetic field strength B, and trapping potential U_{DC} is given by [Bro82]

$$\frac{|q|}{m}B^2 > \frac{2|U_{DC}|}{d^2} \qquad q\,V_{DC} > 0\,. \tag{2.3}$$

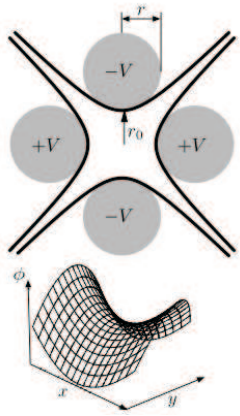

Figure 2.4: Geometrical view of an electric quadrupole. The graph illustrated the potential created by the quadrupole.

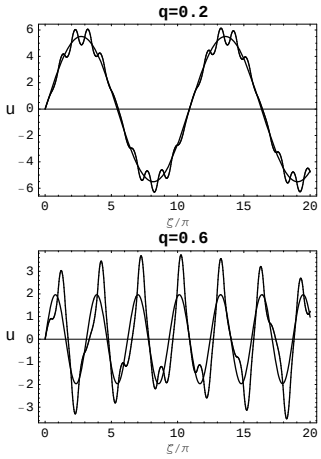

Figure 2.5: Analytical ion motion of an ion in a Paul trap. The calculation was done for TITAN's Paul trap at $q = 0.2$ and $q = 0.6$ [Smi05]. The harmonic macromotion is displayed for comparison.

In an ideal quadrupole electric field created by hyperbolic electrodes, the ion motion can be described as the superposition of three independent harmonic eigenmotions as illustrated in Figure 2.7. The ion oscillates parallel to the magnetic field lines with frequency ν_z. The cyclotron frequency of the ion is the sum of reduced cyclotron frequency ν_+ and magnetron frequency ν_- [Bro82]

$$\nu_C = \nu_+ + \nu_-. \tag{2.4}$$

By measuring the cyclotron frequency of the ion in the Penning trap, one can extract the mass of the ion if the charge state and magnetic field are sufficiently well known. For typically high precision mass measurements of the order of $\delta m/m \sim 10^{-8}$ a homogeneous B-field of several Tesla is needed. Generally, the magnetic field is not known to precisions of $\delta B/B \sim 10^{-6}$ and below. Therefore, mass measurements are performed relative to a well known mass, i.e., the cyclotron frequency of a well known mass is measured against the cyclotron frequency of an unknown mass. In this case, the generally imprecisely known magnetic field B cancels. In [Bro82] a detailed review is given for charged-particle storage. For a review on mass measurements with Penning traps, refer to [Maj04], [Bla06] and [Bla09].

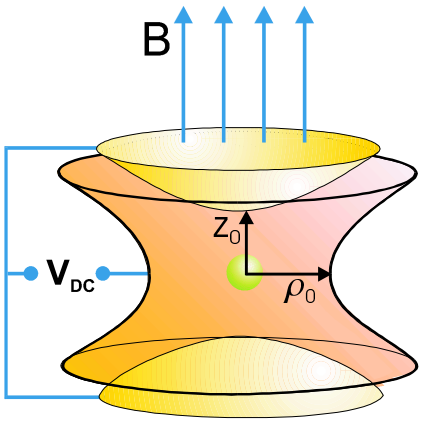

Figure 2.6: Confining fields in a Penning trap. Radially, the ions are confined by the magnetic field while an electric quadrupole field confines them axially. Picture courtesy of R. Ringle.

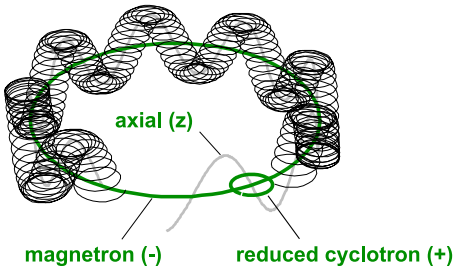

Figure 2.7: The three eigenmotions of an ion in a Penning trap. Ions oscillate with cyclotron frequency ν_+, magnetron frequency ν_- and axial frequency ν_z. Picture courtesy of R. Ringle.

2.2.2 Cooling and bunching of ions in the RFQ

The digitally driven RFQ is the first ion trap that ions pass upon their arrival at TITAN [Smi06]. It is a gas filled linear Paul trap designed to decelerate, cool, and bunch ions coming from ISAC or TITAN's off-line surface ion source. The incoming ions are electrostatically decelerated by floating the RFQ potential at high voltage ($U_{\mathrm{HV}} \sim U_{\mathrm{ion\ source}}$). Inside the RFQ, the ions are radially confined by an electric quadrupole radio frequency field and axially by a longitudinal trapping potential. In order to cool the ion beam, the RFQ is filled with buffer gas. In collisions with this buffer gas the ions lose their residual energy and cool to thermal equilibrium with the buffer gas (T≈300 K). Along the beam axis ($\vec{z}$-axis) an electric field gradient moves the ions linearly through the RFQ towards the extraction electrode. There, the ions are collected in the minimum of the applied field as illustrated in Fig. 2.8. A potential barrier, the so-called capture potential, prevents the ions from leaving the RFQ and provides three-dimensional confinement. In order to extract the ions, the capture potential is switched from a repulsive potential to an attractive potential, the so-called extraction potential. To achieve extractions of short pulses, an electrode further up-stream is switched to a repulsive potential to accelerate ions out of the RFQ. The applied potential during extraction is shown by the dashed red line in Fig. 2.8.

After the extraction out of the RFQ, the ions are accelerated as a bunch into a drift tube. This tube is switched to ground potential while the ion bunch travels through

it. The drift tube works as an 'ion elevator' and allows one to adjust the ion beam transport energy.

TITAN's RFQ consists of 24 electrodes that create the drag field (see Fig. 2.8 and [Smi05, Bru10c]). A unique feature of this RFQ is the symmetric design of the electrodes. This allows one to apply a drag-field with the potential minimum at the entrance of the RFQ. Thus, ions are collected at the entrance of the RFQ and can be sent in bunches back into the ISAC beam line towards other experiments such as the laser spectroscopy experiment [Man10].

During general operation the RFQ is biased at a potential several tens of volts below the ion source. In an on-line experiment, the floating voltage of the RFQ is set to the nominal ion source potential and optimized using the transmission through the RFQ as a measure. Typically, ISAC's ion beams are delivered with a kinetic energy of about 20 keV to TITAN. The pulsed drift tube is operated at 18 kV to match TITAN's beam line acceptance. The TITAN beam line and experiments are designed for beam energies of 2 keV. If ISAC delivers beam with lower or higher energy, the potential of the drift tube is changed accordingly. Currently, TITAN can accept ISAC beams of up to 40 keV.

2.2.3 Measurement Penning Trap

The MPET is TITAN's ion trap dedicated to high precision mass measurements applying the ion cyclotron resonance time-of-flight technique (ICR-TOF) [Bol90, Kön95] in which ions are captured dynamically in the Penning trap and excited with a quadrupole radio frequency ν_{RF}. When $\nu_{RF} = \nu_C$, this excitation converts the magnetron motion ω_- to the reduced cyclotron motion ω_+. For a measurement, the ion is first brought onto a well defined and reproducible magnetron radius. Then, the RF excitation ν_{RF} is applied for an excitation time T_{RF} such that the magnetron motion is fully converted to reduced cyclotron motion. At that time the ion has the maximal radial kinetic energy. After the excitation, the ion is extracted out of the Penning trap onto a multi-channel plate detector (MCP) and its time-of-flight is recorded. While the excitation time T_{RF} is kept constant, measurements are performed for different RF frequencies ν_{RF} around the cyclotron frequency ν_C of the ion of interest. If $\nu_{RF} = \nu_C$, the ions' kinetic energy gain is maximal and their time-of-flight is minimal. A measured time-of-flight resonance of $^7Li^+$ is displayed in Fig. 2.9. It has been demonstrated with stable $^7Li^+$ from TITAN's off-line surface ion source, that a precision of $4 \cdot 10^{-9}$ could be reproducibly achieved [Bro09].

One feature that distinguishes TITAN's Penning trap from other traps is the specialization in measuring short-lived radioactive isotopes with $t_{1/2} \lesssim 50$ ms. This is made possible using a Lorentz steerer [Rin07] that pushes ions off-axis when they enter the magnetic field. This defines the ions on an initial magnetron radius inside the trap

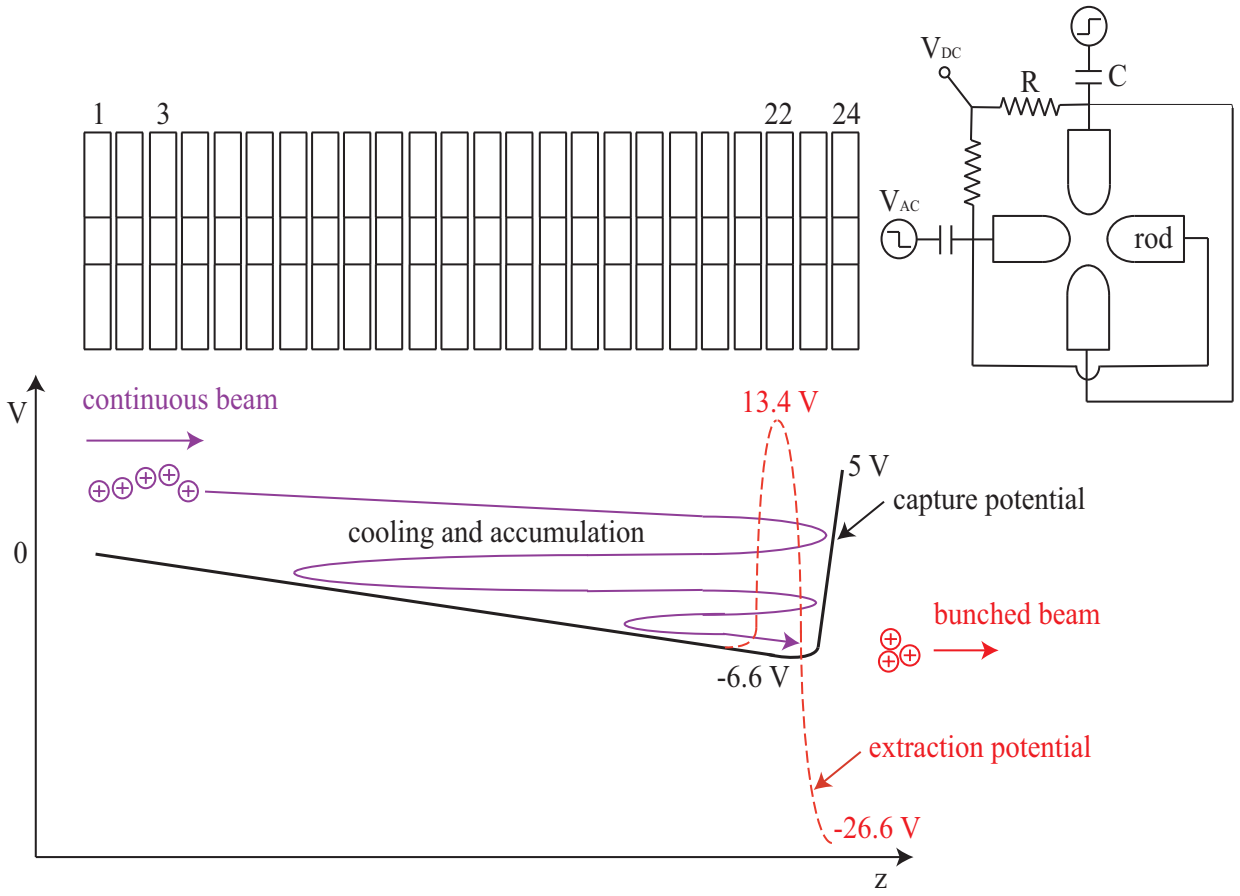

Figure 2.8: Electrode structure of the TITAN-RFQ and a schematic of the drag-field applied to the electrode segments. During the cooling time, the capture potential (thick, black line) is applied to collect the ions in a potential well close to the extraction electrode. In order to extract ions, the extraction potential (red dashed line) is applied. Picture courtesy of M. Brodeur [Bro10a].

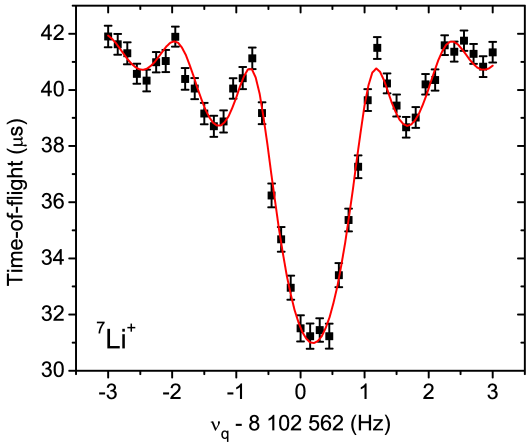

Figure 2.9: Time-of-flight resonance of $^7Li^+$ after an excitation time T_{RF} of 900 ms. The resonance spectrum is fitted with the theoretical line shape [Kön95].

and allows for shorter measurement cycles. Without a Lorentz steerer, a magnetron dipole excitation of about 100 ms duration needs to be applied in order to excite the ions to an initial magnetron radius. Additionally, the whole system can be operated at high repetition rates of up to 100 Hz. This pushes the limit of mass measurements on radioactive isotopes possible to shorter half lives. The shortest-lived isotope measured at TITAN to date was ^{11}Li with a half life of 8.75(14) ms [Aud03]. For isotopes with a half life $t_{1/2}$, the optimal excitation time can be derived from Eq. 2.5 to be $T_{RF} = (2/\ln 2) \cdot t_{1/2}$. Shorter excitation times result in less resolving power and longer excitation times suffer from ion losses due to their radioactive decays.

In a Penning trap, ion masses are determined by measuring the frequency ratio of an unknown to a known isotope. This minimizes systematic uncertainties arising from inhomogeneities of electric and magnetic fields assuming that both ion species travel in the same region of the Penning trap. Based on the mass of the calibrant m_2, the mass of the ion of interest m_1 is deduced from the frequency ratio, $m_1 = \frac{q_1}{q_2} \cdot \frac{\nu_2}{\nu_1} \cdot m_2$. In order to limit the uncertainty contribution of the calibrant, a well known mass needs to be chosen.

The relative precision of this method is approximated by the relation

$$\frac{\delta m}{m} \propto \frac{1}{q\,B\,T_{RF}\sqrt{N}}. \tag{2.5}$$

Max. e^- energy	70 keV	Stored ions in trap	$10^6 - 10^8$
Max. B-field	6 T	e-beam intensity	$\sim 5 \cdot 10^{22}$
Herrmann beam Φ (FWHM)	$\sim 40\,\mu m$	Current density	$10^5\,A/cm^2$

Table 2.1: Specifications of the TITAN EBIT [Lap10].

For a given excitation time T_{RF} of an ion inside a magnetic field B, the precision of the measurement scales linearly with the charge state q and the squared number of ions N^2 measured. One effective possibility for increasing the precision of the mass measurement is by increasing the charge state q.

In order to increase the charge state, ions coming from the RFQ can be sent to TITAN's EBIT. During a first on-line experiment with $^{44}K^{4+}$ the EBIT was successfully commissioned and has been operational since [Lap10].

2.2.4 Electron Beam Ion Trap

At the TITAN facility the charge state of ions can be increased by charge breeding in the EBIT [Fro06, Lap10]. The EBIT is built similar to a Penning trap with cylindrical trap electrodes but operates on a slightly different principle. Ions are radially confined by the intense electron beam. The EBIT consists of a high intensity electron gun, the trap center, and an electron collector. A schematic of the EBIT is shown in Fig. 2.10.

A high intensity electron beam of up to 500 mA (an upgrade to 5 A is planned) is produced by the cathode in the electron gun. The electrons are emitted in a very low magnetic field region. The attractive potential of the trap center accelerates the ions towards the trap center where they are compressed by the strong 6 T magnetic field. This compression of the electron beam leads to current densities of up to $10^5\,A/cm^2$. After the electrons pass through the trap center they are decelerated by the collector that is floating near the electron gun potential. At the collector, a magnetic field with opposite direction to the trap's magnetic field increases the diameter of the electron beam and guides it into the collector electrodes. Fig. 2.11 displays the principle of charge breeding; specifications of the EBIT are listed in Tab. 2.1.

Ions in the EBIT are radially confined by the electron beam space charge. The trap electrodes are biased in such a way that they create a potential minimum in the center of the trap. Ions that pass through the EBIT are ionized by the intense electron beam. If the trap potential is set correctly, the ions get captured inside the potential minimum as soon as their charge state is increased by one. With each electron removed

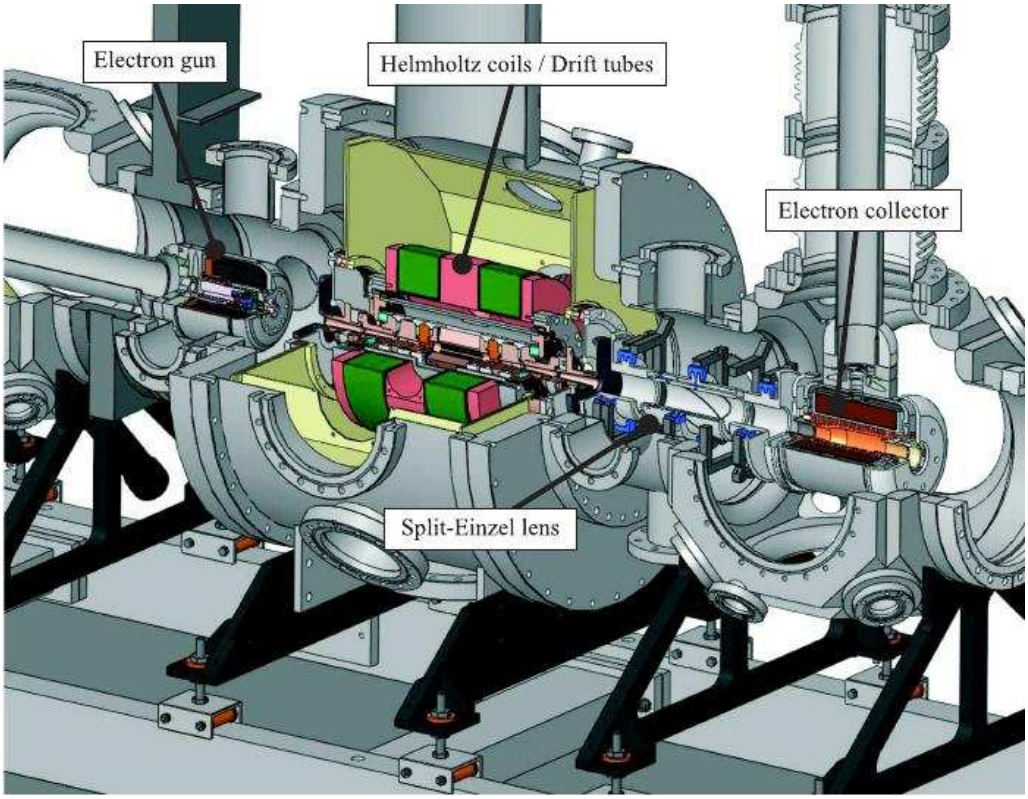

Figure 2.10: Section view of the EBIT model. On the right side the electron gun produces electrons and shoots them through the trap center before they are collected by the collector.

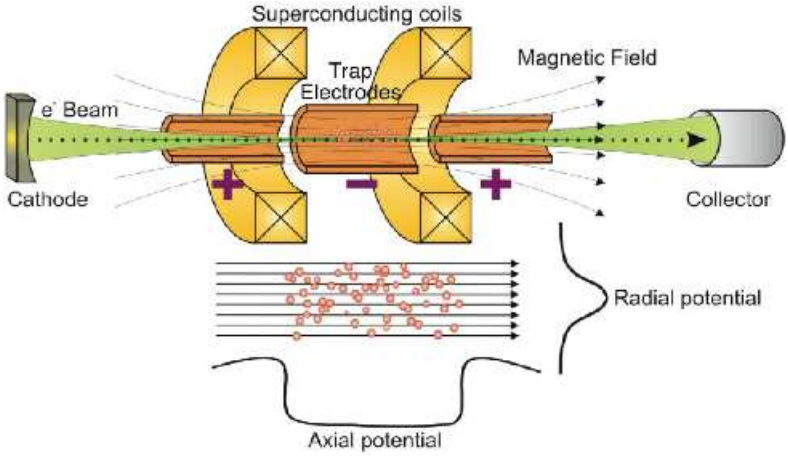

Figure 2.11: Working principle of the EBIT [Fro06].

from the atomic shell, the ions are captured deeper in the potential well. Depending on the electron beam energy and density, the charge state distribution varies. Electron configurations of He-like U^{90+} can be produced with the TITAN-EBIT.

Highly charged ions can be used for a variety of experiments [EBI08]. Their main purpose at TITAN is mass measurements on highly charged ions. But x-ray spectroscopy on highly charged isotopes can also be performed due to the open access to the trap center (see Chapter 3). The possibility to charge breed to certain atomic shell closures also allows one to use the EBIT for atomic mass spectrometry. A proposal for this method has been submitted to the TRIUMF EEC under the proposal number S1141.

In this work, the EBIT was operated without the electron beam as an open access Penning trap to perform in-trap decay spectroscopy. This is the central scope of this thesis and the details of this technique are described in the next chapter.

Chapter 3

In-Trap Decay-Spectroscopy Setup at TITAN

During electron-capture branching-ratio (ECBR) measurements at TITAN, radioactive isotopes produced by ISAC are sent to TITAN's RFQ for beam preparation and then injected into the spectroscopy Penning trap. Static electric and magnetic fields confine the ions inside the trap. The use of carrier material for implantation is not required. While the ions are stored inside the trap, their radioactive decays are observed. Electrons originating from β decays are guided out of the trap by the strong magnetic field and then detected by a β detector located on the beam axis. This β detector is mounted inside the vacuum vessel in a detection chamber and is described in Section 3.3. The detection chamber is introduced in Section 3.1.5 while the results of β trajectory simulations are presented in Section 3.3.1.

X-rays following an electron capture are emitted isotropically and are observed by two radially positioned Ge detectors. These two Ge detectors, used for the present measurements, have been thoroughly tested and were then installed on either side of the spectroscopy Penning trap as described in Section 3.4.

Within this work, the experimental setup to perform electron capture branching ratio measurements has been developed, tested, and installed at the Penning trap. A specially designed detection chamber between the Penning trap and electron-gun chamber houses a multi-channel plate (MCP) detector to observe and tune the beam.

3.1 Spectroscopy Penning trap

The EBIT is designed with a unique open geometry that provides visible access to the trap center. For electron capture branching ratio measurements it is used as a spectroscopy Penning trap. During these ECBR measurements the electron gun is retracted and instead either an MCP or a β detector can be positioned on the beam axis. The experimental setup is shown in Fig. 3.1 displaying the spectroscopy Penning trap with its two superconducting coils, retracted e-gun, detection vacuum chamber, and the position of the MCP.

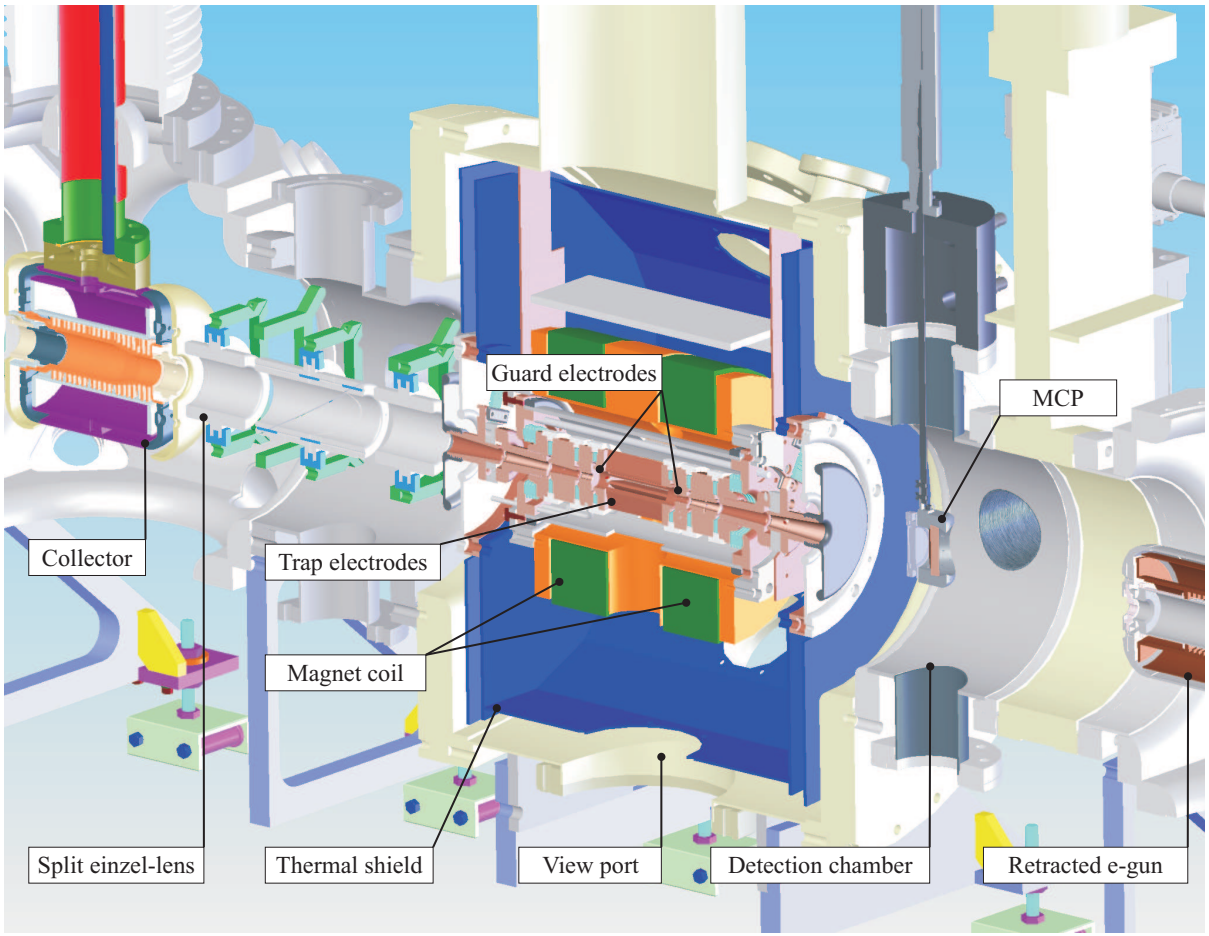

Figure 3.1: Model view of the spectroscopy Penning trap. The e-gun is retracted and at its position either MCP or β detector are placed.

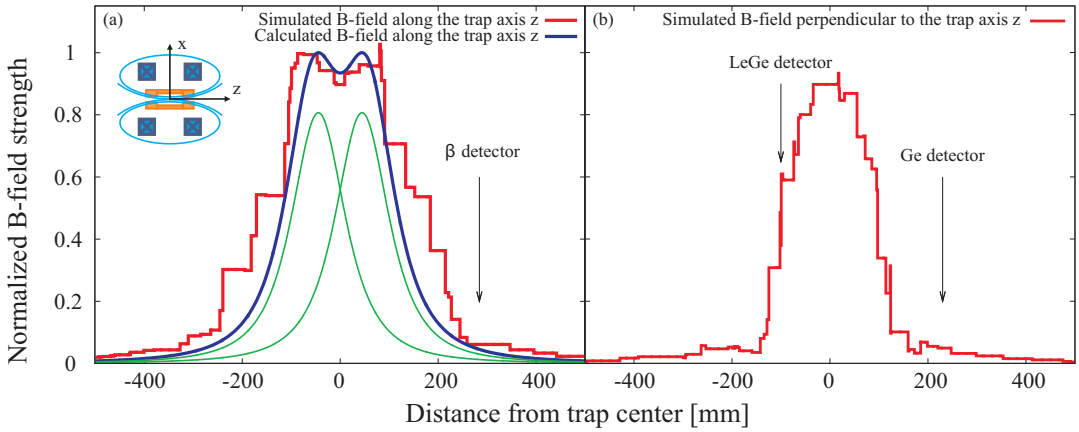

Figure 3.2: Magnetic field (a) along and (b) perpendicular to the trap axis, simulated with COMSOL [COM] (red histogram). The thick, blue line in (a) is the summed magnetic field for two single coils (thin, green line) calculated using Biot-Savards law [Stö00]. Arrows indicate the positions of the detectors used within this work.

3.1.1 Magnet system

Two superconducting Nb_3Sn coils in a quasi-Helmholtz configuration create the magnetic field of up to 6 T ($\sim$ 120 A current [Fro06]) that radially confines the ions inside the Penning trap. The coils have an inner diameter of 115 mm, an outer diameter of 216 mm, and are 55 mm wide. They are separated from each other at a distance of $\sim$112 mm. This distance is larger than the coil radius of $\sim$83 mm and results in a magnetic field minimum at the center of the trap and two maxima roughly at the position of the guard electrodes. At the trap center the field is reduced by $\sim$8% and thus a magnetic bottle is created. The field strength was calculated along the trap axis using COMSOL [COM] and the result is illustrated in Fig. 3.2 a. This figure also displays the calculated magnetic field of two dimensionless coils and the sum of their fields [Stö00]. Between the Helmholtz-coil pair at the trap center, the B-field minimum creates the magnetic bottle that is explained in more detail in the following subsection.

A two-stage Gifford-McMahon helium cryocooler [Lap10] keeps the superconducting coils at a temperature of 4.5 K. It is a cryogen free system, i.e., it is not cooled with liquid helium. Inside the magnet all trap electrodes except the two outermost are mounted to be electrically insulated but in thermal contact with the 4.5 K cold magnet. The magnet is protected from radiative heat load by a thermal shield at 26 K. Connected to this shield are the outermost two electrodes. Two diametrically opposed sets of diagonally crossed adjustable stainless steel rods of 2 mm diameter hold and fix the magnet inside the vacuum vessel. These rods provide thermal contact between the

magnet, thermal shield, and room-temperature housing. Fig. 3.3 displays the opened vacuum vessel, thermal shield, and magnet as well as the trap electrode structure.

Access ports in the thermal shield as well as the magnet allow visible line of sight to the trap center. In order to reduce the heat load on the magnet, the ports of the thermal shield are covered with Al-plates when vacant. Otherwise, the access ports are covered by a 25 µm thick Be window and used for x-ray spectroscopy with detectors placed outside the vacuum vessel. A special low energy Ge detector (see Section 3.4.3) is installed within the vacuum chamber inside one of the access ports of the Helmholtz coil magnet. Inside the magnet this detector is thermally shielded by an Al-tube that is in thermal contact with the thermal shield.

3.1.2 A magnetic bottle effect

The deviation of the coils from an ideal Helmholtz configuration, i.e., the coil radius equaling the distance between the coils, leads in our case to an $\sim 8\%$ magnetic field minimum in the trap center (see Fig. 3.2 a). This minimum creates a magnetic bottle effect in the trap center. Electrons or β particles that are emitted with a pitch angle, i.e., the angle between particle velocity $\vec{v}$ and the magnetic field $\vec{B}$, larger than the critical angle α_c stay trapped and cannot reach the detector. This critical angle depends on the so-called mirror ratio; that is, the ratio between the magnetic field $B_{\min}$ at the origin of the electron and the maximal magnetic field $B_{\max}$, and is given by

$$\frac{1}{\tan \alpha_c} = \left(\frac{v_{||}}{v_{\perp}}\right)_{crit} = \sqrt{\frac{B_{\max}}{B_{\min}} - 1}\,, \tag{3.1}$$

with $v_{||}$ and $v_{\perp}$ being the velocity parallel and perpendicular to $\vec{B}$. At the trap center, the critical angle is calculated to be about 73° but decreases with increasing radial distance from the trap center. Therefore, the number of electrons trapped in the magnetic bottle increases with increasing radial ion-cloud distribution. This effect limits the maximum number of electrons that can leave the trap. If all electrons would originate from the trap center, only about 77%[1] of them could leave the trap. Since a β detector is installed at only one side of the trap, only electrons emitted in one hemisphere are detected. In Fig. 3.4, α_c is calculated using the maximal B-field value along the beam axis as $B_{\max}$ and assuming that the magnetic field runs parallel to the trap axis.

[1] $4\pi r^2 / \left(2 \cdot \int_0^{2\pi} \int_0^{\alpha_c} r^2 \sin\theta \, d\theta \, d\phi\right)$

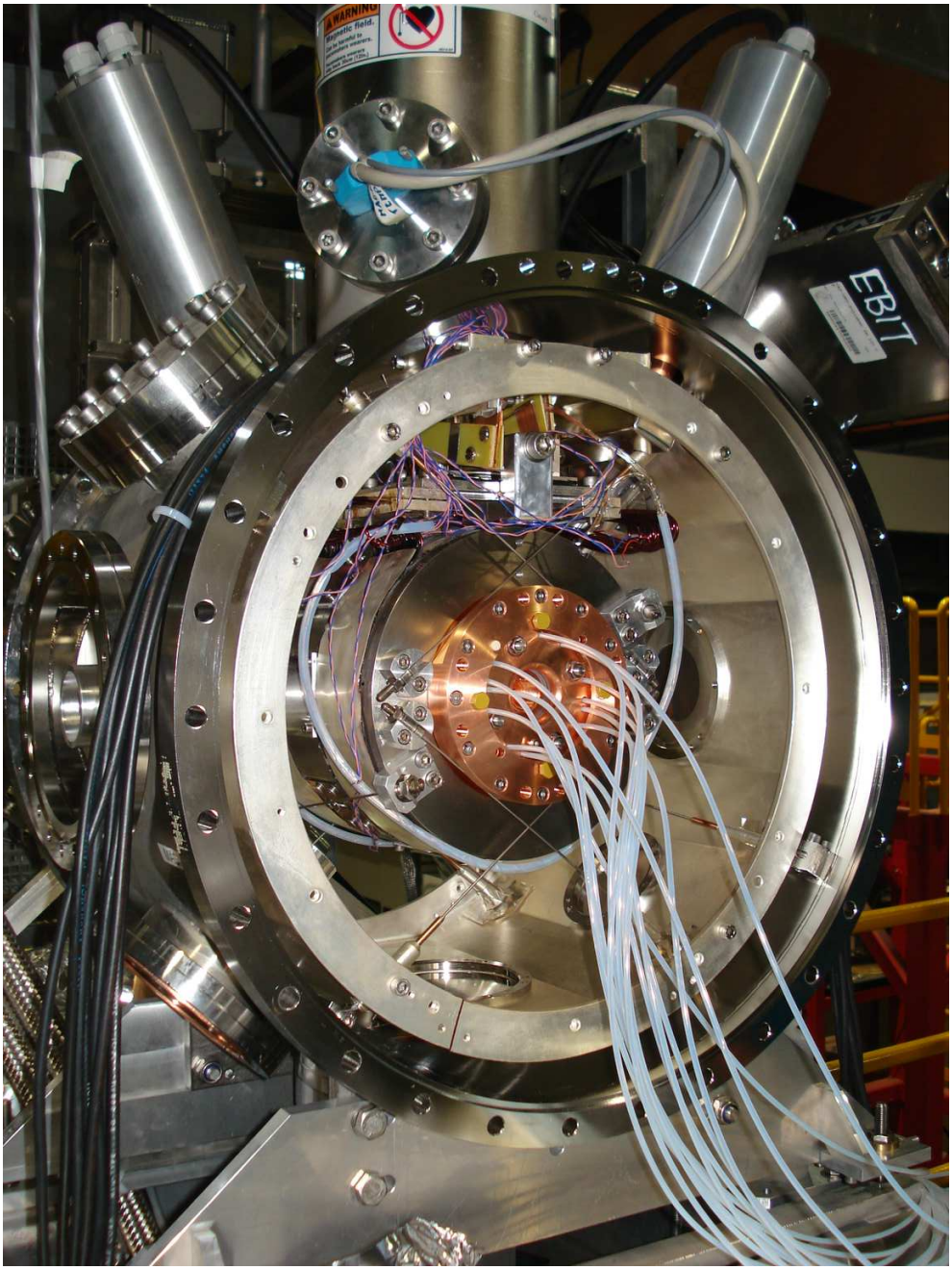

Figure 3.3: Picture of the EBIT vacuum vessel. The thermal shield is the silver-coated cylinder. Magnet and copper electrodes are held in place inside the vacuum vessel by 2 mm thick stainless steel rods. The electrodes are electrically connected with stainless steel wires that are electrically insulated by PTFE Teflon tubes.

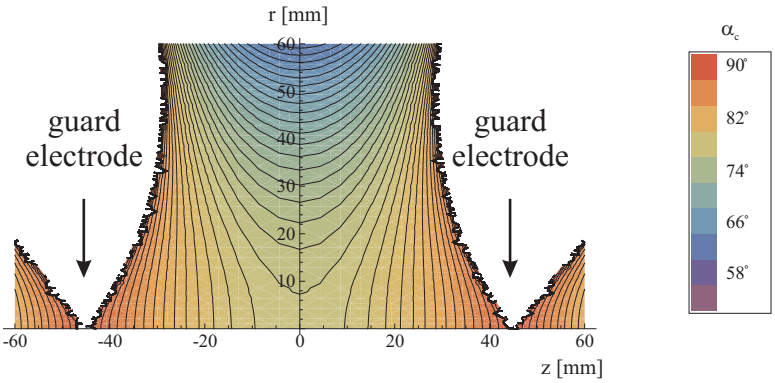

Figure 3.4: Critical angle α_c inside the trap calculated using the script from [Koe10] and Eq. (3.1) with B_{max} ($r = 0\,\text{mm}, z = 45.2\,\text{mm}$). As an approximation, it was assumed that $\vec{B}$ runs parallel to the trap axis. This is a valid approximation for $z = 0$.

3.1.3 Electrode structure of the trap

The Penning trap electrode assembly consists of nine electro-polished, oxygen-free, high-purity copper electrodes (see left Fig. 3.5). It has a conical shape that is optimized for operation with the electron beam [Lap10]. The inner radius of the outermost electrode is 7.5 mm and gradually reduces to 2.5 mm for the guard electrode. The latter electrode is so-named because it is used to create the axially confining potential. The central drift tube has an inner radius of 7 mm and is eight-fold segmented. In between the segments, radial aperture slits provide visible access to the trap center. These slits are equally spaced at 45°, 58 mm long, and 3 or 4 mm wide. The left photograph in Fig. 3.5 shows the whole trap electrode assembly with the segmented central drift tube. A model of the central drift tube is displayed on the right in Fig. 3.5, and all relevant dimensions are provided in Fig. F.3. Inside this central drift-tube, ions are stored during charge breeding and in-trap spectroscopy measurements.

Each electrode of the trap assembly is electrically insulated via sapphire discs that also provide good thermal contact. In order to improve thermal contact between the sapphire disc and the copper drift-tubes, a fine layer of cryogenic Apiezon N [Api10] was applied.

The eight-fold segmented central drift tube allows one to apply ion-cooling techniques such as dipole cleaning [Sav91] and side-band cooling [Ame05].

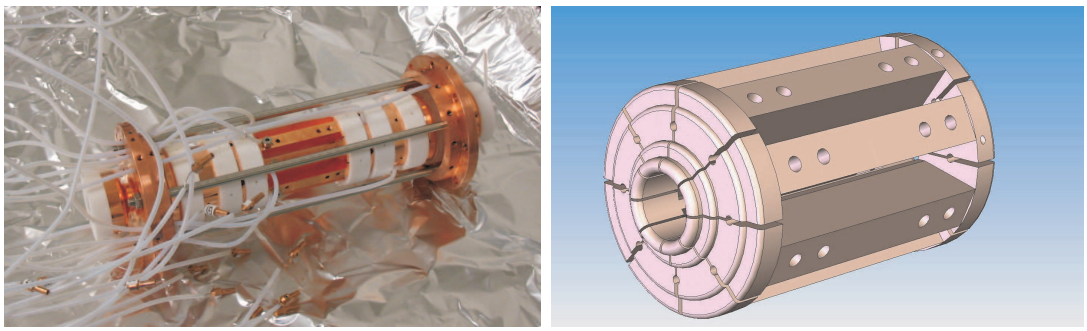

Figure 3.5: Photograph of trap assembly (left) and a model of the eight-fold segmented central drift tube (right).

3.1.4 Ultra-high vacuum system

In order to reduce charge exchange reactions of stored ions, and thus store them for sufficient long duration in the Penning trap to perform in-trap decay spectroscopy, ultra-high vacuum (UHV) conditions are required. Depending on the vacuum inside the trap, the collision rate with residual gas changes. During these collisions, charge exchange between stored ions and residual gas happens. As soon as a stored ion gets neutralized in such a reaction, it can no longer be confined by electric and magnetic fields and leaves the trapping region. Depending on where the ion is lost, inside the trap or along the beam line, its decay contributes to background but in any case it is lost for spectroscopic purposes.

To achieve these conditions, every material that is installed inside the vacuum must have low out-gassing rates. During general operation the magnet is cooled to 4.5 K and acts as a cryo-pump, i.e., residual gas freezes to cold surfaces upon impact. This reduces the gas pressure in the collector and electron gun chamber to the 10^{-10} mbar range. The pressure within the trap center cannot be measured but is estimated to be below 10^{-11} mbar. Thus, long storage times of ions in the Penning trap are possible (see Section 4.3). A more detailed description of the vacuum system is given in [Lap10].

3.1.5 Detection chamber

For in-trap decay spectroscopy measurements, the electron gun is retracted and a detector is moved on the trap axis. The original vacuum vessel connecting electron gun chamber and magnet chamber could not fit the required beta and ion detectors due to size limitations. Within this work a new chamber was developed to house the beta detector and one MCP. Both β detector and MCP are mounted on linear vacuum feedthroughs. If one of them is required for measurements, it can be moved into the

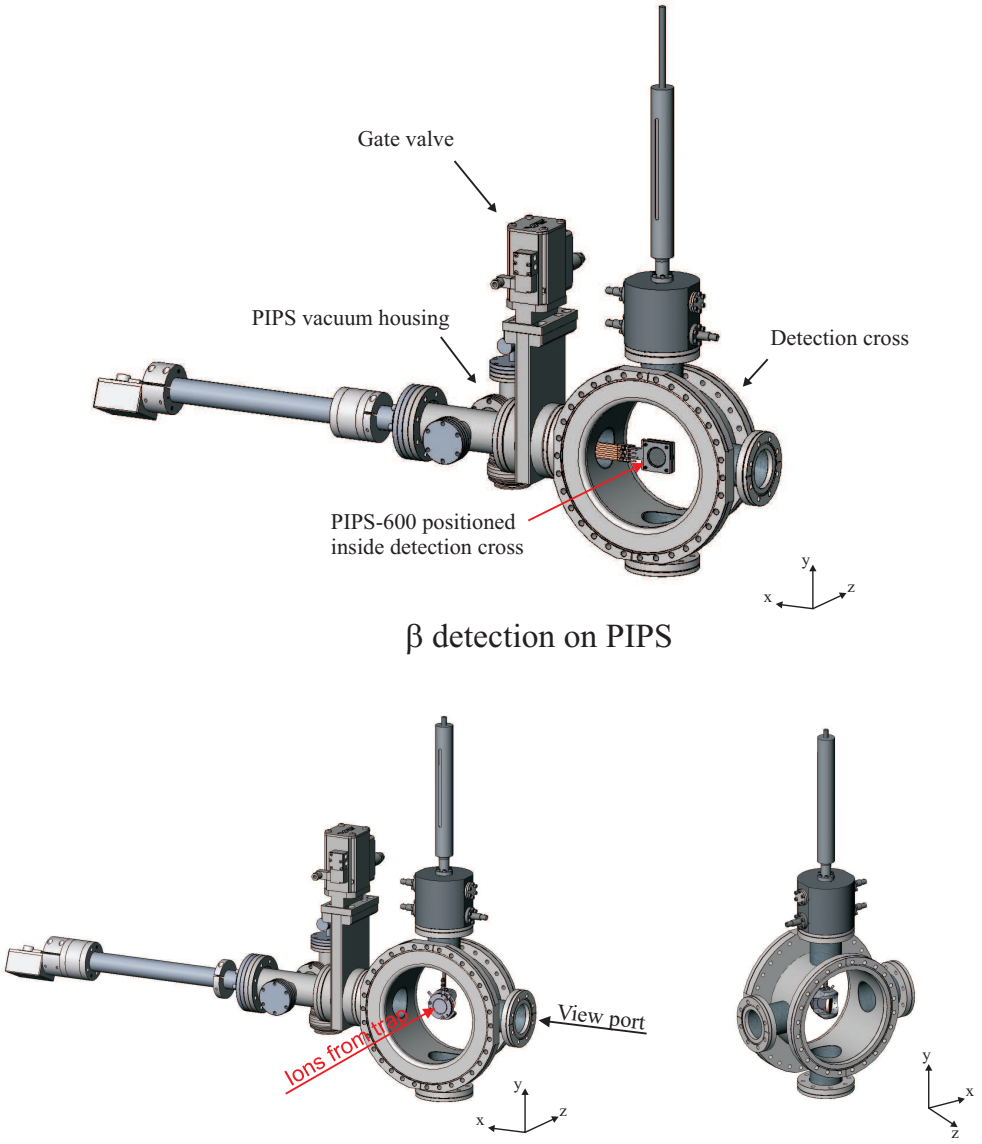

Figure 3.6: Detection chamber between magnet and electron gun chamber. Either MCP or β detector (PIPS detector) can be inserted into the chamber.

chamber and positioned onto the beam axis. The chamber with either β detector or MCP inserted is shown in Fig. 3.6. When the EBIT is used for charge breeding, both MCP and β detector are retracted and the electron gun is moved into the detection chamber.

3.2 MCP detector

In order to determine the beam profile and shape of ions passing through the trap, an MCP[2] in a Chevron configuration with phosphor screen can be centered on the beam axis inside the detection chamber. A special holder was developed that holds the MCP as well as an optical mirror in the visible range. It is moved into the detection chamber by a linear motion feedthrough[3]. The MCP assembly, including the mirror, is shown in Fig 3.7. The MCP detector consists of two plates with small channels coated with a thin layer of material with a low electron work function. Each channel works similar to the dynodes in a photomultiplier creating an electron shower inside the channel. Ion imaging with an MCP functions as follows: ions leaving the Penning trap are accelerated onto the front plate of the MCP. Since their kinetic energy is greater than the impact ionization potential of the material, they create an electron shower upon their impact on the first plate. The electrons of the shower are then accelerated through the channels onto the second plate of the MCP. There, the electron shower is amplified further before it hits a phosphor screen or an anode[4] [Wiz79]. This principle is illustrated in Fig. 3.8. Upon electron impact on the phosphor screen, fluorescence light is produced. A mirror behind the screen reflects the image by 90°. With a CCD-camera, this picture can then be observed through a CF 4.5" glass view port installed at the detection chamber.

3.3 Beta detector

During in-trap spectroscopy operation, a β detector is placed in the detection chamber. Its purpose is the detection of electrons originating from β decays occurring inside the trap. One requirement for all components in the spectroscopy trap is to have low outgassing rates in order to maintain the ultra-high vacuum. The limited space inside the detection chamber requires the detector to be compact. It also needs to be retractable in order to alternate with the MCP detector system and withdraw for charge breeding operation. At the detector's position, a residual magnetic field of $\sim$1 T is present and thus constrains available β detection techniques.

MCP detectors, scintillators, and solid state detectors were considered for β detection; however, proportional gas counters were not due to space and vacuum limitations. Benefits and disadvantages of each detector type are the following:

- **Multi-channel-plate**
  Multi-channel-plates [Wiz79] require vacuum conditions to operate and are widely

[2] Photonis APD 3025 12/10/12 60:1 STD P.20, ⌀ 26.42 mm active area
[3] Huntington Rack & Pinion Linear Positioner L-2131-6 CF1.33"
[4] Typical MCP voltages applied in this work were GND/+2000 V/+2200 V

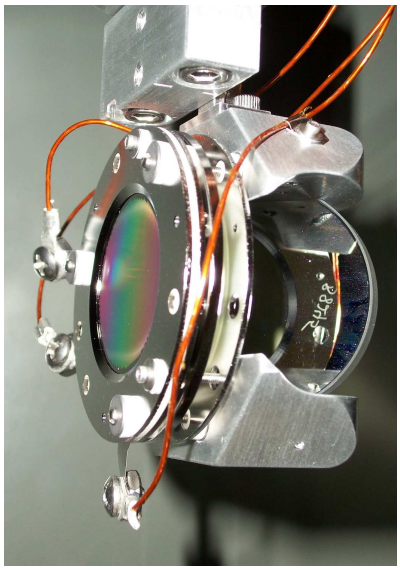

Figure 3.7: Picture of MCP assembly including the mirror.

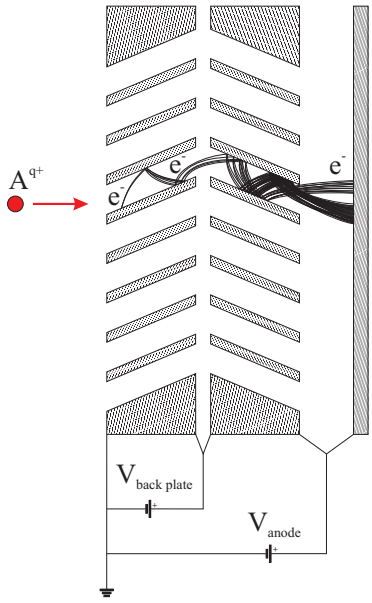

Figure 3.8: Working principle of a MCP. An explanation is given in the text.

used in ultra-high-vacuum setups for beam diagnostics [Kru00, VdB01] or particle detection [Tor90]. Moreover, operation in environments with magnetic fields has been reported [Col82, All90, Fra90]. When an MCP is operated in B-fields, its gain is expected to decrease when the gyration radius $r_{\text{gyration}} = \frac{m\,v_\perp}{q\,B}$ of the secondary electrons produced by an incident particle is smaller than half the pore diameter [Col82, Fra90]. MCPs typically used at the TITAN facility have a pore diameter of 10 µm and a pitch angle of 12° to the surface normal. Assuming a secondary electron, with an energy of 2.5 eV [Ebe79], is emitted perpendicular to the surface and magnetic field, one thus expects no significant influence on the detection efficiency for magnetic field strengths of less than 1.1 T. Calculated field strengths at the actual position $z = 284$ mm of the MCP in the detection chamber are in the range of 0.2 T, i.e., well below the critical B-field (see Fig. 3.2 to estimate the B-field along the beam axis). Calculated gains for single MCP plates for several bias voltages as a function of the axial magnetic field show no change in gain up to about 0.5 T for 1300 V bias voltage and a pore diameter of 12.5 µm [Fra90]. Based on these calculations, an MCP system operates without problems under the conditions present in the TITAN-EC setup.

While MCPs provide high detection efficiencies ε_{det} for ions and electrons with kinetic energies from 0.5 keV to ∼15 keV [Str99], ε_{det} drops for higher incident particle energies [Sch96a]. It has been demonstrated that an additional foil placed

in front of the MCP increases $\varepsilon_{\mathrm{det}}$ by a factor of three for 10 keV positrons. Tornow [Tor90] achieved more than 90% detection efficiency for 100 keV electrons by placing a BaF_2 coated Al-foil in front of the MCP. However, efficient detection in the MeV region has not been demonstrated. Therefore, an MCP detector is installed inside the detection chamber without any foils to only detect ions during tuning and optimization processes, for β detection it is not used.

- **Scintillator**
  Scintillators provide a high detection efficiency for fast electrons but most common scintillator materials out-gas or have unknown out-gassing rates. Additionally, the read out with photomultiplier tubes in residual magnetic fields as present in the setup is difficult [Col82]. Alternatively, avalanche photo diodes are considered to read out light signals from the scintillator since they would not be affected by the residual magnetic field. The main limitation for scintillators is the limited space in combination with the UHV and the requirement to be able to retract the detector during charge breeding operation. Therefore, the development of a scintillator for β detection was not pursued.
- **Solid state detector** Surface-barrier Si detectors (SBD) are commonly used in β-counting applications such as β telescopes [Hor96]. Their response function to fast electrons has, for example, been investigated in the range 0.8-3.5 MeV with the Giessen electron linear accelerator [Fro91]. At REX-ISOLDE, a Si detector has been used to detect conversion electrons originating from ions stored in the Penning trap REXTRAP [Wei01].

  Si detectors also operate in magnetic field environments. If the magnetic field is perpendicular to the surface normal of the crystal, the electrons are deflected by the Lorentz force. This impairs the tracking resolution of Si-strip detectors and has been investigated for magnetic fields of up to 8 T [Boe00,Boe01,Bar02]. In the TITAN-EC setup, the residual magnetic field is much smaller and the direction of the field is parallel to the surface normal. Therefore, no influence of the magnetic field on the Si detector is expected.

  Compared to scintillators, solid state detectors are easy to install and operate and do not require light guides or photo multipliers. Therefore, only a single element needs to be installed inside the vacuum chamber.

In summary, magnetic field rigidity, compact size and UHV compatibility made a surface-barrier detector (SBD) the premier choice for β detection in the TITAN-EC setup. Within this work the β detector was simulated, developed, and tested.

3.3.1 In-trap β-trajectory simulations

Beta decays are three body decays and thus produce electrons with a continuous energy distribution T_e. The maximum kinetic energy of a β particle is given by the energy

difference Q_β between initial and final states, assuming a massless neutrino. Based on Fermi's theory of β decay the energy distribution can be calculated [Kra87] by

$$N_e(T) = \frac{C}{c^5}\sqrt{T_e^2 + 2\,T_e\,m_e\,c^2}\,(Q_\beta - T_e)^2\,(T_e + m_e\,c^2). \tag{3.2}$$

Typical β decay Q_β values of intermediate $\beta\beta$ transition nuclei are about 3 MeV. This Q_β value was used to create the electron energy distribution in simulations. The Q values of isotopes involved in $\beta\beta$ decays are listed for example in [Fre07, NND10].

In order to determine the size of the β detector required to detect electrons leaving the Penning trap, SIMION [Dah00] simulations have been performed [Bru10b]. The underlying electrode geometry as well as the magnetic field map were taken from [Sch08]. Based on this field map, size and position for the optimal detector were evaluated.

Electron trajectories were simulated for various ion-cloud distributions in typical magnetic field strengths of 4 T, 5 T and 6 T. For this purpose, electrons were generated with a hemispherical direction distribution $\frac{\vec{v}}{v}$ and a Gaussian energy distribution that approximates one calculated with Eq. (3.2). Fig. 3.9 displays the calculated energy distribution as well as that of 3000 β particles that were created during the simulation. Spatially, a three dimensional Gaussian distributed ion cloud was assumed and thus defined each electron's starting point. The distribution was assumed to have a constant width σ_z along the beam-axis and varying radial distributions $\sigma_x = \sigma_y = \sigma$.

The number of electrons reaching the β detector was simulated for varying ion-cloud distributions $\sigma_x = \sigma_y = \sigma$ and different magnetic field strengths. These simulations show that the fraction of electrons leaving the trap depends on several factors:

- The existing quasi-Helmholtz-coil configuration creates a local magnetic field minimum at the trap center and thus a magnetic bottle inside the trap. Electrons that are emitted with a pitch angle, i.e., the angle between particle velocity and the magnetic field axis, larger than the critical angle α_c stay trapped and cannot reach the detector (see Eq. (3.1)). The fraction of electrons that can leave the trap is calculated to be about 77% when all were emitted from the trap center. For electrons emitted further away this fraction decreases as α_c decreases. This calculation agrees with the results of the SIMION simulations at 4 T, 5 T, and 6 T. For ion-cloud distributions with a radial distribution of $\sigma_r \lesssim 0.75$ mm, the fraction of electrons that reaches the detector is 66 ± 2%. The slight deviation from the calculated 77% arises, because a point-source was assumed for the calculation in Section 3.1.2. The result presented in Fig. 3.10 shows that the fraction of electrons reaching the β detector is independent of the magnetic field strengths ranging from 4 T to 6 T. This fact allows one to perform in-trap decay spectroscopy measurements with a magnetic field setting that allows for optimal ion storage.

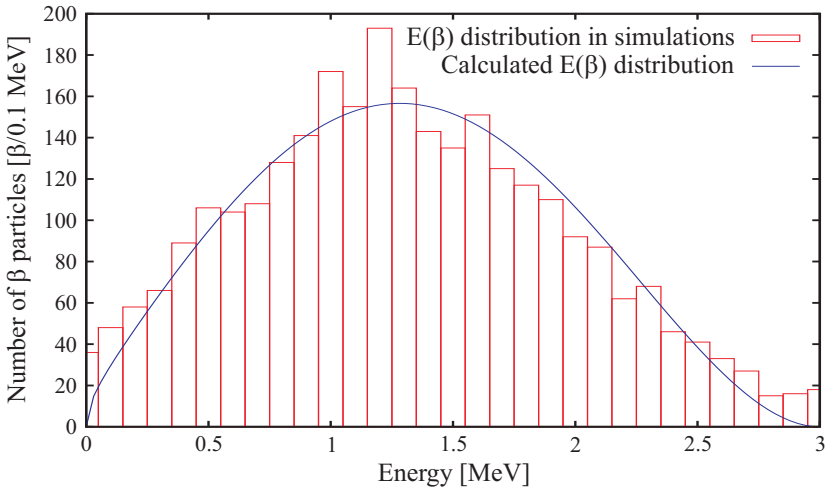

Figure 3.9: Calculated energy distribution of a β spectrum without taking the Coulomb force into account. A Gaussian energy distribution approximating the calculated β spectrum of Eq.(3.2) is used in the simulations. The energy distribution of 3000 simulated β particles in SIMION is displayed with boxes, a maximum of Q_β=3 MeV is used.

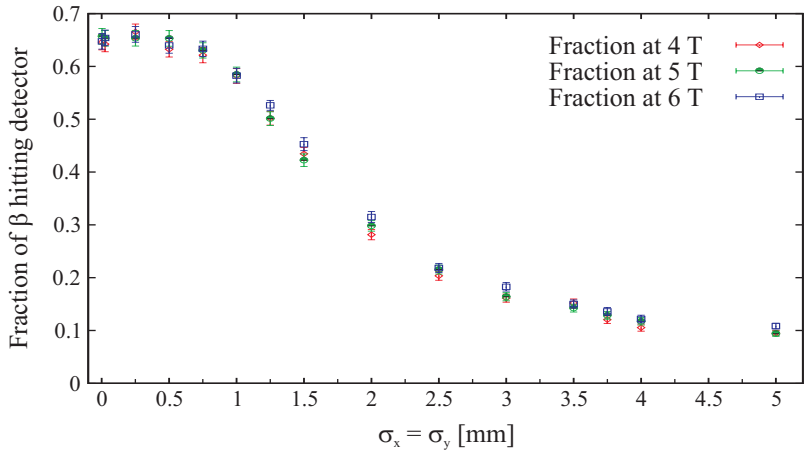

Figure 3.10: Fraction of electrons reaching the β detector as a function of the initial x-y-symmetric Gaussian ion-cloud distribution σ.

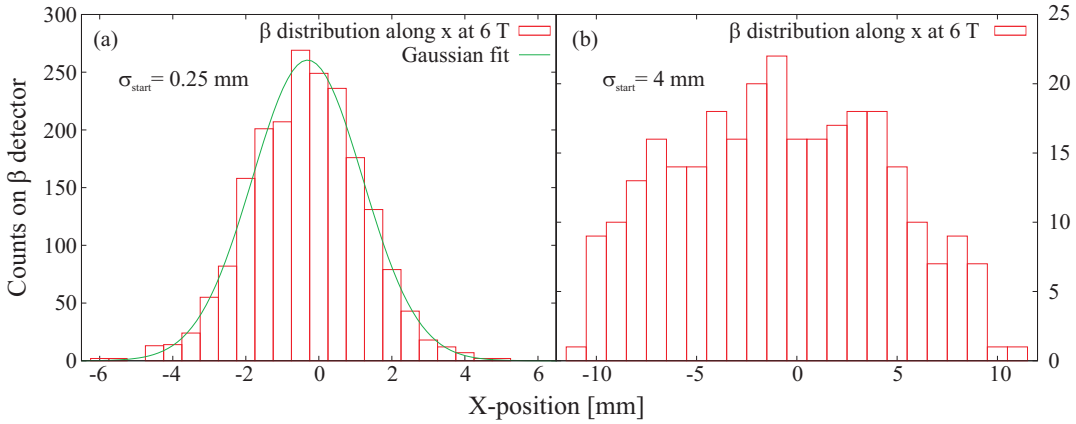

Figure 3.11: Simulated electron impact distribution on the β detector along the x-axis for the ion cloud distributions (a) $\sigma = 0.25\,\text{mm}$ and (b) $\sigma = 4\,\text{mm}$.

- With increasing ion-cloud diameter, the extraction trap electrode (diameter 5 mm) acts as an aperture. Electrons that are emitted further away from the trap axis hit the electrode while following the field lines and are lost (see Fig. 3.10). Projecting the x-y-hit distribution on the β detector onto the x-axis reveals a Gaussian intensity distribution as shown in Fig. 3.11 a for an ion distribution with $\sigma = 0.25\,\text{mm}$. Larger ion-cloud distributions are still Gaussian distributed in the center but the periphery of the distribution is cut by the effect of the extraction trap electrode. This behavior is displayed in Fig. 3.11 b where an ion-cloud distribution of $\sigma = 4\,\text{mm}$ is simulated.

- For electrons emitted radially with an energy larger than about 3.5 MeV, a magnetic field strength of 5 T is no longer sufficient to confine the electrons. Thus, they can leave the trap center radially from where they hit the central trap electrode. This does not affect ECBR measurements of transition nuclei in $\beta\beta$ decays because the largest Q_β value is 3.278(4) MeV in the case of ^{116}In [NND10].

  In this work, in-trap decay spectroscopy measurements were performed on the isotopes ^{107}In, ^{124}Cs, and ^{126}Cs with β end-point energies of 2.198(10) MeV, 4.907(9) MeV, and 3.802(14) MeV, respectively [NND10]. In the case of ^{124}Cs simulations showed that the magnetic field is not sufficient to confine all electrons originating from β decays.

These simulations indicate, that independent of the ion-cloud size and magnetic field strength, in the range from 4 T to 6 T, a β detector with a diameter larger than $\varnothing \sim 24\,\text{mm}$ is sufficient to detect all β particles originating from the trap center. Based on these simulations a Si detector with $600\,\text{mm}^2$ active area ($\varnothing = 27.6\,\text{mm}$) was chosen to detect electrons during ECBR measurements.

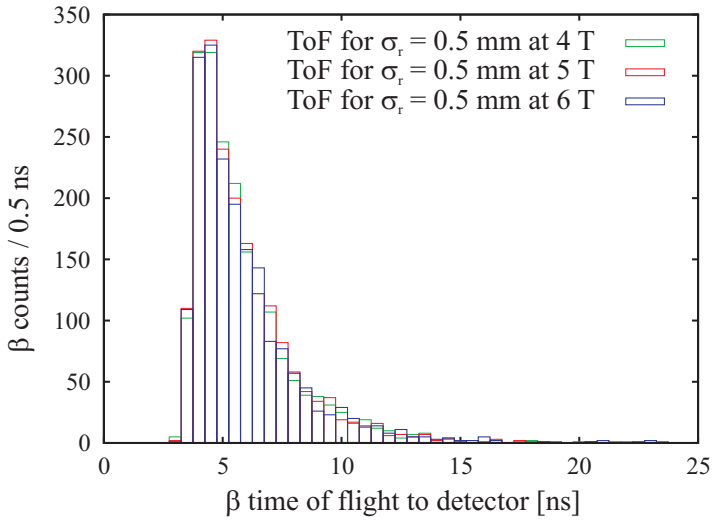

Figure 3.12: Simulated time-of-flight for β particles from their place of birth to the β detector.

Additionally, the time-of-flight of the β particles from their place of origin to the detector was simulated. It is also independent of the magnetic field strength for 4 T, 5 T, and 6 T. Simulated flight times range from 2.5 ns to 23 ns with an average of about 6 ns. The simulated time-of-flight spectrum is displayed in Fig. 3.12.

3.3.2 Passivated Implanted Planar Silicon detector

For the detection of β particles a Passivated Implanted Planar Silicon (PIPS) detector has been chosen because it best fits the previously defined requirements. A planar Si-wafer is attached to a ceramic board and therefore minimizes contamination of the vacuum by out-gassing. Moreover, it has been demonstrated that surface barrier detectors (SBD) work in magnetic environments [Sai91].

First, a PIPS detector with 300 mm^2 (PIPS-300, 500 µm thick) active area was tested to verify that this detector type is suited for β detection. After tests with a ^{207}Bi source inside a test vacuum chamber, this detector has been installed in the TITAN beam line upstream of the MPET. A $\approx$ 20 µm thick Al-foil was mounted in front of the PIPS detector. During the mass measurements of ^{8,9,11}Li [Smi08], radioactive ^{9}Li was implanted onto the Al-foil and β particles originating from the ^{9}Li-decay were counted with the PIPS detector. This technique of β counting allowed one to identify the isotope composition of ion bunches sent from the RFQ to the MPET. Results of this method are summarized in [Bru08a].

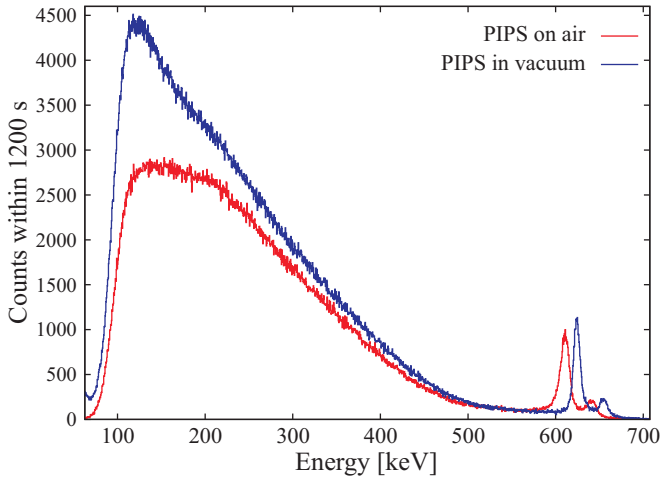

Figure 3.13: Spectra of a ^{137}Cs source recorded with a PIPS-600 detector in vacuum and on air.

Based on the successful performance of the PIPS-300 detector during the on-line Li experiment, it was chosen as the beta detector for in-trap decay spectroscopy. Simulations show that a detector with an area of more than $\varnothing \sim 24\,\mathrm{mm}^2$ is required to detect all electrons originating from β decays occurring inside the trap. In order to compensate for uncertainties in the positioning of the detector inside the detection chamber, a slightly larger PIPS detector with $600\,\mathrm{mm}^2$ active area[5] is used. A Si-waver of this size is commercially available from Canberra but not mounted on a UHV-compatible ceramic carrier board. Hence, a ceramic board has been designed and then fabricated by ALL Laser Inc.. At the Max-Planck Halbleiter laboratory in Munich, electric contacts were printed onto the ceramic board. All dimensions of the ceramic board and contact pads are listed in Appendix C.

After manufacturing two PIPS-600 detectors, they were tested with a ^{137}Cs source in a test vacuum chamber in Munich. The resulting spectra of one detector at 1 atm and in a vacuum of $\sim 1 \cdot 10^{-4}\,\mathrm{mbar}$ are displayed in Fig. 3.13. On the right side of the spectrum the conversion electron lines CE K (624.2 keV) and CE L (655.7 keV) of ^{137}Cs are visible [NND10]. When the chamber was evacuated, the spectrum shifted to higher energies because the electrons lost less energy in collisions on their way to the detector.

The PIPS-600 detector was mounted in the detection chamber for the first time during the ^{107}In experiment. Radioactive ^{107}In was implanted onto the Al-foil in front of the detector and identified by its half life [Ett09, Bru10b]. This measurement demonstrated the feasibility of using the Si detector for β detection in ECBR measurements.

[5] Canberra PIPS-600-CB, 500 µm thick

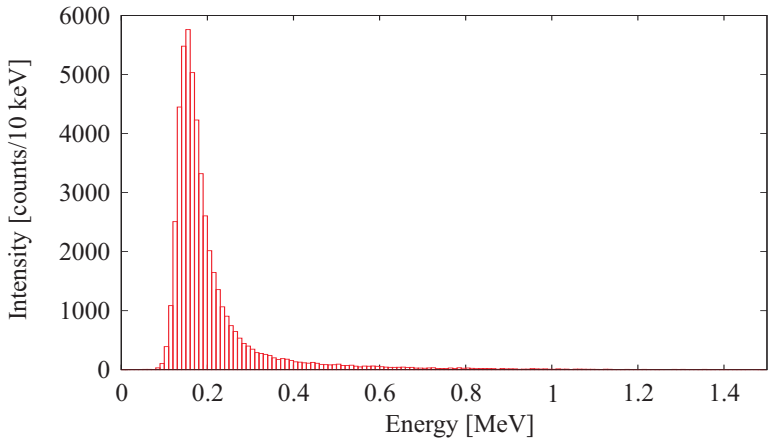

Figure 3.14: Energy deposition of $5 \cdot 10^4$ electrons impinging with 1.5 MeV on a 500 µm thick Si wafer with a dead layer of 50 nm simulated with Penelope2008.

Due to the thin Si-waver thickness of 500 µm, only electrons impinging with an energy less than $\sim$ 600 keV are completely stopped. More energetic electrons only deposit some of their energy while passing through the detector. An energy-loss spectrum of 1.5 MeV mono-energetic electrons simulated with Penelope2008 [Sal08] is displayed in Fig. 3.14. This simulation agrees with results obtained with CASINO [Dro07].

3.3.3 PIPS detector mounting system

In the detection chamber, two PIPS-600 detectors were mounted on each side of an Al-mounting plate. This mounting plate was then installed at a rotary-linear magnetic feedthrough[6]. A $\approx$ 20 µm thick Al-foil was mounted in front of one of the Si detectors. Both detectors, with and without Al-foil, could be rotated in such a way that they would face the Penning trap exit. If the one with Al-foil was facing the trap, ions could be implanted onto the Al-foil and by observing the β-decay rate the implanted isotope could be identified by its characteristic half life.

During all experiments performed within this work, a 6 mm thick solid Al-mounting plate was used. If a rather long-lived isotope ($t_{1/2} \gtrsim 3$ mins) was implanted onto the Al-foil prior to an ECBR measurement, all β particles from this decay would be stopped in the aluminum and could not contribute to the background on the Si detector mounted on the other side of the mounting plate. In this setup, both Si detectors only detect β particles impinging onto the front face of the detector.

[6]Huntington VF-169-12 CF2.75" rotary-linear magnetic feed through

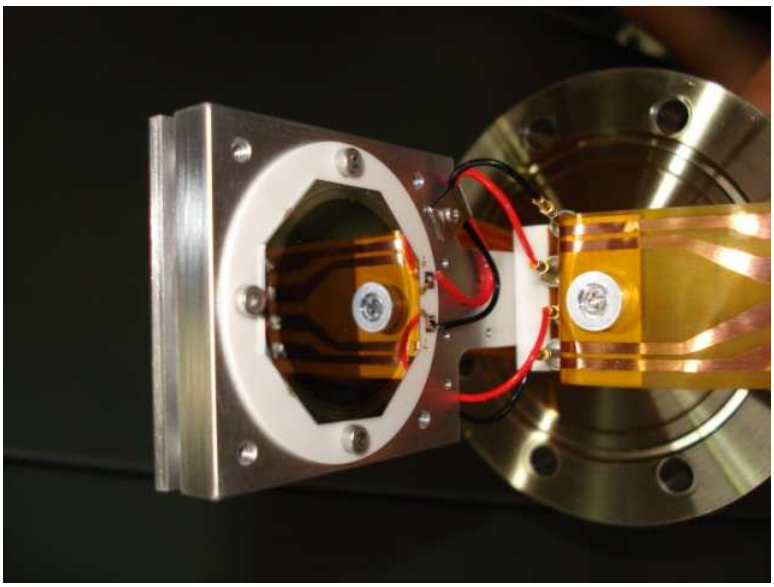

Figure 3.15: Picture of the β detector including flexible-circuit-board mounted on the magnetic linear feed through.

Mounting plate and β detectors can be retracted into a separate vacuum chamber that can be separated from the detection chamber via a gate valve[7]. This allows one to install, test and, if necessary, repair or exchange the Si detectors without having to break the vacuum of the Penning trap.

Inside the vacuum, the detectors are biased by means of a flexible-circuit-board that is fed onto the rod of the magnetic feed through. The conducting strips of the flexible-circuit-board have been etched from a Polyimide Flexible Laminate[8]. On the detector side this circuit board is screwed onto a Macor block with ring-connectors. A female connector has been silver-soldered to the ring connectors. This allows one to exchange β detectors without having to solder or unmount the circuit board. At the other end of the circuit board, Teflon-coated wires are soldered to the copper conduction strip. These wires are then connected to a 5 kV electrical feedthrough with push-on connectors. All parts have been processed and cleaned to meet the UHV requirements. Pictures of the manufacturing process and the assembled β detector are shown in Appendix. D. The mounted β detector assembly is displayed in Fig. 3.15.

[7] VAT series 108 CF4.5" pneumatic gate valve

[8] DuPont^{TM} Pyralux LF8515R All-Polyimide Flexible Laminate, Copper 153 g/cm^2, 25 µm thick adhesive, 25 µm thick Kapton [DuP01], NASA out-gassing rate %TML=0.94% and %CVCM=0.06% [Gus09]

	LeGe	Ge
Manufacturer	Canberra	Canberra
Type	Planar High purity Ge	Reverse Electrode Coaxial Ge
Model	GUL0110P	GR2018
Serial number	08078301	1086799
Position	North side of trap	South side of trap
Bias	-1000 V	-3000 V
Output polarity	+	-
Output range	0-5 V	0-5 V
Pre amp	ITRP	2001C

Table 3.1: Specifications of the Ge detectors used within this work. Their location is schematically illustrated in Fig. F.2.

3.4 X-ray detectors

During the first in-trap decay-spectroscopy experiments and throughout this work, two Germanium detectors were used for the detection of x-rays and γ-rays from EC and β decays. Their specifications are listed in Tab. 3.1. On the South side of the Penning trap a reverse electrode coaxial high-purity Ge detector (referred to as Ge detector, see Section 3.4.2) was mounted in air. X-rays and γ-rays originating from the trap center passed through two Be windows before they were detected by the Ge detector. The second detector, a Canberra low-energy Ge detector (referred to as LeGe detector, see Section 3.4.3) was installed inside the vacuum close to the trap center. The location of the detectors as well as their orientation is illustrated in a schematic of the EBIT beam-line and the spectroscopy Penning trap in Fig. F.2.

The energy resolution of these detectors is determined by inherent statistical fluctuations σ_D, incomplete charge collection σ_X and broadening σ_E induced by electrical components. They all contribute to the total width $\sigma_T^2 = \sigma_D^2 + \sigma_X^2 + \sigma_E^2$. Independent of crystal shape and electronics, statistical fluctuations limit the resolution to [Kno00]

$$(\mathrm{FWHM})^2 = \left(2\sqrt{2\ln 2}\right)^2 \sigma_D^2 = \left(2\sqrt{2\ln 2}\right)^2 F\,\varepsilon\,E\,, \tag{3.3}$$

with ε being the energy required to create an electron-hole pair within the crystal, E the photon energy and F the experimentally determined Fano factor. For Ge crystals these values are $\varepsilon = 2.95\,\mathrm{eV}$ and $F = 0.125$ [Jen95].

3.4.1 Be window

Two Be windows are installed between the Ge detector and trap center. The outer 500 µm [Fro06] thick Be window[9] is welded into a CF 8" flange and installed at the horizontal southern port of the trap's vacuum vessel. A second Be window of 25 µm thickness covers the access port in the thermal shield. It improves the vacuum in the center of the trap and reduces the thermal load on the magnet. The ultrahigh purity Be windows provide high transmissions of more then $\sim 96\%$ in the x-ray region above 15 keV. Fig. A.4 displays the calculated transmission through 525 µm IF-1 beryllium which was calculated with mass-attenuation coefficients determined by XCOM [Ber09] specifically for the element composition of the IF-1 Be window [Bru08b].

3.4.2 Ge detector

The Ge detector is installed at the South side of the Penning trap. This contact method and the use of a 1.5 mm Al window [Cand] allows for the detection of photons with energies as low as about 6 keV. The crystal has a diameter of $\varnothing = 46$ mm and is 46 mm long [Cand]. A picture of the Ge detector is presented in Fig. 3.16.

Placed in air, the detector observes x-rays and γ-rays coming from the trap center through the two Be windows described above. The detector is mounted on a movable table and thus its distance to the Be window can be adjusted. At the position closest to the Be window the geometrical acceptance of the detector is $\varepsilon^{geo} \approx 0.2\%$. Its intrinsic efficiency ε^{int} is determined with the radioactive sources ^{132}Cs, ^{133}Ba and ^{144}Eu and is displayed in Fig. A.5. These two efficiencies, $\varepsilon_{\mathrm{geo}}$ and ε^{int}, added to the transmission through the Be window result in the total detection efficiency ε^{tot}.

At 122.06 keV (^{57}Co) and 1332.5 keV (^{60}Co), the detector has a resolution of 0.93 keV and 1.8 keV, respectively. Resolutions of other energies, determined from photo peaks are listed in Table A.1. At the detector position the magnetic field is too small to have any measurable influence on the energy resolution.

3.4.3 LeGe detector

On the North side of the Penning trap the Canberra LeGe detector is mounted on a support table. Its Ge crystal is planar contacted and has an active area of 100 mm^2 ($\varnothing = 11.3$ mm) with a thickness of 10 mm [Cane]. In front of the crystal, a 0.025 mm thick Be window separates the vacuum of the detector from its surrounding. The complete detector assembly, i.e., coldfinger and Ge crystal, can be connected to the

[9] Brushwell IF-1, minimum of 99.8% Be content [Bru08b]

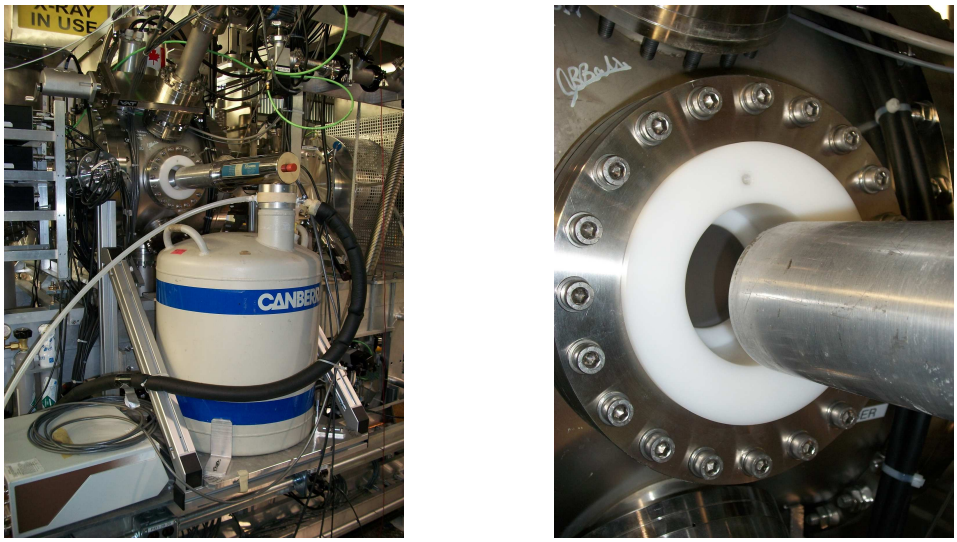

Figure 3.16: The Ge detector installed at the South side of the trap (left). The Ge detector in its retracted position (right). The white plastic cap is to protect the Be window from contact with the Ge detector.

ultra-high-vacuum chamber of the spectroscopy Penning trap via a CF2.75" flange. A gate valve is installed between the LeGe detector assembly and the trap's vacuum vessel. This allows one to separate the detector from the vacuum chamber. A CF1.33" pumping port connects to a turbo pump allowing one to evacuate the detector separately. With this setup, the LeGe can be added to or removed from the Penning trap vacuum chamber without having to break the trap's vacuum. When the LeGe detector is mounted and connected to the vacuum system, it can be moved into one of the access ports inside the magnet as close as ∼100 mm to the trap center. At this position the detector covers a solid angle of ∼ 0.08%. A picture of the LeGe detector mounted on the North side of the spectroscopy Penning trap is presented in Fig. 3.17.

A Transistor-Reset-Preamplifier (TRP) amplifies the energy signal of the Ge crystal. Its output signal constantly rises from 0 V to 5 V and gets reset every 5 s if no event occurs in the detector [Cana]. Dependent on the photon-count-rate, this reset may happen more frequently. This TRP preamp reduces pile-up effects and higher count rates can be accepted [Canb].

The resolution of the LeGe detector was determined using a ^{57}Co source as well as a ^{133}Ba source and is 208(6) eV, 579(3) eV, and 1.123(20) eV at photo peak energies of 14 keV, 122 keV, and 356 keV, respectively. Further energies are listed in Table B.2 and displayed in Fig. 3.18. Based on Eq. (3.3) the intrinsic resolution was calculated and is also plotted in Fig. 3.18. The actual resolution of the LeGe detector is very close to the

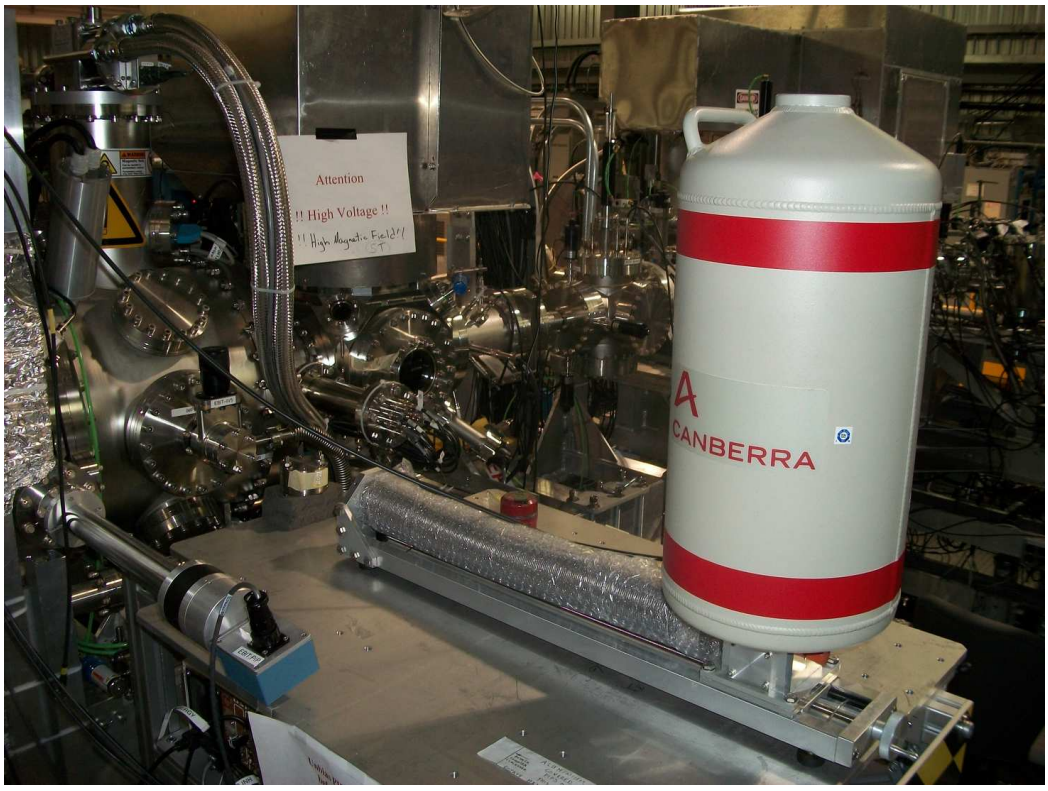

Figure 3.17: Picture of the LeGe detector prior to its installation on the North side of the EBIT.

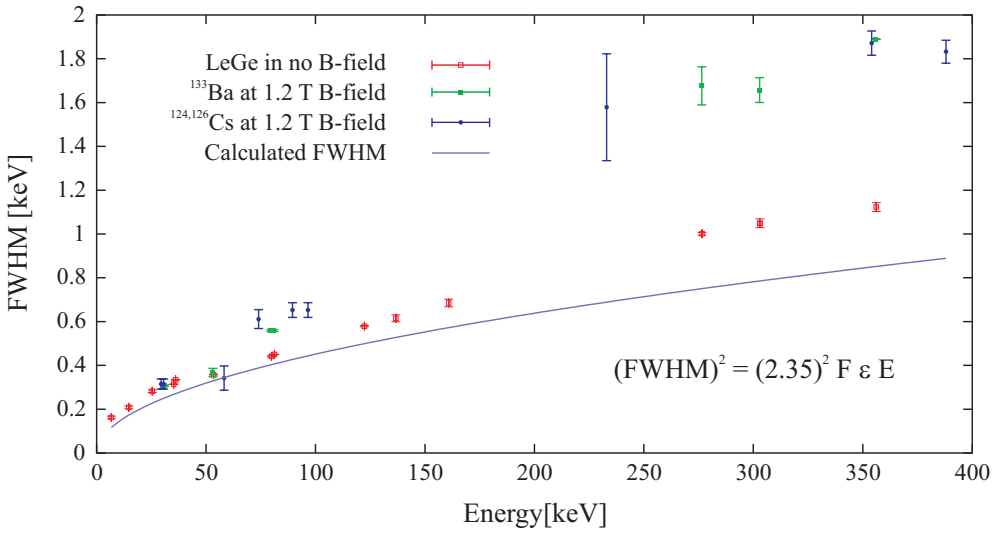

Figure 3.18: FWHM of the LeGe detector as a function of the photo peak energy. For this data a ^{133}Ba and a ^{57}Co photo peaks as well as ^{124,126}Cs photo peaks were used.

intrinsic one, i.e., other effects such as electronic noise and incomplete charge collection are less significant.

In order to determine electron capture branching ratios, the intrinsic detection efficiency needs to be know. Therefore, a photon-spectrum was taken with a ^{57}Co source and a calibrated ^{133}Ba source[10].

The ECBR of ^{124}Cs was measured with the LeGe detector. The x-ray efficiency was determined by measuring the spectrum of ^{126}Cs. This method is then independent of prior knowledge of the x-ray detection efficiency. However, the γ efficiencies need to be known. In the case of ^{124,126}Cs, ^{133}Ba was used to calibrate the efficiency between 200 keV and 400 keV.

After the ^{124,126}Cs measurement it was discovered that the DSPEC, the unit used to record the LeGe detector spectrum, does not record all energies with the same efficiency. This is illustrated in Fig. B.2 where relative efficiencies are presented for different hardware setups. For energies above $\sim$ 120 keV, the recorded data is truncated. If the LeGe detector preamp signal was terminated with 50 Ω or if the amplification of the DSPEC was reduced, the extracted efficiency agreed with Penelope2008 simulations up to $\sim$ 350 keV. At higher energies, one of the two DSPEC units, DSPEC 321, recorded data less efficient. However, below an energy of $\sim$ 120 keV, the photo peak efficiencies were equal during all tested settings and always agreed with simulations.

[10]Source LT 880, calibrated by Deutscher Kalibrierdienst, Kalibrierzeichen 012077 DKD-K-06501 03-07, July 1st, 2003

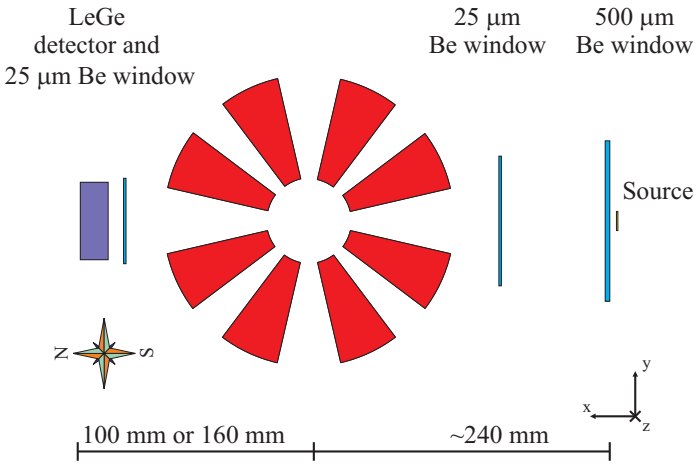

Figure 3.19: Schematic view of the setup to determine the influence of the B-field on the LeGe detector.

As already mentioned, the efficiency of the LeGe detector in the x-ray region is determined relative between ^{124}Cs and ^{126}Cs. This only requires knowledge of the relative detection efficiencies at higher energies and will be explained in detail in Chapter 5. The detection efficiency at these higher energies, namely 254.1 keV and 388.6 keV, were determined with a 133Ba source during the ^{124,126}Cs experiment with the same data acquisition setup. To account for the effect of signal truncation, an additional systematic uncertainty is added to the determined ECBR.

During operation the LeGe detector was positioned close to the trap center inside an access port of the magnet. It could be as close as ~ 100 mm to the trap center with a strong magnetic field of the Helmholtz coils present. In the closest placement of the detector to the trap center, this field was estimated to be about $(40 \pm 2.5)\%$ of the field at the trap center (see Fig. 3.2, COMSOL simulation [COM]) with its orientation perpendicular to the crystal axis. For a magnetic field of 5 T in the trap center the residual field at the position of the LeGe detector is then calculated to be about 2 T.

The magnetic field is expected to have two effects on the LeGe detector inside the vacuum. Due to the Lorentz force, the charge carrier trajectories are bent. This phenomenon is expected to change the shape of the output pulse as the charge-carrier path length increases. Additionally, one expects an enhanced Penning effect in the vacuum between the Ge crystal and detector capsule. Recently, the behavior of Ge detectors in magnetic fields has been investigated and published for magnetic fields of ≈ 1 T [Lor07], 0–0.8 T [Szy08], and up to to 2.5 T [Agn09]. The results of these studies agree with observations made within this work.

In order to investigate the influence of the magnetic field on the detector, the LeGe detector was placed at varying distances from the trap center, i.e., in different magnetic field strength regions. A radioactive source was placed at the Be window on the South side of the trap opposite the LeGe detector. Hence, γ-rays were detected by the LeGe that traversed both Be windows and the central trap electrode as illustrated in Fig 3.19. Spectra were recorded with the detector placed at a known, fixed, position and the magnetic field at the trap center either at 0 T, 4 T, or 5 T. After a spectrum was recorded at 0 T, the field was ramped up with the LeGe detector being un-biased. After the magnetic field reached its final magnitude, bias was applied to the Ge crystal. During this process no sparks or current draw could be observed. Therefore, we conclude that no enhanced Penning trap effect occurred.

The magnetic field strength was determined experimentally in the following way: ions in the trap were resonantly excited with a dipole frequency and the B-field dependent frequency was determined. This allowed one to measure the magnetic field to sufficient precision. To do so, oxygen was charge bred to O^{4+} while the dipole frequency ν_{RF} was applied to the central trap electrode segments. One phase was applied to segments one through four and the opposing phase was applied to segments five through eight. Following the dipole excitation the ions were extracted from trap. For $\nu_{RF} = \nu_c$, the the ion's cyclotron frequency, the ions were excited maximally and moved to a larger cyclotron radius. Thus they could not leave the trap during extraction. This resulted in a count rate minimum of extracted ions measured at the detector[11] (see Fig. 4.1). The measured ion intensity as a function of ν_{RF} is displayed in Fig. 3.20. The cyclotron frequency was determined to be $\nu_c = 15.307(5)$ MHz. With the known charge-to-mass ratio q/m, the magnetic field strength can be calculated to $B_{mean} = 4.043(2)$ T using the relation $\nu_c = B\,q/(2\,\pi\,m)$. The measured magnetic field agrees with the setpoint of the current control system of the magnetic field. The presented uncertainties are statistical ones only. Systematic uncertainties were not investigated but could be considered of similar order. Due to the spacial expansion of the ion cloud inside the trap, the magnetic field is probed over a wide range. Therefore, the magnetic field determined with the technique of dipole excitation corresponds to the mean magnetic field in the trap center. However, for in-trap decay spectroscopy the magnetic field strength is not required to be known precisely. The presented measurement was performed to test the magnet controller.

In ECBR measurements, x-rays with energies in the region 9 keV to 40 keV are measured. Therefore, the effect of the magnetic field on the LeGe detector was mainly investigated by determining the FWHM of the 39.5 keV and 40.1 keV $K_{\alpha_{1,2}}$ lines of a ^{142}Eu source. The data acquisition was set up such that only spectra up to an energy of $\sim$ 50 keV were recorded in order to provide a detailed shape of the photo peak. The result of the 39.5 keV and 40.1 keV peak analysis is listed in Table 3.2. Based on this analysis one concludes that magnetic fields up to about 2 T at the position of the

[11] TSYBL:MCP6

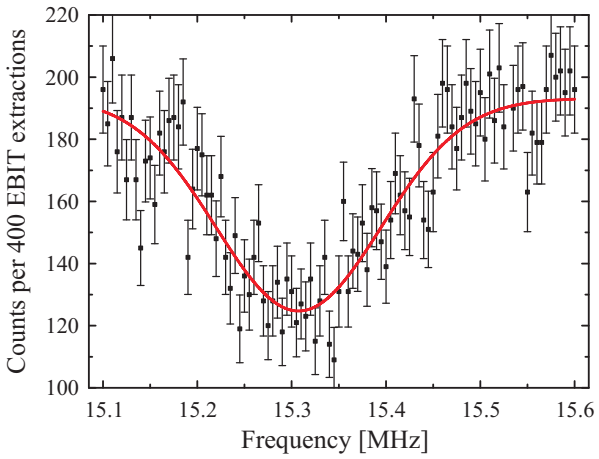

Figure 3.20: B-field determination with dipole excitation.

Trap distance	B-field trap	B-field detector	FWHM 39.5 keV and 40.1 keV	Area/ 1 hour	$\chi^2/706$
160 mm	0 T	0 T	311.9(11) eV	5368(21)	1.140
160 mm	4 T	$\sim$ 1 T	311.8(8)	5327(16)	1.235
160 mm	5 T	$\sim$ 1.2 T	312.6(30)	5365(56)	0.965
100 mm	0 T	0 T	311.6(11)	5396(21)	1.077
100 mm	4 T	$\sim$ 2 T	312.3(4)	5358(8)	1.846

Table 3.2: Influence of the B-field on the LeGe detector.

detector do not significantly influence the detection of x-rays. Peak shape and detection efficiency remain constant in the x-ray region. This agrees with results presented in [Szy08], where it was found that the degradation of the energy resolution is negligible at low energies. The only indication of an influence of the magnetic field on the LeGe detector is the increase of χ^2 by a factor of ~ 1.8. An explanation is the slight deviation of the photo peak from an ideal Gaussian pulse.

During the ECBR measurement of ^{124,126}Cs, calibration spectra were recorded throughout the measurement with the LeGe detector placed about 100 mm away from the trap center and a ^{133}Ba source at the source position displayed in Fig. 3.19. The resulting peak widths (FWHM) are listed in Table 3.3. Based on the analyzed data, one concludes that the influence of the magnetic field is more significant for the detection of higher energetic photons. This observation agrees with results presented

	31 keV	53 keV	81 keV	276 keV	356 keV
0 T	287.8(3)	346.0(19)	424.9(4)	853.2(57)	936.6(115)
$\frac{\chi^2}{\mathrm{DoF}}$	6.796	1.174	2.050	1.142	1.041
5 T	307.5(22)	367.3(175)	559.0(41)	1676.3(884)	1821.3(504)
$\frac{\chi^2}{\mathrm{DoF}}$	1.779	1.182	1.092	0.974	0.984

Table 3.3: FWHM of ^{133}Ba photo peaks for 0 T and 5 T magnetic fields.

in [Lor07, Szy08, Agn09]. For photons in the x-ray region the effect on the resolution is negligible. This is in agreement with the results presented in the previous paragraph.

For ECBR measurements, detection efficiency is important. Unfortunately, no direct comparison of the detection efficiency of the LeGe detector between no B-field and applied B-field was done above ~ 50 keV. The ^{133}Ba calibration spectra recorded during the ^{124,126}Cs experiment were analyzed. The peak areas were then divided by the peak areas obtained from a calibration spectrum recorded prior to the beam time and the results are presented in Table 3.4. Based on these values, the detection efficiency appears to be affected by the magnetic field. However, in this comparison the set up of the source was completely different. The spectrum without a magnetic field was recorded with the detector outside the vacuum vessel and the source directly in front of it. The spectrum with the detector inside the magnetic field was recorded with the setup illustrated in Fig. 3.19 and the peak areas corrected for the attenuation of 525 µm Be calculated based on [NND10]. Contrary to the results presented here, [Szy08] found no appreciable change in the intrinsic detection efficiency of a Ge detector in a 0.8 T field whereas [Agn09] reports an energy dependent change of the detection efficiency. Depending on the photon energy and the magnetic field applied, the efficiency loss ranges from $\sim -4\%$ to $\sim 1\%$ for 59.4 keV, and from $\sim 3.5\%$ to $\sim 7.2\%$ for 1332.5 keV.

It is thus possible that the source in this study was placed such that little, but some, material besides the Be windows was covering the source. This would result in stronger attenuation for x-rays and less attenuation for γ rays and could explain the discrepancies arising in Table 3.4.

In future measurements, this effect has to be investigated further if solid state detectors are placed in very high magnetic fields close to the trap. For fields below ~ 0.8 T and photon energies below ~ 400 keV these effects are very small and have no influence on the detection efficiency [Szy08].

	53 keV	81 keV	276 keV	303 keV	356 keV
$\frac{A(4\,\mathrm{T})}{A(0\,\mathrm{T})}$	0.0137(6)	0.0161(1)	0.0389(21)	0.0866(34)	0.2712(101)

Table 3.4: Fraction of peak areas with 0 T and 5 T magnetic field inside the Penning trap.

3.5 Data acquisition system

Generally, x-ray and γ-ray spectra were recorded with an Ortec DSPEC unit. In parallel, efforts were taken to implement a data acquisition system based on the sampling ADC tig10 [Mar08] developed by the University of Montréal. However, the required performance of tig10 system in combination with the LeGe detector could not be achieved [Bru09]. Therefore, the tig10 system was used during the Cs-experiment to only record β events on the PIPS-600 detector in coincidence with γ-rays from the Ge detector. The LeGe detector was read out with the DSPEC during all measurements.

For the analysis of x-ray spectra taken during the ^{107}In measurement and calibration spectra recorded prior to this experiment, a peak-function was defined according to [Hel80, Haa06] and used to fit the photo peaks in the employed analysis software Origin [Ori]. Besides Origin, RadWare [Rad, Rad95] was used to analyze calibration spectra that were taken during systematic investigations. The advantage of RadWare is the interactive graphical user interface. This allows one to efficiently analyze calibration spectra. However, for the analysis of peaks with low statistics RadWare reached its limitation. For the analysis of x-ray spectra with low statistics an additional program was used [Sju09] that has been specifically developed by A. García and S. K. L. Sjue to determine the ECBR of ^{100}Tc [Gar93, Sju08b]. It uses the maximum-likelihood method to determine peak-area. Additionally, the program TV [The] that was developed by the nuclear structure group at the university of Cologne, Cologne, Germany, was used to analyze some spectra, generally in determining the intensity of photo-peaks by event-counting instead of fitting.

Chapter 4

Systematic Tests of the TITAN-EC Setup

For in-trap decay spectroscopy experiments at TITAN, beam transport, ion transmission through the RFQ, and ion injection and storage in the Penning trap need to be optimized. The ion delivery and transport optimization up to the Faraday cup (FC) in front of TITAN's RFQ (ILE2T:FC3 in Fig. 4.1) are provided by ISAC operations. From this FC onwards, beam line optics and involved ion traps have been optimized within this work to achieve the best performance during ECBR measurements. Most of these systematic studies were performed with an off-line surface ion source[1]. This ion source consists of an alkali substrate on a filament. By heating the filament, positive singly charged alkali ions are evaporated and ionized due to their low ionization potential. Depending on source type and temperature, the alkali isotope ratio emitted by the source changes. A Cs ion source delivering stable ^{133}Cs was typically used during the systematic studies for ECBR measurements.

Stable ^{133}Cs was injected into the RFQ while RF frequency f_{RF}, RF peak-to-peak amplitude V_{PP}, cooling time and gas pressure were optimized as described in Section 4.1. Afterwards, ion bunches were sent to the spectroscopy trap while beam transport and injection into the trap were optimized as described in Section 4.2. Following this optimization, ions were captured in the Penning trap. Storage times were investigated depending on the injected isotope and magnetic field strength of the Penning trap. Such studies have shown that for storage times of up to 250 ms, ion losses of less than 20 % occur. These studies are presented in Section 4.3.

All these measurements were performed using several Faraday cups and MCPs for ion detection installed along the TITAN beam line. Faraday cups are commonly used to determine beam intensities of DC beams. They were used to determine transmission efficiencies through the RFQ. With a Faraday cup, ion currents can be observed down to $\sim 1\,\mathrm{pA}$ corresponding to $\sim 6 \cdot 10^6$ singly-charged ions per second. The sensitivity is limited by electrical noise of the amplifier. Ion bunches were sent to MCPs along the beam line to determine ion-bunch intensities and ion flight times. For systematic studies, they were used in single-ion detection mode, i.e., only up to ∼10 ions per

[1] HeatWave Labs *www.cathode.com*, source ⌀ 0.250 inch

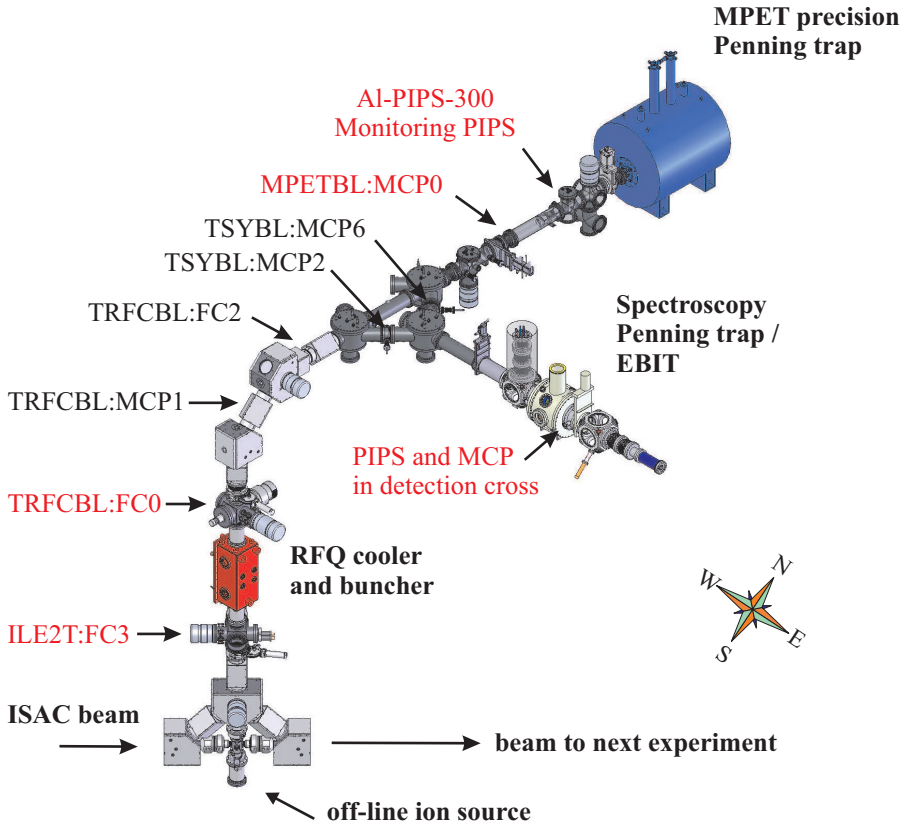

Figure 4.1: Schematic view of the TITAN experiment illustrating all ion beam diagnostic devices. The devices used during the systematic studies presented in this work are highlighted in red color.

bunch were extracted onto the MCP to avoid saturation. Higher count rates saturate the detection system and were thus only used for qualitative optimization.

In Fig. 4.1, the positions of all permanently installed beam diagnostic elements are shown. Monitoring PIPS assembly Al-PIPS-300 [Bru08a] and detection chamber including MCP (see Section 3.1.5) have been specifically developed and installed for ion-detection.

4.1 RFQ operation and optimization

Optimization of the RFQ consisted of several steps. Firstly, the RFQ was optimized in DC transmission, i.e., with RF fields and buffer gas applied but without the confining

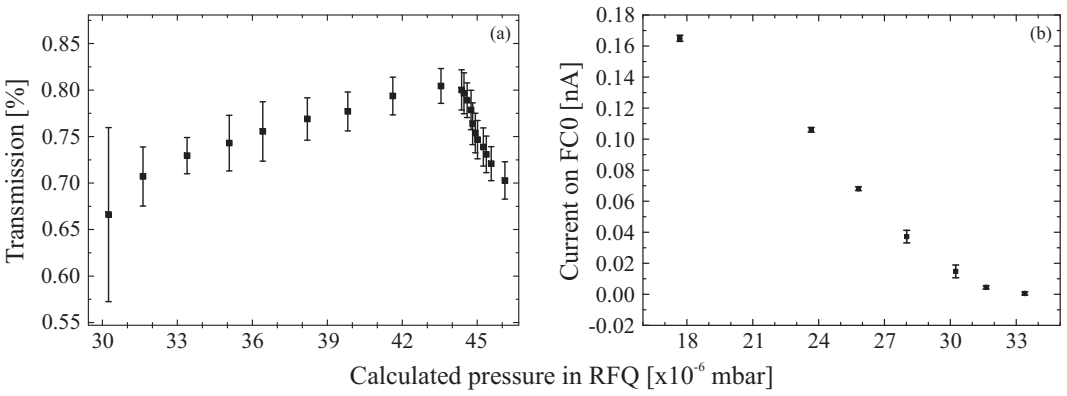

Figure 4.2: Influence of He buffer gas on the DC transmission. (a) DC transmission through the RFQ for different flow rates and (b) transmission through the RFQ with a longitudinal trapping potential applied. For explanation see text.

longitudinal potential well[2] displayed in Fig. 2.8. In this operation mode the beam line elements upstream of the RFQ are tuned onto FC0 to achieve the maximum transmission. The transmission efficiency in DC operation is calculated from the ratio of the current on Faraday cups FC3 and FC0 before and after the RFQ. This transmission primarily depends on injected ion energy, RF amplitude, and RF frequency, but also on the chemical properties of the element injected and its mass difference to the buffer gas. Depending on these properties, the likelihood of charge exchange reactions with impurities in the He buffer gas and ions scattering out of the trap changes. For the alkali ion $^{133}Cs^{1+}$ from TITAN's ion source, the transmission is as high as $80 \pm 5\%$ for a He buffer-gas flow rate of 7 sccm$\approx 43 \cdot 10^{-6}$ mbar. Fig. 4.2 displays the DC transmission through the RFQ for different gas flow rates. For low gas flow rates, the incoming ions are not completely stopped by the buffer gas inside the RFQ (see next paragraph). Instead, they pass through the RFQ but still reach FC0. This is reflected by the large error bars for small flow rates.

After RFQ-optimization in DC mode the minimal buffer-gas flow rate is determined. Therefore, the RFQ is operated in trapping mode, i.e., with a longitudinal trapping potential created by applying a capture potential as displayed by the solid, black line in Fig. 2.8. This potential is kept static without extracting the ions. For low gas flow rates the ions do not lose enough energy through collisions with the buffer gas inside the RFQ and pass through the device. In Fig. 4.2 this behavior is displayed for different calculated gas pressures inside the RFQ. The pressure was estimated based on the vacuum pressure outside the RFQ, considering the flow through the 5 mm diameter pumping diaphragm and a pumping speed of 500 l/s for the used turbo pump.

[2]RFQ electrode 24 is biased with -7 V instead of 5 V.

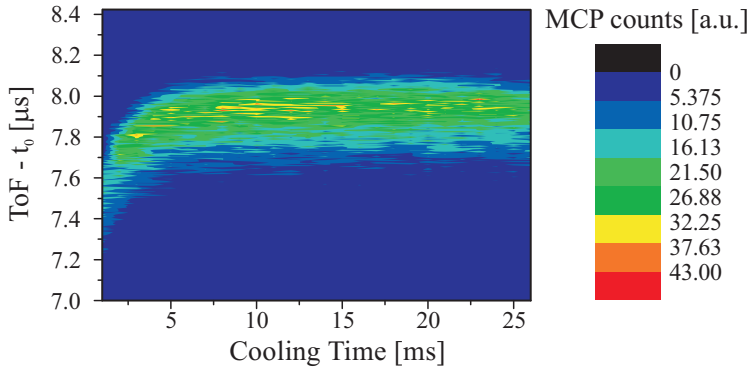

Figure 4.3: Ion time-of-flight distribution recorded on MCP0 as a function of cooling time. Typically, each extracted ion pulse consists of approximately 5 ions in order to not saturate the MCP and operate well below the space-charge limit of the RFQ. Each ToF distribution is the sum of 100 extraction cycles with a He gas-flow of 5 sccm.

The fact that ions are not completely stopped inside the RFQ for low gas pressures was found during systematic studies with the RFQ after the ^{107}In and ^{124,126}Cs ECBR measurements. For these experiments the RFQ was operated at a flow rate of 5 sccm. During the measurement of ^{126}Cs a so-called hot spot, an area of accumulated activity, was located at the position of FC0 with up to 700 µSv/hr detected at the outside of the vacuum vessel. Typical values during this experiment were 0.5 µSv/hr along the beam line and $1-2$ µSv/hr at the 45° bends. This high dose at FC0 can be explained by ions passing through the RFQ due to a too low gas flow rate. In future experiments at TITAN this has to be taken into consideration.

For further systematic investigations, the RFQ is set up for its intended operation to cool and bunch injected ions. In order to determine the ideal cooling time inside the RFQ, a beam gate is installed in front allowing only a certain number of ions to enter the RFQ. Depending on the beam intensity, this gate was typically open for 10 µs up to 2 ms. After a certain cooling time the ions are then extracted onto MCP0 and their intensity and distribution are recorded with a Stanford Research SR430 multi-channel scaler (MCS). The ion distribution is displayed in Fig. 4.3. This measurement was performed in single-ion counting mode with typically 4-6 ions per bunch. Under these conditions, the RFQ is also operated well below its space-charge limit with a gas flow rate of 5 sccm$\approx 36 \cdot 10^{-6}$ mbar. At the time of the measurement it was not known that this flow rate is insufficient to stop all ions with the applied conditions. However, it does not affect the measurement of the ion distribution because those ions that are not stopped inside the RFQ cannot reach MCP0. When ions leave the RFQ, they are accelerated by the RFQ bias and cannot pass the two 45° benders along the beam line. After $\sim$ 7 ms the ions are cooled down as their time-of-flight distribution does no longer

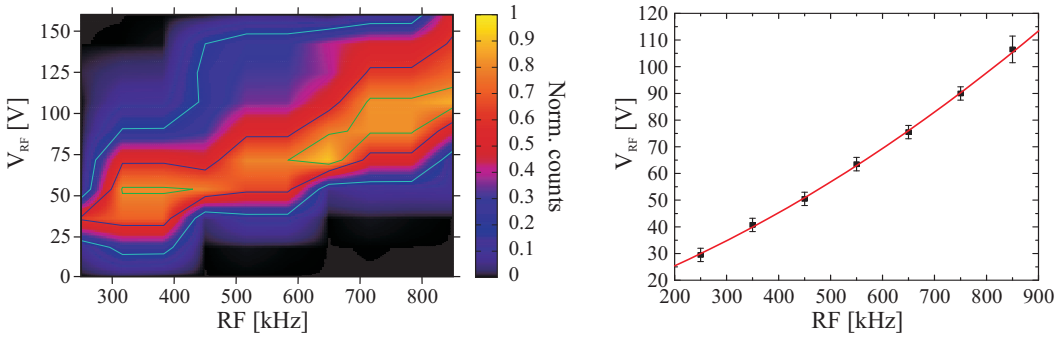

Figure 4.4: Ion intensity extracted from the RFQ as a function of RF frequency and voltage (left). Maximal transmission through the RFQ plotted as a function of RF frequency (right).

change in time as illustrated in Fig. 4.3. Additionally, it is pointed out that for cooling times up to $\sim 25\,\mathrm{ms}$ no significant intensity loss was observed.

The transmission of an ion through the RFQ depends on whether an ion moves on a stable or unstable trajectory inside the RFQ. This can be understood from the stability parameter q that is defined in Eq. (2.1). For a given RFQ electrode distance $2 \cdot r_0 = 2 \cdot 10\,\mathrm{mm}$ and a certain ion mass m, this parameter only depends on the RF frequency f_{RF} and RF amplitude V_{RF}. In order to optimize the transmission through the RFQ those two parameters were varied while the number of extracted ions was recorded on MCP0 with the MCS. During this measurement the flow rate was kept constant at 5 sccm and the beam gate applied. A cooling time of 10 ms was set while the measurement was performed in single-ion counting mode. The resulting intensity scan is displayed on the left side of Fig. 4.4. Generally, we find that higher RF frequencies are preferable because high transmission is given for a broader range of RF amplitudes. For low RF frequencies, the transmission is high only over a small range of RF amplitudes. The maximal transmission from the left plot of Fig. 4.4 was extracted and fitted with a polynomial function of second order. The resulting fit is $V_{\mathrm{RF}} = 9.5(85)\,[\mathrm{V}] + 6.8(35) \cdot 10^{-5}\,[\mathrm{V/kHz}]\,\nu_{\mathrm{RF}} + 5.2(34) \cdot 10^{-11}\,[\mathrm{V^2/kHz^2}]\,\nu_R^2$ and is displayed on the right side of Fig. 4.4. This fit can be used to extrapolate the correct RF amplitude for different masses at a given frequency.

4.2 Injection into the spectroscopy Penning trap

The efficiency of ion capture and ion storage strongly depends on injection into the trap and is referred to as acceptance phase space. Hence, the injection into the spectroscopy Penning trap is optimized by sending ions through the trap onto the MCP in the de-

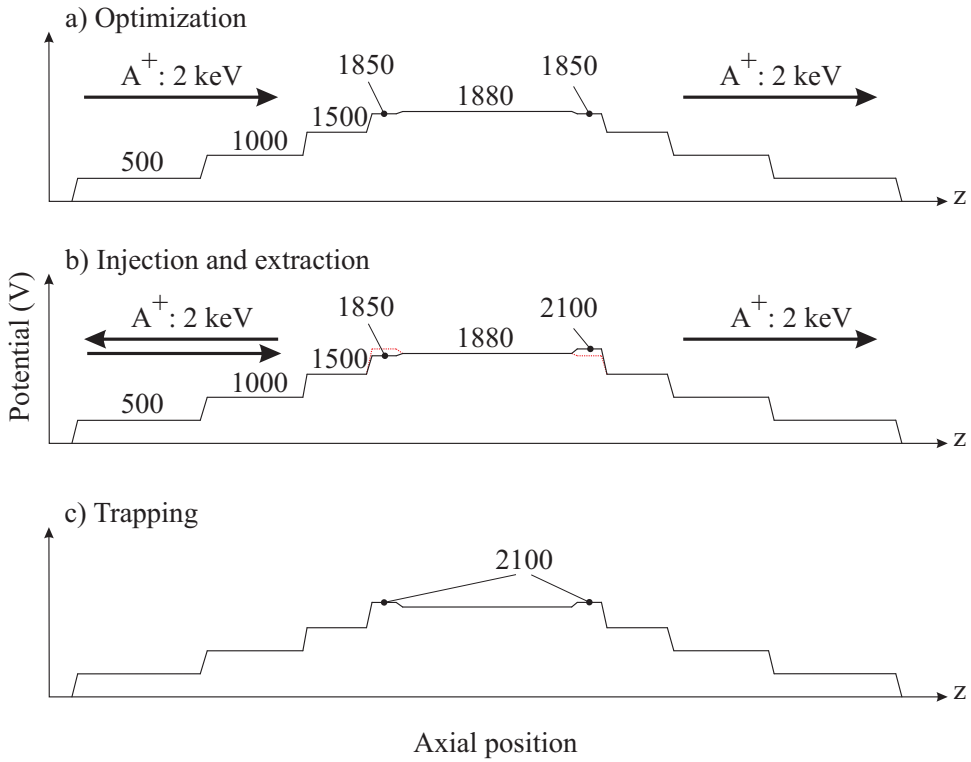

Figure 4.5: Potential landscape applied to the spectroscopy Penning trap during (a) optimization, (b) injection and extraction, and (c) trapping of an ion bunch with 2 keV kinetic energy.

tection chamber. This process does not involve any capturing and the typical potential applied to the drift tubes is displayed in Fig. 4.5a. This optimization process follows the principle that all ions that can be guided through the magnetic field and trap electrode structure can and will be trapped once the appropriate electrostatic potentials are applied. It has been demonstrated that one of the highest losses comes from the ions being reflected in the magnetic fringe field, and hence an optimized transmission is critical. When the ions hit the MCP 'behind' the trap, the beam shape is visualized by a phosphor screen and then recorded with a CCD-camera installed on the view-port indicated in Fig. 3.6. If the ions are injected on the magnetic field axis, a spot is visible on the phosphor screen. This spot is displayed on the left in Fig. 4.6 where the ion image on the phosphor screen in a bright dot. Ions injected off-axis start to gyrate when they enter the magnetic field of the Penning trap and the resulting shape is that of a ring displayed on the right in Fig. 4.6. This behavior has been verified in SIMION simulations [Lap09].

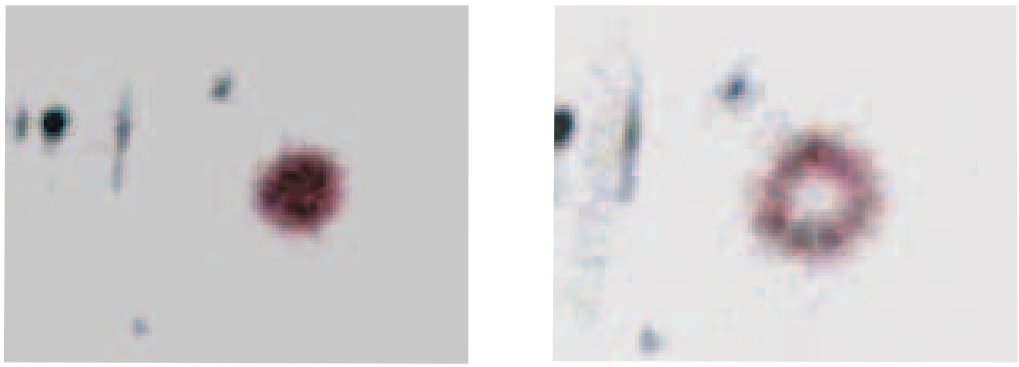

Figure 4.6: Beam profile on the MCP in the detection chamber (see Section 3.1.5) of ions passing through the Penning trap. Displayed are pictures taken with a CCD-camera and ions injected on axis (left) as well as ions injected off-axis (right).

After optimizing the injection into the magnetic field, the capture timing cycle is set up. The timing is done by a programmable pulse generator that controls fast switching high-voltage switches. The timing cycle is set up in such a way that the end cap towards the RFQ is at a low potential while the end cap towards the detection chamber is at a high potential. The applied potential is displayed in Fig. 4.5(b) by a black line. As soon as the ion bunch is in the trap's center, the entrance end cap is switched to a high potential. This captures the ion bunch in the Penning trap with the potential landscape sketched in Fig. 4.5(c). After a short storage time of 1-5 ms, the ion bunch is extracted onto the MCP in the detection chamber by applying the potential indicated by the red line in Fig. 4.5(b). The number of counts at the MCP as well as the shape are then used to optimize the beam line ion optic elements (see Fig. F.2) to maximize the capture and storage efficiency.

4.3 Systematic storage time investigations

For ECBR measurements it is necessary to determine the optimal storage time that balances ion losses in the trap with high decay count-rates. A method was developed to determine the loss rate of the Penning trap as a function of storage time, using TITAN's off-line surface ion source for measurements. A controlled and reproducible number of ions was injected into the RFQ using a beam gate. The intensity of the beam injected into the RFQ was set such that 2-6 ions were detected on the MCP in the detection chamber. First, 100 identical bunches of ions from the RFQ were injected into the trap, stored for $t_{\mathrm{storage}} = 5\,\mathrm{ms}$, and extracted onto the MCP in the detection chamber. The average ion-bunch intensity is referred to as $\overline{N}_{\mathrm{norm}} = N_{\mathrm{norm}}/100$. A storage time of 5 ms is chosen as reference because little losses are expected to occur during this time.

Shorter storage time were suffered from hardware limitations. Afterwards, the storage time t_{storage} was changed and one ion bunch was stored for that time period before it was extracted onto the MCP. The recorded number of ions N_{storage} was normalized by $\overline{N}_{\text{norm}}$. This procedure was repeated n times and resulted in a storage efficiency

$$\varepsilon_{\text{storage}} = \frac{1}{n} \sum_{i=1}^{n} \frac{N_{\text{storage}}}{\overline{N}_{\text{norm}}} \,. \tag{4.1}$$

This procedure suffers only minimally from ion intensity fluctuations that naturally occur over time due to temperature changes. The 100 repetitions used to determine $\overline{N}_{\text{norm}}$ and the one shot for N_{storage} happen in short time succession. Therefore, ion intensity fluctuations are only statistic based and on a short time scale negligible. A LabVIEW hard-ware control program [Ins] was created to automate this measurement. Several storage time scans were performed that found inconsistencies stemming from the timing generator. After these issues were resolved, two scans were performed with $^{39}\text{K}^{+}$ and $^{133}\text{Cs}^{+}$ at 4 T and 5 T, respectively.

Storage of $^{39}\text{K}^{+}$

In order to determine the intrinsic storage time of the Penning trap, $^{39}\text{K}^{+}$ was injected into it. The measured, normalized storage efficiency is summarized in a plot displayed in Fig. 4.7. As a consistency check, a measurement was performed for a storage time of 5 ms resulting in 99.6(69)% storage efficiency as expected. For a storage time of 25 ms, 95.4(75)% of the ions are lost compared to the 5 ms storage time. The efficiency slowly decreases for storage times longer than 5 ms and at 1 s storage time, 72.7(84)% of the ions remain stored compared to $t_{\text{storage}} = 5$ ms. For even longer storage times, the efficiency continuously drops to about 20% for 10 s storage time. All measurements were performed with a magnetic field of 4 T.

Storage of $^{133}\text{Cs}^{+}$

Prior to the ECBR measurement of ^{124,126}Cs, the magnetic field was ramped first to 4.5 T and then 5 T. This required substantial re-tuning of the ion optical elements in the transfer beam line as described in Section 4.2. Additionally, tuning the beam into the trap became necessary. Once a tune was established, the storage time measurement as described above was repeated using $^{133}\text{Cs}^{+}$. The consistency check at 5 ms resulted in a storage efficiency of 99.5(34)%. For increasing storage times the storage efficiency dropped significantly. After 20 ms only 71.4(28)% of the ions were still confined compared to 5 ms storage. The efficiency further dropped to 22.2(16)% for a storage time of 100 ms. Measured efficiencies for storage times above 250 ms show an increasing trend as displayed in Fig. 4.8. A possible explanation are stability fluctua-

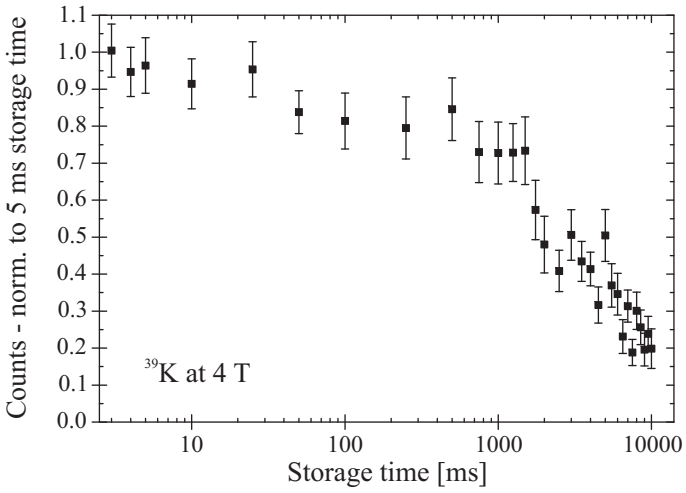

Figure 4.7: Intensity of extracted ^{39}K ions as a function of the storage time. The counts were normalized to a storage time of 5 ms.

tions of ion optical power supplies and the trap's drift tube power supplies. We also noticed, that at a magnetic field of 5 T, the beam tune became extremely sensitive to small changes in beam line optics. A tune might be sufficient to store ions for 5 ms but not ideal to store ions for long time periods. Slight changes in the tune could have a greater effect on the storage efficiency for long storage times than short ones. Automated scans were performed over a period of several hours. During this time the beam tune might have shifted leading to a better tune into the trap and thus resulting in higher storage efficiencies. The measurement was performed in June 2009 with high day–night temperature fluctuations. A temperature dependent influence on ion storage and beam line optics has also been observed during systematic studies with the mass-measurement Penning trap [Bro10b, Ett10a].

Summarizing the results of the storage time measurements, one concludes that ions can successfully be stored for a sufficient amount of time in the spectroscopy Penning trap to perform ECBR measurements. In this work, ^{107}In was stored for 1 s while ^{124,126}Cs were stored for 25 ms and 50 ms. For lower magnetic fields it is easier to inject ions into the trap. Nevertheless, during ECBR measurements, up to 10^6 ions are simultaneously stored inside the trap while a maximum of 10 ions were stored at a time during the measurements presented here.

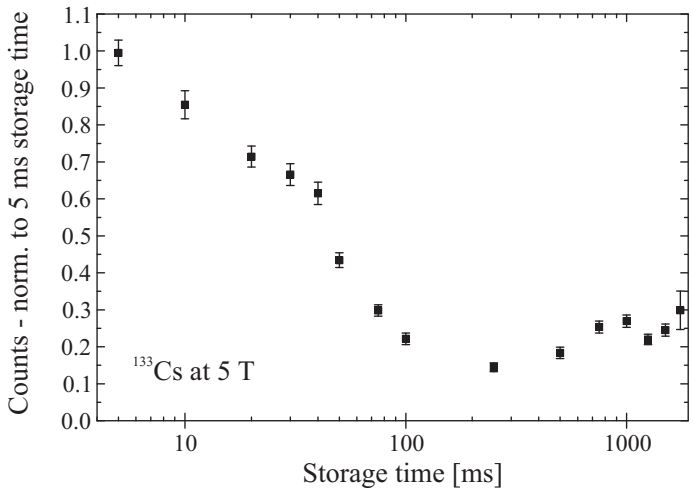

Figure 4.8: Intensity of extracted ^{133}Cs ions as a function of the storage time. The counts were normalized to a storage time of 5 ms.

Chapter 5

First Electron-Capture In-Trap Decay Spectroscopy

The measurement of electron-capture branching ratios (ECBR) of intermediate transition nuclei in double-beta decays provides important nuclear structure information to benchmark theoretical models of $2\nu\beta\beta$ decays as described in Chapter 1. At TITAN, the technique described in Section 1.5 has been developed with the aim of measuring these ECBRs.

During two online measurement campaigns with radioactive ^{107}In and ^{124,126}Cs, the feasibility and advantages of this technique were demonstrated. It was the first time that an electron-capture decay had been measured in a Penning trap [Ett09, Bru10b]. The isotopes ^{107}In and ^{124,126}Cs were chosen due to their rather strong ECBRs of 64(3)%, 10(9)%, and 19.1(23)%, respectively [NND10]. The results of the ^{107}In measurements are presented in Section 5.2 while the ^{124,126}Cs measurement is described in Sections 5.3 and 5.4. For the ECBR measurement of ^{107}In the magnetic field was at 4 T and ions were stored for 1 s, while ^{124,126}Cs was measured at 5 T with storage times of 25 ms and 50 ms.

In an ECBR measurement of double-beta decay transition nuclei, the ratio between electron capture and β^- decay is determined. This is illustrated in the left decay scheme of Fig. 5.1. The measurements performed within this work test the feasibility of the developed method and determine the electron-capture branching ratio versus the β^+ decay branch as illustrated in the right decay scheme of Fig. 5.1.

5.1 Electron-capture branching-ratio measurement at TITAN

The ECBR is defined as the fraction of electron captures N_{EC} to the total number of decays N_{total},

$$BR\,(EC) = \frac{N_{EC}}{N_{total}}\,. \tag{5.1}$$

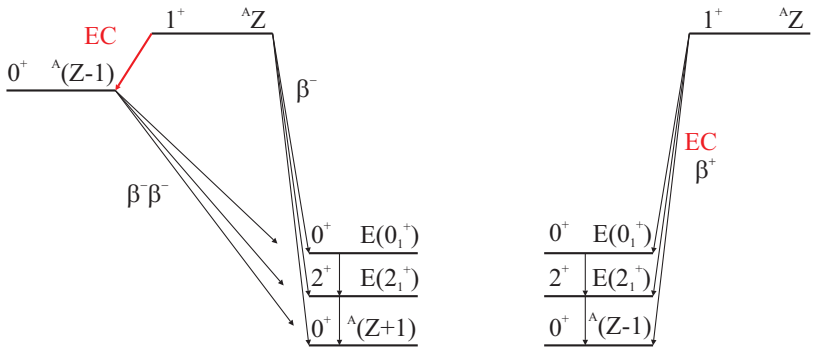

Figure 5.1: Electron-capture decay schemes of (left) $\beta\beta$ transition nuclei and (right) conventional EC isotopes.

These two quantities must be determined experimentally. The most common method for short lived isotopes is decay spectroscopy. In this case, N_{EC} is determined by observing x-rays following the electron capture. N_{total} is determined by measuring the sum of all decay branches that occur by employing a system with a well determined detection efficiency.

If the intensity I^A of at least one branching ratio $BR(A)$ of the decay-branch A is known precisely from another experiment, the total number of decays N_{total} can be deduced from the number of measured decays D^A_{meas} of that particular branch A. Knowing the intrinsic energy-dependent detection efficiency $\varepsilon^{int}_{det}(E_A)$, and the geometrical detection efficiency ε^{geo}_{det} the total number of decays is given by

$$N_{total} = \frac{D^A_{meas}}{\varepsilon^{int}_{det}(E_A)\,\varepsilon^{geo}_{det}\,I^A}\,. \tag{5.2}$$

In order to determine N_{total} of $\beta\beta$ decay transition nuclei, the emitted β particles can be detected. In the TITAN-EC setup ε^{geo}_{det} is difficult to determine because of the magnetic bottle produced by the quasi-Helmholtz coil pair (see Section 3.1.2) and the uncertainty of the ion-cloud distribution inside the trap. Furthermore, it is not granted that it stays constant throughout the experiment. A more elegant way of determining N_{total} is by measuring the photons emitted in the decays of excited states in decay products. Generally, nuclei decaying by beta decays feed excited states of the daughter nuclei. These excited states emit a photon while decaying to lower-lying states. Based on the known strengths of these branches, N_{total} can be derived by measuring the number of events $D^{\gamma}_{meas}(E)$ of the photo peak at the energy E, if $\varepsilon^{int}_{det}(E)$ is known. If x-rays and γ rays are detected simultaneously with the same detector, the measurement becomes independent of ε^{geo}_{det}.

N_{EC} is determined by measuring the K-shell x-rays D^K_{meas} of the daughter isotope. However, EC decay is not the only process creating a vacancy in the atomic shell. Conversion electrons (CE) also create vacancies in the atomic shell that result in the emission of an x-ray when they are filled. Therefore, D^K_{meas} is the sum of EC and CE events,

$$D^K_{meas} = N_{total}\, \varepsilon^{int}_{det}(E_\mathrm{K})\, \varepsilon^{geo}_{det} \left(BR(EC) \cdot \omega_\mathrm{k} \cdot f_\mathrm{k} + \omega_\mathrm{k}\, I^{CE}_\mathrm{K} \right) , \tag{5.3}$$

with I^{CE}_K being the total intensity of K-shell conversion electrons, ω_k being the fluorescence yield, i.e., the probability that the vacancy in the K-shell is closed while emitting an x-ray, and f_k the probability that an EC leaves a vacancy in the K-shell. The ECBR can then be expressed as

$$BR\,(EC) = \frac{1}{\omega_\mathrm{k} \cdot f_\mathrm{k}} \left(\frac{\varepsilon^{int}_{det}(E_A)\, I^A\, D^K_{meas}}{\varepsilon^{int}_{det}(E_\mathrm{K})\, D^A_{meas}} - \omega_\mathrm{k}\, I^{CE}_\mathrm{K} \right) . \tag{5.4}$$

This branching ratio is independent of the geometrical detection efficiency if x-rays and γ rays are detected with the same detector. The latter equation simplifies to

$$BR(EC) = \frac{I^K - I^{CE}}{\omega_\mathrm{k} \cdot f_\mathrm{k}} , \tag{5.5}$$

using the total K-shell intensity

$$I^K = \frac{D^K_{meas}\, I^A\, \varepsilon^{int}_{det}(E_A)}{D^A_{meas}\, \varepsilon^{int}_{det}(E_\mathrm{K})} , \tag{5.6}$$

and subtracting the K-shell x-ray intensity due to conversion electrons $I^{CE} = \omega_\mathrm{k}\, I^{CE}_\mathrm{K}$.

Based on Eq. (5.4), the ECBR of ^{107}In was determined at TITAN. During this measurement the K-shell x-rays were measured as well as the 205 keV photon intensity of the excited $7/2^+$ state in ^{107}Cd. However, applying Eq. (5.4) requires detailed knowledge of the intrinsic detector efficiency. Determining $\varepsilon^{int}_{det}(E_\mathrm{K})$ with radioactive sources introduces additional uncertainties, especially in the x-ray region, due to unknown photon attenuation in the source. The detector efficiency calibration in the x-ray energy region becomes obsolete if another isotope with the same Z and a well known x-ray intensity

$$I^{K'} = \frac{D^{K'}_{meas}\, I^{A'}\, \varepsilon^{int}_{det}(E_{A'})}{D^{A'}_{meas}\, \varepsilon^{int}_{det}(E_{\mathrm{K}'})} \tag{5.7}$$

is measured with the same experimental setup. Then, Eq. (5.6) can be written as

$$\begin{aligned} I^K &= I^{K'} \frac{D^K_{meas}\, I^A\, \varepsilon^{int}_{det}(E_A)\, D^{A'}_{meas}\, \varepsilon^{int}_{det}(E_{\mathrm{K'}})}{D^A_{meas}\, \varepsilon^{int}_{det}(E_{\mathrm{K}})\, D^{K'}_{meas}\, I^{A'}\, \varepsilon^{int}_{det}(E_{A'})} \\ &= I^{K'} \frac{D^K_{meas}\, I^A\, \varepsilon^{int}_{det}(E_A)\, D^{A'}_{meas}}{D^A_{meas}\, D^{K'}_{meas}\, I^{A'}\, \varepsilon^{int}_{det}(E_{A'})}\,, \end{aligned} \tag{5.8}$$

if the x-ray energies are equal as they are for isotopes. It is noted that the isotope dependent x-ray energy shift is negligible compared to the energy resolution of the detector. Therefore, only the ratio $\varepsilon^{int}_{det}(E_A)/\varepsilon^{int}_{det}(E_{A'})$ needs to be known. Typically, E_A and $E_{A'}$ are in the region above $\sim 120\,\mathrm{keV}$. In this region the efficiency of solid state detectors is well understood and self shielding of the source is less critical. The ECBR of ^{124}Cs was determined by applying this method. Therefore, ^{126}Cs was used as calibration isotope A'.

In all experiments, the photo peak intensities D_{meas} were determined using the Ge and LeGe detector described in Section 3.4. During the ^{107}In measurement, the signal of these detectors was digitized by two DSPEC units. Schemes of the DAQ setup used during this experiment are illustrated in Fig. A.2 and Fig. B.1 for Ge and LeGe detectors, respectively.

During the ^{124,126}Cs measurement the signal of the LeGe was split and fed to the two DSPEC units. The signal of the Ge detector and the PIPS detector was sampled and recorded by the tig10. The schemes of these setups are displayed in Fig. B.3 for the LeGe detector, and Fig. C.2 and Fig. A.3 for PIPS and Ge detector signal processing, respectively. The DAQ with the split signal is explained in more detail in Section 5.4.1.

5.2 Electron-capture branching-ratio measurement of ^{107}In

For the ECBR measurement of ^{107}In, a high power Ta target was bombarded with a 65 µA proton beam from TRIUMF's cyclotron at an energy of 500 MeV. A radioactive ion beam was extracted from the ion source with a beam energy of 15 keV. Prior to delivery to TITAN, the yield was determined to be $4.9 \cdot 10^5$ ions/s and $1.6 \cdot 10^3$ ions/s of ^{107g}In and ^{107m}In, respectively, and the contamination of the beam was measured to be less than 10% at ISAC's yield station [ISA08]. The beam was delivered to TITAN's RFQ where it was cooled, bunched and sent to the spectroscopy trap. The ion bunches were first implanted into the Al foil in front of the PIPS detector installed in the detection chamber without being stored. ^{107}In isotopes were confirmed as the main component of the delivered beam by measuring the β-rate resulting in a measured half life of 33.3 ± 1.3 min. This value is in agreement with the literature value [NND10].

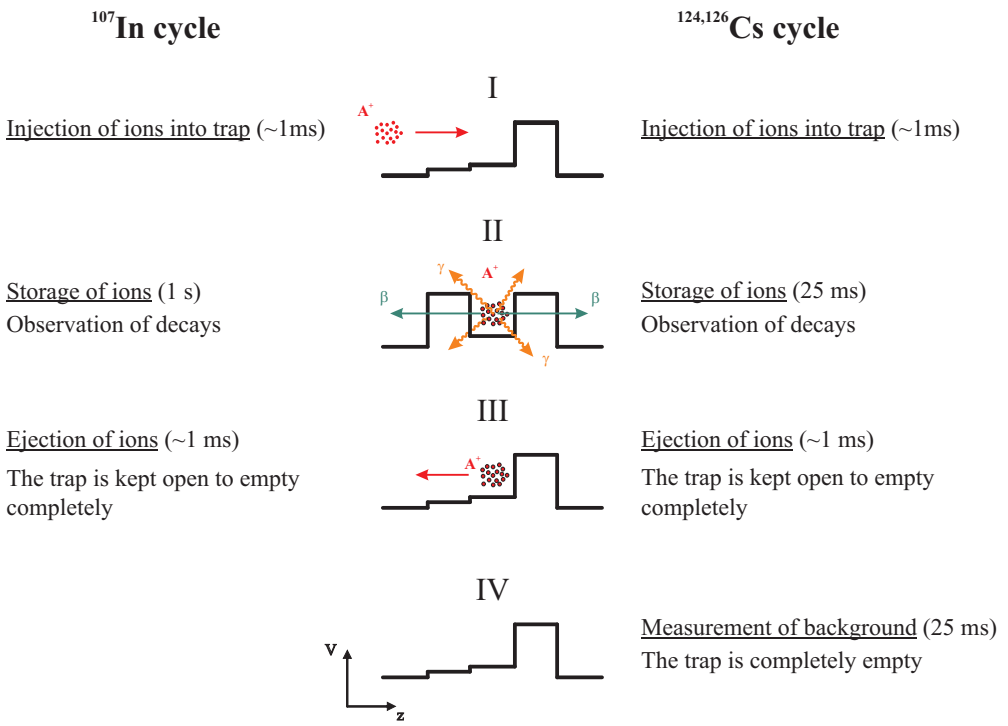

Figure 5.2: Schematic of the (left) ^{107}In and (right) ^{124,126}Cs measurement cycles. (I) Ions were injected into the trap and (II) while they were stored, their radioactive decay was observed. (III) Afterwards, the trap was emptied. During the ^{107}In measurement a new cycle started after the ejection. In the ^{124,126}Cs measurement, (IV) a background spectrum was recorded after the trap was emptied. Following this measurement a new cycle started with ion injection. Sketched is the potential V along the trap axis z.

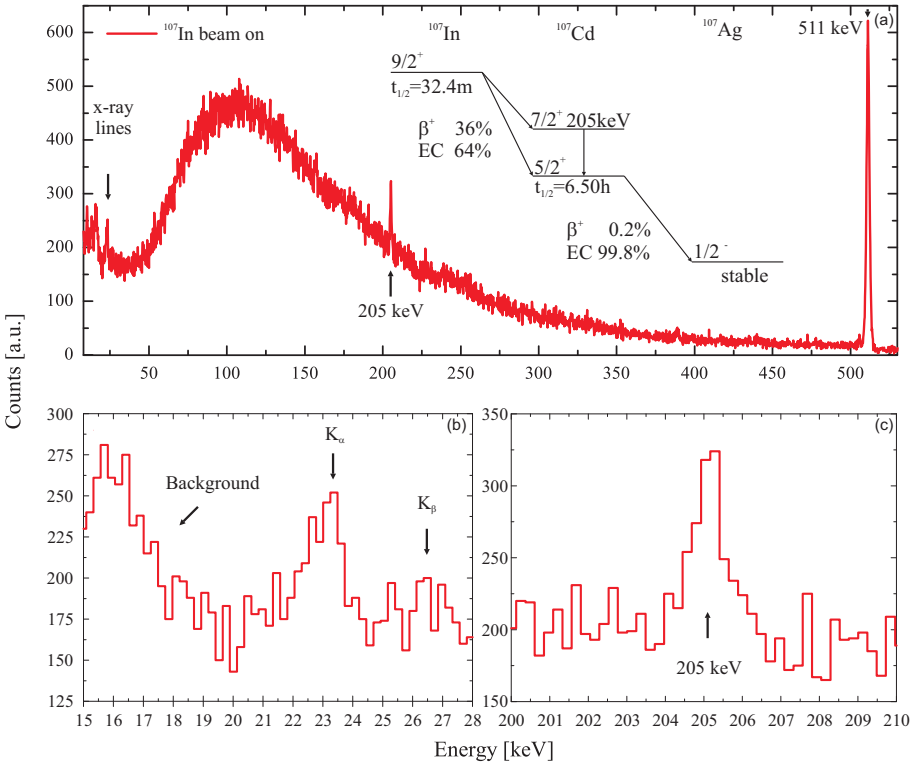

Figure 5.3: ^{107}In decay spectrum recorded with the Ge detector. (a) The whole spectrum showing the range from 10 keV up to 520 keV. (b) K_α and K_β x-ray signatures used to determine the ECBR of ^{107}In. The peak at 16 keV originates from intrinsic noise. It is not visible in the LeGe detector spectrum shown in Fig. 5.4. (c) The 204.95 keV [NND10] γ-line was used to determine the total number of decays that occurred inside the trap.

After the identification of ^{107}In, the ions were stored in the spectroscopy Penning trap for 1 s while their radioactive decays were observed with the LeGe and Ge detectors covering ∼0.02% and ∼0.25% solid angle, respectively. After the 1 s measurement period the trap was emptied by extracting the ions back into the beam line where they were deposited on an electrode. This was done to minimize background contributions from subsequent decays. The timing cycle of this measurement is displayed in Fig. 5.2(I-III). In order to reduce the radiation background, the detector DAQ system was gated such that it would only record spectra while ions were stored inside the trap. Background spectra were taken with the detectors before and after the ECBR measurement of ^{107}In, i.e., before ^{107}In was delivered to TITAN and after the measurement. The data acquisition was done with two DSPEC units recording data from LeGe and Ge detector.

The spectra recorded during the ECBR measurement of ^{107}In are displayed in Fig. 5.3 for the Ge detector, and Fig. 5.4 for the LeGe detector. The spectrum of the Ge detector was taken during the first hour of the experiment. Later, the delivered beam intensity dropped and it could not be verified whether In was injected and stored in the trap. The Ge detector spectrum was analyzed using Origin [Ori] with an adjusted fitting function consisting of a Gaussian and a smoothed step function, which accounts for low-angle scattering between source and detector. A detailed description of the contributions to a photo peak detected by a Ge detector is given for example in Ref. [Hel80, Haa06]. The 204.95 keV photo peak from the decay of the $7/2^+$ state in ^{107}Cd was used as reference. It was also considered to use the positron annihilation photons as a reference. However, during background measurements before the beam time the 511 keV annihilation line was found to have unexplained fluctuating intensities. Based on the measured peak intensities D_{meas}, the resulting ECBR was calculated using Eq.(5.5) applying ω_{k} from [Sch96b, Sch00] and I_{K}^{CE} from [NND10] to be $(53 \pm 20)\%$ and is in agreement with 64(3)% [NND10] and an independent analysis of this data, 55(20)% [Ett09].

Independent of the consistency of this result, additional effects should be considered. Ions could be lost out of the direct detection region of the Ge detectors during injection and extraction. In this case, the detectors would be shielded against x-rays while 205 keV photons could still reach them. This would lead to a decreased ECBR. Additionally, Ag x-rays from the decay product of ^{107}Cd overlap with Cd x-rays in the Ge detector spectrum. This introduces further uncertainties. The Ge detector resolution is not sufficient to resolve them while they are well separated in the LeGe spectrum. In the spectrum of the LeGe detector displayed in Fig. 5.4, the Ag x-ray lines dominate those of Cd while in the spectrum of the Ge detector it is the inverse as shown in Fig. 5.3. This difference originates from a difference in measurement time. The LeGe detector was accumulating data for a longer period of time than the Ge detector. Over time, Ag built up inside the trap and thus its contribution to the spectrum increased with longer measurement time. Background spectra were only taken before and immediately after the measurement. Therefore, the presence of the Ag line in the background spectrum is evident but it is not possible to determine the amount of ions lost inside the trap within the given uncertainty. The background contribution of ions lost inside the trap to the spectrum cannot be determined with the applied measurement cycle.

However, the ECBR of ^{107}In was the first time an EC was observed of ions stored in a Penning trap. This measurement proved the feasibility of this technique but also indicated issues that still needed to be addressed. Therefore, a second experiment was performed with ^{124,126}Cs based on the experience gained during the ^{107}In experiment with the goal to further refine the technique.

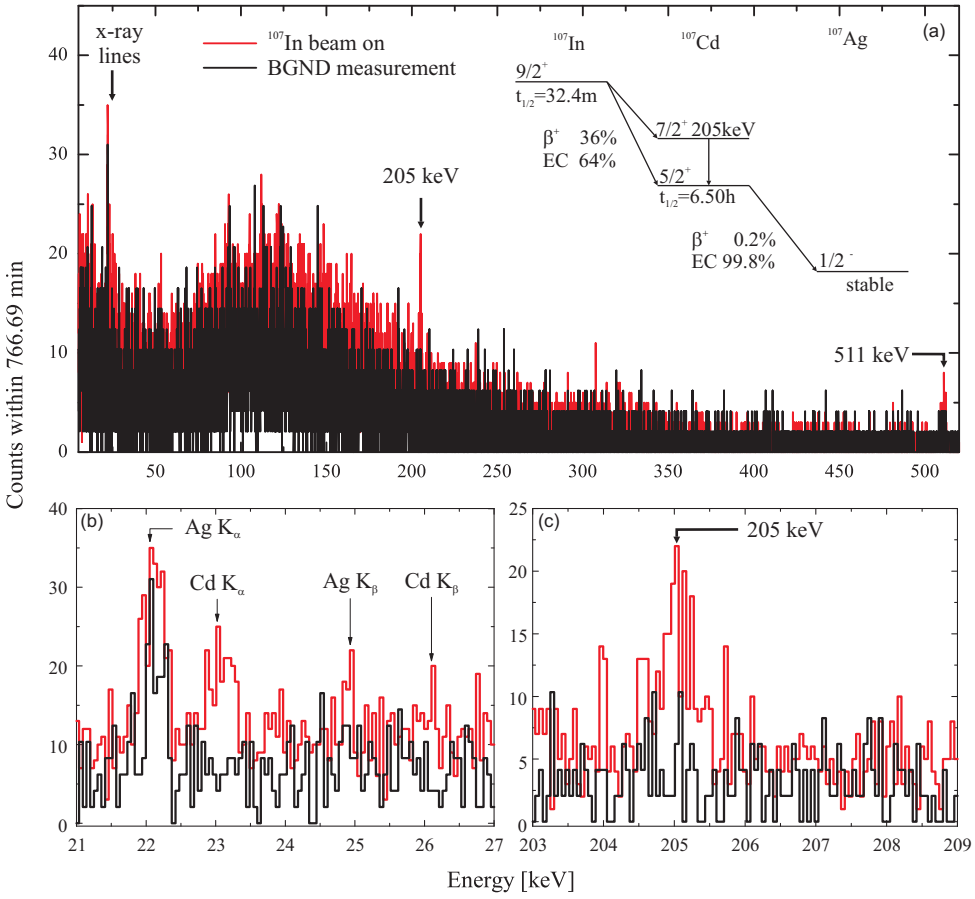

Figure 5.4: ^{107}In decay spectrum recorded with the LeGe detector. (a) The entire spectrum showing the range from 10 keV up to 520 keV. The decay scheme with relevant levels is also illustrated. (b) Cd and Ag x-ray signatures of the EC decays of ^{107}In and ^{107}Cd. (c) The 204.95 keV [NND10] γ-line was used to determine the total number of decays that happened inside the trap.

5.3 Systematic studies with ^{124,126}Cs

For the ECBR measurement of ^{124,126}Cs, a Ta high power target[1] was bombarded with a 50 µA proton beam from TRIUMF's cyclotron with 500 MeV energy. Cesium atoms were ionized by surface ionization and delivered to TITAN with 15 keV beam energy. The yields were $1.3 \cdot 10^7$/s for ^{124g}Cs, $2.5 \cdot 10^5$/s for ^{124m}Cs, $1.6 \cdot 10^7$/s for ^{126}Cs, and $8.8 \cdot 10^6$/s for ^{128}Cs, respectively, measured at the ISAC-I yield station [Kun09].

After being cooled and bunched by TITAN's RFQ, the ions were extracted into the TITAN beam line. Their schematic flight-path is illustrated in Fig. 5.5. Initially, the ions were implanted into the Monitoring PIPS assembly and identified by their half life. This transport path is indicated by the dashed red line in Fig. 5.5. During this measurement the number of ions per bunch was determined as described in Section 5.3.1. Ion bunches were then injected into the spectroscopy Penning trap as indicated by the red arrow in Fig. 5.5. While the ions were stored, their decays were observed as described in Section 5.4.3. After a certain storage time t_{storage}, the ions were extracted towards the MPET, implanted into the monitoring PIPS assembly (green arrow in Fig. 5.5) and a background measurement was performed for $t_{\text{background}} = t_{\text{storage}}$. The implantation of extracted ions into the monitoring PIPS assembly provides direct information on the measurement. If the beam intensity changes during the experiment, the β count rate of the monitoring PIPS changes and the system can be adjusted accordingly. Part of the β count rate recorded by the monitoring PIPS during the Cs experiment is displayed in Fig. 5.6. Arrows indicate some of the events that can be identified in the intensity plot. This method was tested and found to be a valuable monitoring technique during ECBR measurements.

5.3.1 Ion-bunch intensity determination with the Al-PIPS

After optimizing the tune of the RFQ as described in Section 4.1, ions were extracted from the RFQ and implanted into the monitoring PIPS[2] assembly (see Fig. 5.5) in order to identify the isotope delivered to TITAN and determine possible contaminations. Ten shots were typically extracted from the RFQ at a frequency of 10 Hz. After extraction of the last pulse from the RFQ, the data acquisition with the SR430 multi-channel scaler was initiated to recorded the β^+ intensity. Additionally, the split signal of the monitoring PIPS detector was sent to a monitor, a so-called ISAC scaler[3]. Based on the recorded spectra the isotopes, ^{124,126}Cs and possible contaminants were identified. It was assumed that the beam consists of the two isotopes A and B with the condition that A only decays to B which is unstable. A is considered the contaminant. Based on

[1] Target module #4, Ta high power target #28
[2] Al-PIPS-300
[3] ISAC scaler ILE2:SCALER:SCALER.S14.

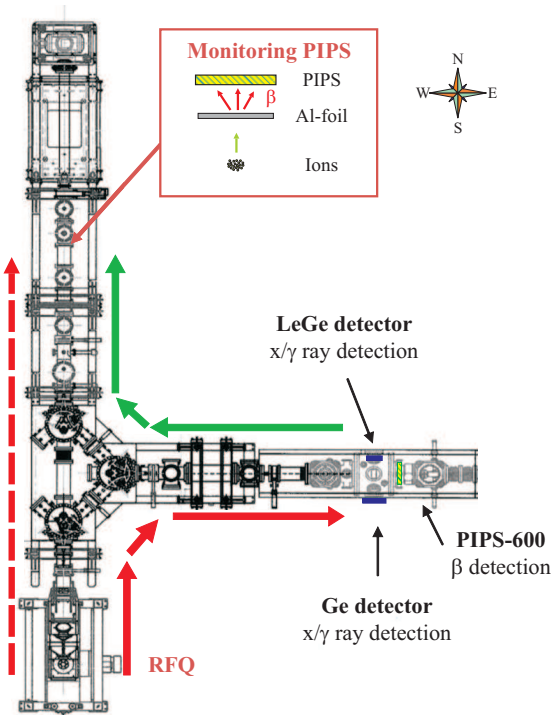

Figure 5.5: Ion path during a measurement. Ions from the RFQ are delivered to the Penning trap (red arrow) where their decay is observed. After a certain period of time they are extracted back into the beam line and implanted into an Al-foil in front of a β detector (red arrow).

the decay rates

$$\frac{\mathrm{d}n_A}{\mathrm{d}t} = -\lambda_A\, n_A^0 \qquad \text{and} \tag{5.9}$$

$$\frac{\mathrm{d}n_B}{\mathrm{d}t} = -\lambda_B\, n_B^0\,, \tag{5.10}$$

with the decay constants λ_A and λ_B as well as the number of nuclei n_A^0 and n_B^0 at $t = t_0$ of A and B, respectively, one can express the decay rate of the daughter isotope B as

$$\frac{\mathrm{d}n_B}{\mathrm{d}t} = -\lambda_A\, n_A^0 - \lambda_B\, n_B^0\,. \tag{5.11}$$

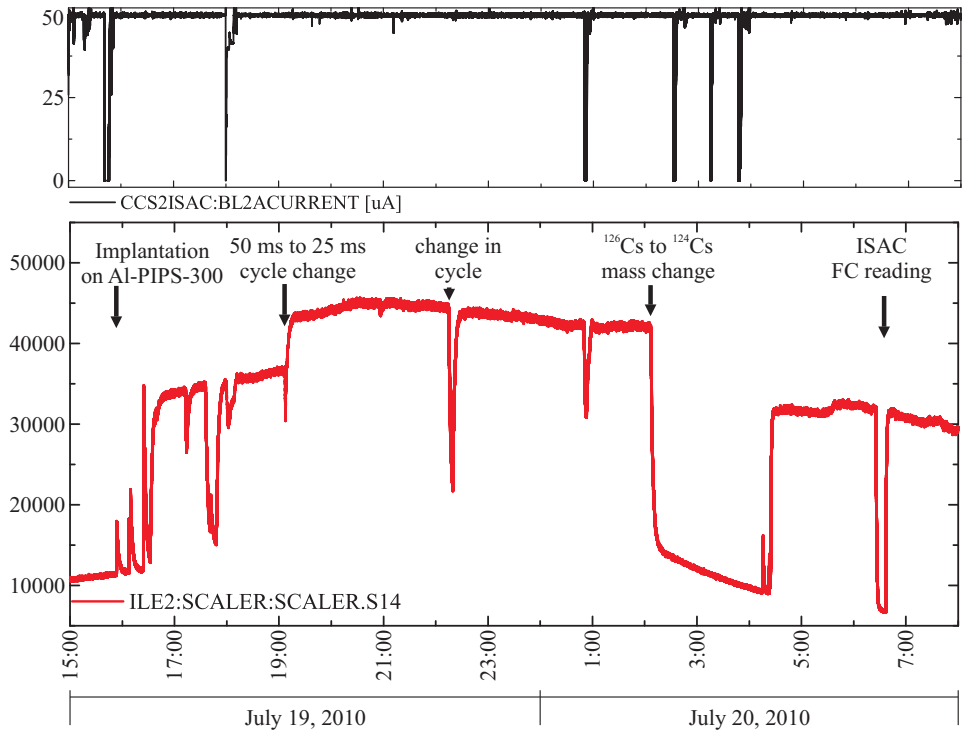

Figure 5.6: (top) Proton intensity and (bottom) β intensity on the monitoring PIPS assembly during the Cs ECBR experiment.

This differential equation of first order can be solved as described in Ref. [Bro01] and results in the equation

$$n_B(t) = \frac{\lambda_A}{\lambda_A - \lambda_b} n_A^0 \left\{\exp\left(-\lambda_A\left(t - t_0\right)\right) - \exp\left(-\lambda_B\left(t - t_0\right)\right)\right\} + n_B^0 \exp\left(-\lambda_b(t - t_0)\right). \tag{5.12}$$

In the case of ^{124}Cs this equation was used to investigate the ^{124m}Cs contamination.

The beam intensity per extracted shot from the RFQ was estimated assuming a total detection efficiency of $(25 \pm 10)\%$ for the monitoring PIPS assembly. This efficiency is the product of intrinsic detection efficiency and geometric detection efficiency. The latter is the main contribution to the uncertainty of the total efficiency due to the distance of (6 ± 1) mm between detector and Al foil. The intrinsic detection efficiency was calculated by integrating the β spectrum defined by Eq.(3.2). Based on this, an intrinsic detection efficiency of $\sim 99\%$ was determined assuming that electrons below 250 keV were stopped by the 20 µm thick Al foil and the detector's dead layer, and thus

not detected. The ion bunch intensity measurements of ^{124}Cs and ^{126}Cs are described separately in the following subsections and the results are summarized in Table 5.1.

Identification of ^{124}Cs

After determining the background count rate, ^{124g,m}Cs was implanted into the monitoring PIPS assembly and the count rate was recorded with the SR430 multi-channel scaler. For the half life measurement of ^{124g}Cs, a delay of 30 s was used to trigger the multi-channel scaler. This delay corresponds to ~ 4.5 times the half life of ^{124m}Cs and thus only $\sim 4\%$ of ^{124m}Cs did not decay by the time the measurement was started. The resulting half life of ^{124g}Cs was measured to be 30.94(10) s and is in agreement with 30.8(5) s [NND10].

The beam intensity was determined by implanting 10 ion bunches at 10 Hz repetition rate into the Al foil. Counting with the SR430 began 1006.7 ms after the first bunch was extracted from the RFQ, i.e., directly after all bunches hit the Al foil. The flight time for $^{126}Z^{1+}$ from RFQ to monitoring PIPS assembly with 2 keV beam energy is about 120 µs. The decay curve was then fitted with Eq.(5.12). During the fit only n_A and n_B were varied while λ_A and λ_B were kept constant at 6.3(2) s [NND10]. The background was determined to be 23.2(8) counts/s in a measurement performed prior to the implantation. A minimal χ^2/d.o.f.=1.19096 was determined for $n_A^0 = 0$. This result agrees with a contamination of about 2% as determined by yield station measurements. Based on the assumption that the contamination of ^{124}Cs is negligible, the decay data was analyzed using Eq.(5.10). Based on the fit, the total number of atoms exposed to the detector was determined to be $6.9(2) \cdot 10^5$ for 10 shots. Assuming a detection efficiency of (25±10)%, the beam intensity is estimated to be $2.8(11) \cdot 10^5$ ions per bunch at an extraction rate of 10 Hz. The ion beam current entering the RFQ was measured to be $I_{\mathrm{ISAC}} \sim 3 \cdot 10^{-12}$ A$\approx 19 \cdot 10^6$ ions/s at FC3. Based on these measurements, the efficiency of the RFQ was estimated to be about 10% in bunched operation at 10 Hz. Further spectra with different repetition rates were also recorded. The resulting efficiencies are consistent.

In addition, an attempt was made to identify ^{124}Ba as a possible contaminant. The half life of 11.0(5) min [NND10] is long compared to that of ^{124m,g}Cs and thus it was not possible to identify ^{124}Ba with this setup. In the SR430 spectrum, the count rate was dominated by ^{124}Cs and the ISAC scaler fluctuated on that time scale.

The presented measurements were performed at an RFQ gas-flow rate of 5 sccm$\widehat{=}4.4 \cdot 10^{-5}$ mbar. As mentioned earlier, at the time of the experiment it was assumed that this flow rate is sufficient to stop all incoming ions in the RFQ. In subsequent investigations this was found not to be the case. Therefore, the transmission through the RFQ in pulsed operation could be considered to be even higher.

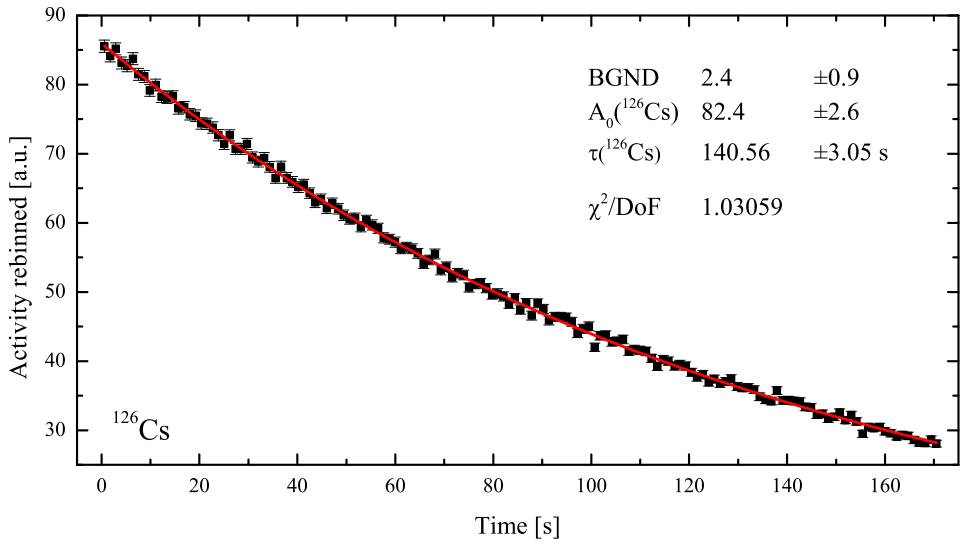

Figure 5.7: Decay curve of ten ion bunches of ^{126}Cs, extracted from the RFQ and implanted into the monitoring PIPS assembly. The rate was recorded with the SR430 multi-channel scaler.

Identification of ^{126}Cs

The isotope ^{126}Cs was identified with a method similar to that for the identification of ^{124}Cs. Radioactive isotopes were extracted in bunches from the RFQ and implanted into the monitoring PIPS assembly. The half life of ^{126}Cs was measured to be 97.4(21) s and agrees with 98.4(12) s [NND10]. This value was determined from 10 shots implanted into the Al foil. The decay curve is displayed in Fig. 5.7. Following the first measurement, two more measurements were performed with 10 shots and 100 shots extracted from the RFQ. The measured half lives were 100.8(18) s and 109.4(15) s, respectively. The increase in the identified half life resulted from ^{126}Ba contamination that was built up on the Al foil. The resulting spectra therefore consisted of two components and needed to be convoluted. It was attempted to estimate this contamination by analyzing the data recorded by ISAC's scaler but the scaler output was unstable and drifted over time as mentioned earlier. Therefore, with the recorded data it was not possible to get constraints on the ^{126}Ba contamination.

The first ten ion pulses implanted into the monitoring PIPS assembly with a repetition rate of 10 Hz were analyzed in order to determine the number of ions per shot. The

Isotope	Half life this work	Half life NNDC [NND10]	Intensity per bunch @ 10 Hz	Intensity at FC3
^{124g}Cs	30.94(10) s	30.8(5) s	$2.8(11) \cdot 10^5$	$\sim 3 \cdot 10^{-12}$ A
^{124m}Cs		6.3(2) s		
^{126}Cs	1.59(6) min	1.64(2) min	$4.4(21) \cdot 10^5$	$\sim 1 \cdot 10^{-11}$ A
^{126}Ba		100(2) min		

Table 5.1: Half lives and beam intensities that were determined during the ^{124,126}Cs measurement.

total number of nuclei whose decay was detected by the PIPS detector was determined to be $1.1(3) \cdot 10^6$ for 10 shots. With the total detection efficiency of (25±10)% this calculates to $4.4(21) \cdot 10^5$ ions per shot extracted from the RFQ at a repetition rate of 10 Hz. About two hours prior to and after this measurement, a beam intensity of $I_{\mathrm{ISAC}} \sim 1 \cdot 10^{-11}$ A $\approx 6 \cdot 10^7$ ions/s was measured at FC3 going into the RFQ. Based on this ion current the transmission of the RFQ was determined to be about 1%. This is a factor 10 less than the RFQ efficiency determined with ^{124}Cs. It is noted here that the applied technique was aimed at identifying the delivered isotope. The method was neither optimized for β decay spectroscopy nor was it calibrated. Based on the measurements presented here, the RFQ-transmission in pulsed operation at 10 Hz repetition rate is determined to be 1-10%. This efficiency agrees with typical RFQ efficiencies as well as with observations during other experiments at TITAN with low intensity ion beams [Bro10b]. However, this measurement provided the first efficiency estimate with more than 10^4 ions/s entering TITAN's RFQ. All results are summarized in Tab. 5.1.

Apart from isotope identification, the monitoring PIPS assembly was used to monitor the stored isotope intensity during the ECBR measurement of ^{124,126}Cs as illustrated in Fig. 5.6.

5.3.2 LeGe detector background investigation

Before radioactive ions were injected into the trap, background spectra were recorded with the LeGe detector placed 100 mm away from the trap center, i.e., at its position during the experiment. The recorded background spectrum was normalized to an exposure time of 1 hour and is displayed in Fig. 5.8 (blue spectrum).

During the experiment with radioactive ^{124,126}Cs, further background measurements were performed while ^{126}Cs was deposited in the RFQ without being extracted. The resulting spectrum is displayed in Fig. 5.8 (red spectrum). This spectrum was also

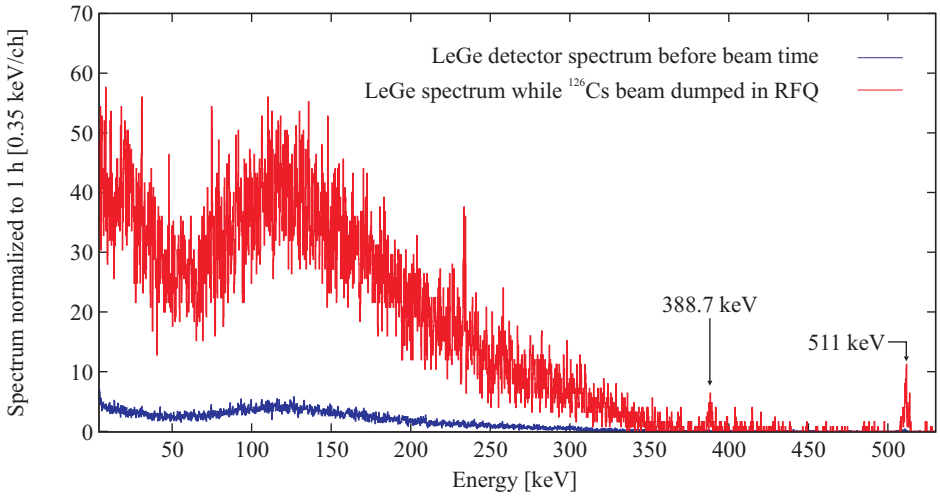

Figure 5.8: LeGe detector background spectrum recorded prior to the beam time and while ^{126}Cs was dumped in the RFQ. The spectrum was normalized to 1 hour. See text for explanation.

normalized to 1 hour measurement time. Prior to this measurement, no ions were delivered to TITAN for about 5 hours to allow all previously deposited cesium and barium to decay. The activity deposited in the RFQ increased the background level by about one order of magnitude. Well separated are the 388.66 keV and 511 keV lines from the decay of ^{126}Cs and positron annihilation, respectively. The fact that higher energetic lines of ions lost inside the RFQ contributed to the spectrum has to be considered in the analysis and future developments.

5.3.3 $\beta^+ - \gamma$ coincidences

During the ^{124,126}Cs measurement, Ge and PIPS detector signals were digitized using the tig10 sampling ADC [Mar08]. Typically, the tig10 was only recording data while ions were stored in the trap. The trigger algorithm triggered on the signal height of single samples and therefore, the trigger was susceptible to noise. As a result, the recorded photon spectrum of the Ge detector below ∼40 keV strongly depended on the applied trigger threshold. In systematic studies prior to the beam time it was not possible to record reproducible x-ray spectra [Bru09]. Therefore, during the Cs experiment the Ge detector recorded γ rays above ∼40 keV. The recorded data set consisted of β and γ events that could be investigated under consideration of coincident events. Neither PIPS nor the Ge detector were used to determine the ECBR of ^{124,126}Cs, but were used for systematic studies.

The recorded normalized β spectra of ^{124,126}Cs are displayed in Fig. 5.9. In the case of ^{124}Cs, the high energy side of the spectrum has more counts than in the case of ^{126}Cs. This is due to the fact that the Q value of ^{124}Cs is about 1 MeV greater than of ^{126}Cs.

When ^{126}Cs was first injected into the trap, the PIPS detector was rotated away from the trap so that it would face the electron gun. In this position, no β particles were counted. When rotated back and facing towards the trap center, positrons were detected. This verified that the PIPS detector was actually measuring β particles originating from in-trap decays.

Instantly after the measurement of ^{124}Cs, background measurements were initiated counting beta intensity during $\sim$ 4 hours following the experiment. The β count rate decayed exponentially indicating that ions were implanted into the PIPS detector. This can be explained by the symmetric trapping potential that was applied during the experiment as shown in Fig. 4.5c. During the injection process, the guard electrode was switched to a low potential to allow ions to enter the trap as displayed in Fig. 4.5b. Slow ions arriving after the ion bunch, were still in the region of the guard electrode while the electrode was switched to a high potential to confine the main ion bunch. This then acts as an 'ion elevator' increasing the potential energy of the slow ions so that they were not confined anymore by the guard electrode facing the PIPS detector. This background source has to be considered in future experiments. A solution would be to increase the voltage of the PIPS-facing guard electrode to reflect all ions that would otherwise impinge on the PIPS detector.

The photon spectra recorded with the Ge detector are displayed in Fig. 5.10. Also displayed are γ events that occurred in coincidence with a β event. Considering the difference in intensity, one concludes that the coincidence is soft. The time difference $t_\gamma - t_\beta$ between γ and β detection is plotted in Fig. 5.11 for photon energies in the peak range of 354 keV and 511 keV. The signal of a beta event is processed much faster than that of a photon event. Therefore, all events with a time difference smaller than zero are random coincidences.

5.4 In-trap decay spectroscopy of ^{124,126}Cs

During the analysis of the ^{107}In ECBR measurement, it was found that the cycle used was not optimal to perform in-trap decay spectroscopy. First, background spectra were only taken after several hours of storing radioactive ions and measuring their decays. Hence, little information on losses inside the trap was gained. Second, a storage time of 1 s was acceptable for the storage of ^{107}In in a trap with a 4 T magnetic field. For the ECBR measurement of ^{124,126}Cs the magnetic field was increased to 5 T to better confine β particles. This was necessary due to the Q values of 5929(9) for ^{124}Cs and 4824(14) for

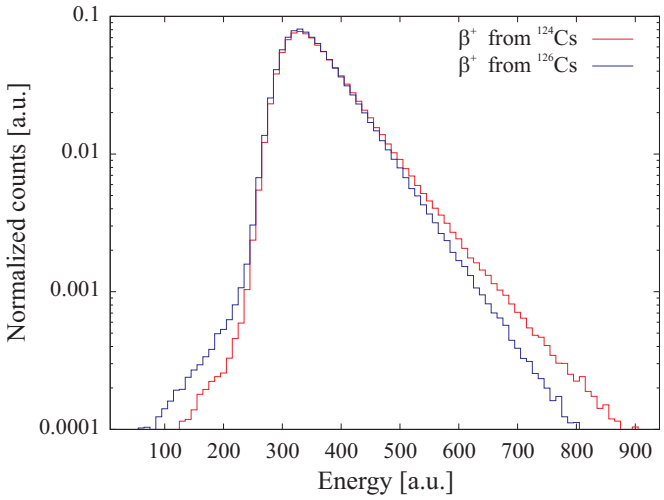

Figure 5.9: Normalized β^+ spectrum of ^{124,126}Cs recorded with the PIPS detector. Both spectra were summed over several hours of data-taking and then normalized to the area.

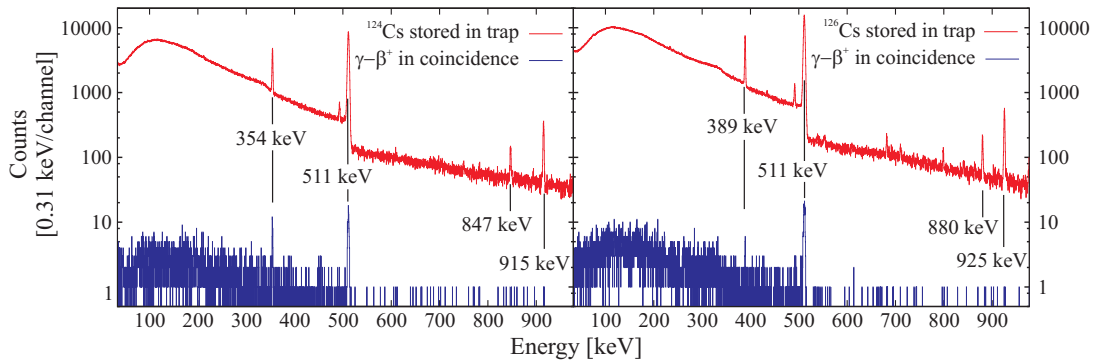

Figure 5.10: ^{124,126}Cs spectra recorded with the Ge detector. The detector was set up to only record data during t_{storage}, i.e., when ions were stored inside the trap. The blue spectrum are photon events that were recorded in coincidence with β^+ events.

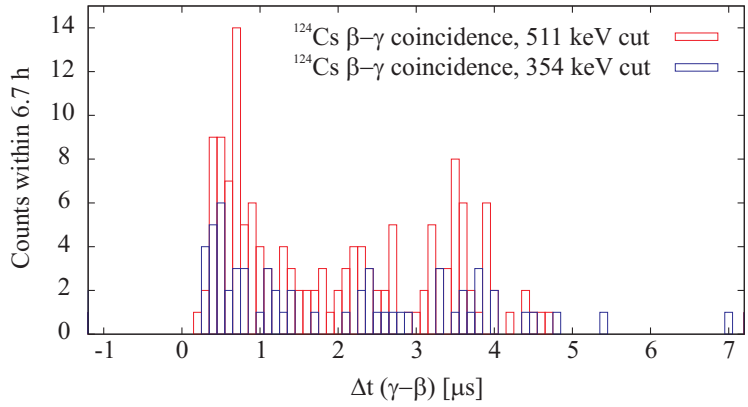

Figure 5.11: $\beta^+ - \gamma$ time correlation recorded with Ge and PIPS detector.

^{126}Cs [NND10]. Subsequent storage time measurements with the spectroscopy Penning trap (Section 4.3) showed that shorter storage times are favorable for ion storage in higher magnetic fields. To address these two issues the timing and measuring cycle was changed for the ^{124,126}Cs measurement. In this newly developed cycle ions were injected into the Penning trap where they were captured for the period t_{storage} while their decays were observed. During the measurement with ^{126}Cs the storage times $t_{\text{storage}} = 25\,\text{ms}$ and $t_{\text{storage}} = 50\,\text{ms}$ were applied, ^{124}Cs was stored for $t_{\text{storage}} = 25\,\text{ms}$. Afterwards the trap was opened to extract the ions and after 1 ms a background spectrum was recorded for $t_{\text{BGND}} = t_{\text{storage}}$. The cycle then started again with the injection of ions into the trap. Therefore, one full cycle t_{cycle} consisted of t_{BGND}, t_{storage}, and the transition time t_{trans}. Under the condition that no ions are lost inside the trap, the total number of decays n in a measurement time T calculates to

$$\begin{aligned} n\left(t_{\text{storage}}, t_{\text{BGND}}\right) &= \frac{T}{t_{\text{cycle}}} N_0 \left(1 - e^{-\frac{t_{\text{storage}}}{\tau}}\right) \\ &= \frac{T}{t_{\text{BGND}} + t_{\text{storage}} + t_{\text{trans}}} N_0 \left(1 - e^{-\frac{t_{\text{storage}}}{\tau}}\right), \end{aligned} \tag{5.13}$$

assuming a constant ion bunch intensity N_0. For a given transition time t_{trans} the times t_{BGND} and t_{storage} can be varied to optimize the number of decays n that happen within the measurement time T. Fig. 5.12 displays $n\left(t_{\text{storage}}, t_{\text{BGND}}\right)$. During the experiment, the detector signal was split and fed to two data acquisition units that recorded spectra either during t_{storage} or t_{BGND}. The ^{124,126}Cs measurement cycle is displayed on the right side of Fig. 5.2.

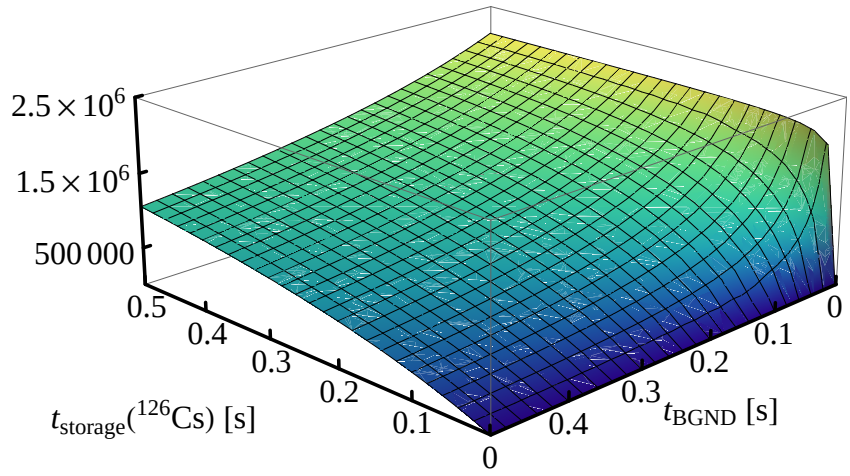

Figure 5.12: Calculated number of decays $n\,(t_{\mathrm{storage}}, t_{\mathrm{BGND}})$ for a measurement period of $T = 1\,\mathrm{hour}$ and $1 \cdot 10^5$ ions/bunch.

5.4.1 Split LeGe-detector signal

The split LeGe detector output signal was sent to two DSPEC units in order to record spectra either while ions were captured or immediately after the extraction and before the next ion bunch was injected. The units DSPEC 319 and DSPEC 321 were gated with the EBIT ppg (programmable pulse generator) NIM signal to only record data during t_{storage} and t_{BGND}, respectively. A schematic of this DAQ setup is displayed in Fig B.3. The settings of both DSPEC units are listed in Table B.1.

A ^{133}Ba source was placed at the Be window at the South side of the trap opposite the LeGe detector (see Fig. 3.19) to investigate the effect of splitting the LeGe detector signal and feeding it to two DSPEC units. First, both DSPEC units were recording data simultaneously without being gated. These spectra were analyzed and the fraction of DSPEC 319 versus DSPEC 321 was calculated. This fraction is illustrated for different photo peaks on the left in Fig. 5.13. The fitted peak-area ratios calculate to 1.003(17) and 1.000(25) for 30.6 keV and 81.0 keV, respectively. The K_β lines that are emitted from the ^{133}Ba source were difficult to fit. Therefore, these K_β peak areas were integrated and their intensities agreed for both DSPECs. The integrated peak-area ratio is illustrated by blue dots in Fig. 5.13 and all areas are listed in Table B.3. Based on these results, one concluded that both DSPEC units recorded data with the same efficiency.

In the same setup, both DSPEC units were gated applying the actual timing cycle presented in the previous section. The times t_{storage} and t_{BGND} were set to 50 ms. The large distance between detector and source in combination with a dead time of more

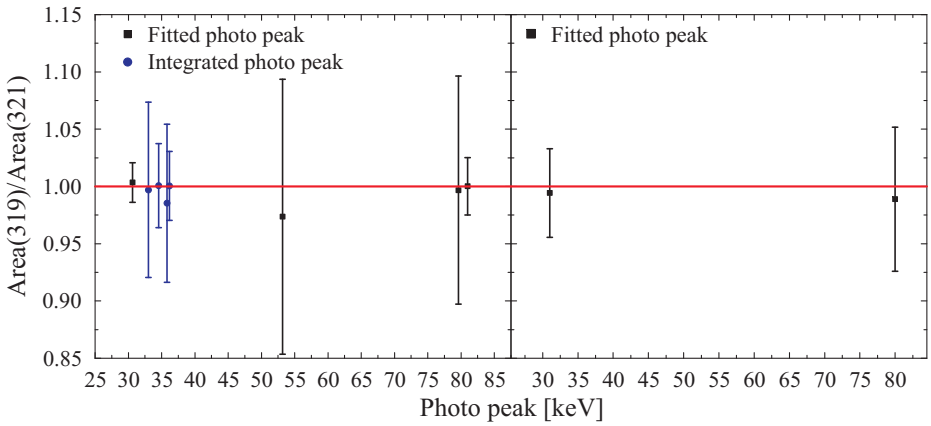

Figure 5.13: Fraction of peak areas recorded with the split signal DSPEC setup with non-gated data acquisition (left) and gated data acquisition (right). The values are listed in Table B.3. Black squares represent peak areas fitted with [Sju09] and blue points represent the ratio of integrated photo peak regions.

than 50% due to the gating resulted in few counts in the spectrum. Hence, reliable results could only be obtained for the K_α peaks and the photo peak at 81 keV. Again, the peak areas agree within uncertainty and the ratios of gated DSPEC319 to gated DSPEC321 are 0.994(39) for the 30.6 keV peak and 0.989(63) for the 81 keV peak as displayed on the right side of Fig. 5.13. From this comparison one infers that the timing cycles t_{storage} and t_{BGND} are identical.

Throughout the ^{124,126}Cs experiment, calibration spectra with ^{133}Ba were recorded repeatedly. The centroids of the 35 keV and 81 keV photo peak shifted less than 1 channel$\hat{=}$ 0.0330(5)keV over 35 hours. The time-dependent centroid positions of the split-signal data acquisition are displayed in Fig. 5.14. This agrees with systematic studies performed before the online measurement.

However, during the analysis of the online beam time data it was discovered that both DSPECs truncated energy events above $\sim$ 120 keV. Due to this truncation, the efficiency for higher energetic photons drops off several orders of magnitude faster than one would expect for a Ge crystal of that particular size. This introduced an additional systematic uncertainty to the measurement and is discussed later in this chapter.

5.4.2 Analysis of the recorded ^{124,126}Cs spectra

During the cesium online beam time, radioactive Cs was injected into the spectroscopy trap and x-rays following an electron capture were detected along with the emitted positrons. The cycle listed on the right side of Fig. 5.2 was applied and spectra were

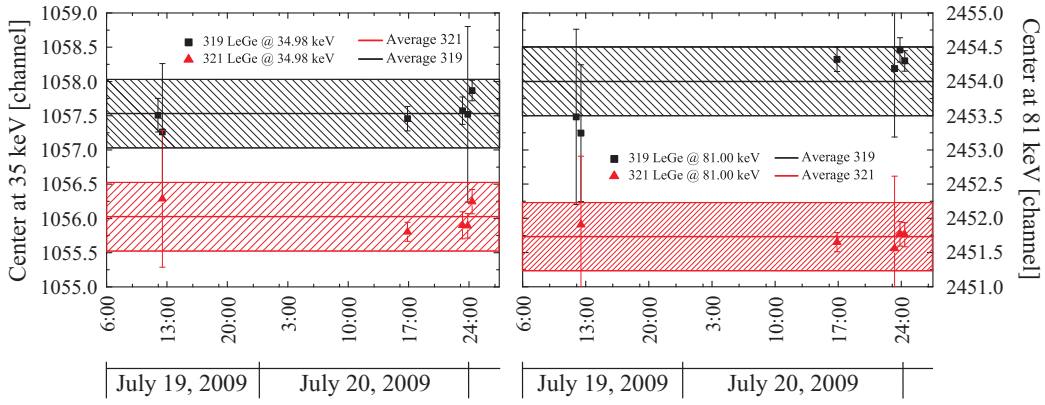

Figure 5.14: Centroid channel of the (left) 35 keV and (right) 81 keV ^{133}Ba photo peaks throughout the ^{124,126}Cs experiment.

recorded with DSPEC 319 while ions were stored inside the trap, and with DSPEC 321 during the background measurement immediately after ion storage. The data was recorded in so-called blocks. Each block typically consisted of several one-hours spectra of continuous beam delivery with constant settings. The DSPEC units recorded pulse-height spectra of typically one hour that were read out and stored by a computer.

The recording efficiency of both DSPEC units was considered equal based on the results presented in the previous section, i.e., the spectra were not weighted. In order to achieve higher statistics the spectra of each block were added channel by channel. This is reasonable since the shift over several hours is less than 1 channel $\hat{=}$ 0.0330(5) keV as previously mentioned. If the settings of two different blocks remained the same, these blocks were also added channel by channel.

The summed spectra were then analyzed with the following method. Photo peaks in the x-ray region were fitted with a FORTRAN code [Sju09]. Within the fit, K-shell x-ray energy and relative intensity were kept constant at the literature value [Tho09]. Typically, the x-ray lines of Cs and Xe were fitted simultaneously. The code applied a maximum likelihood method to determine the peak areas. The resulting peak areas were $D^{peak}_{storage}$ and D^{peak}_{BGND} recorded with DSPEC 319 during $t_{storage}$ and DSPEC 321 during t_{BGND}, respectively. The widths of the peaks were determined in the analysis of $D^{peak}_{storage}$ photo peaks. These widths were then kept constant in the analysis of the background spectra. This procedure was also applied in the analysis of the ^{124m}Cs γ lines.

The influence of the magnetic field on the peak shape increases with increasing field strength as mentioned in Section 3.4.3. As a result, the peak is broadened with a tail on the low-energy side. In order to be independent of the peak shape the γ lines at 354 keV and 388 keV were integrated using TV [The]. Two background regions were

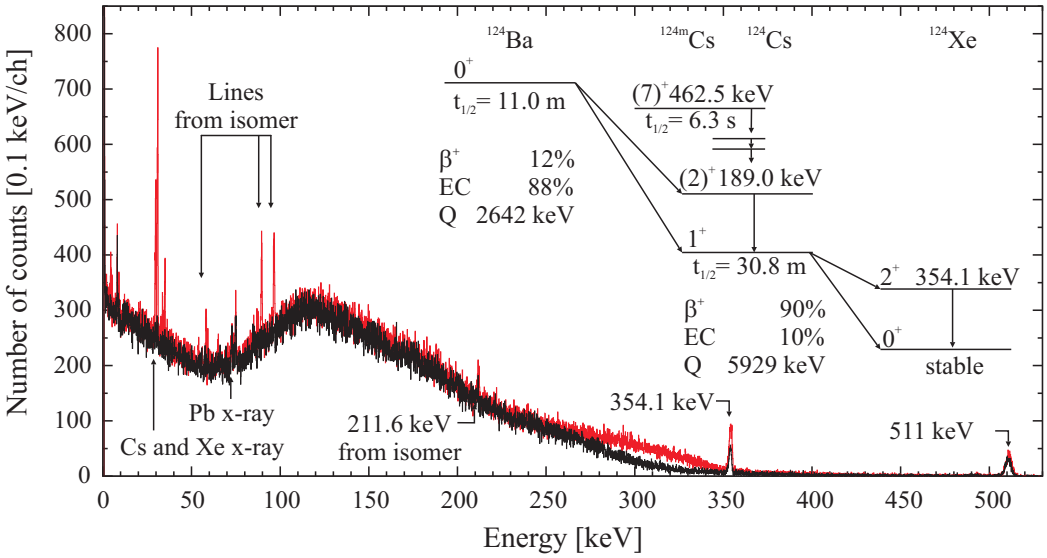

Figure 5.15: Photon spectrum of (red) ^{124}Cs in-trap decay and (black) background measurement. Displayed is the sum of all spectra (6 h).

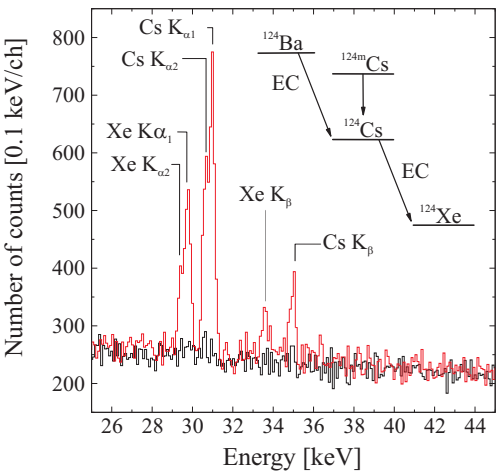

Figure 5.16: (Red) X-ray signature of ^{124}Cs EC decay and (black) background measurement. The spectrum is the sum of all spectra.

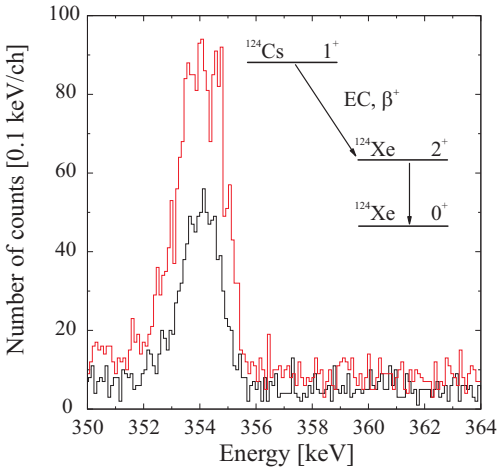

Figure 5.17: (Red) 354 keV line of ^{124}Cs $\xrightarrow{\beta^+}$ ^{124}Xe in-trap decay and (black) background measurement. The spectrum is the sum of all spectra.

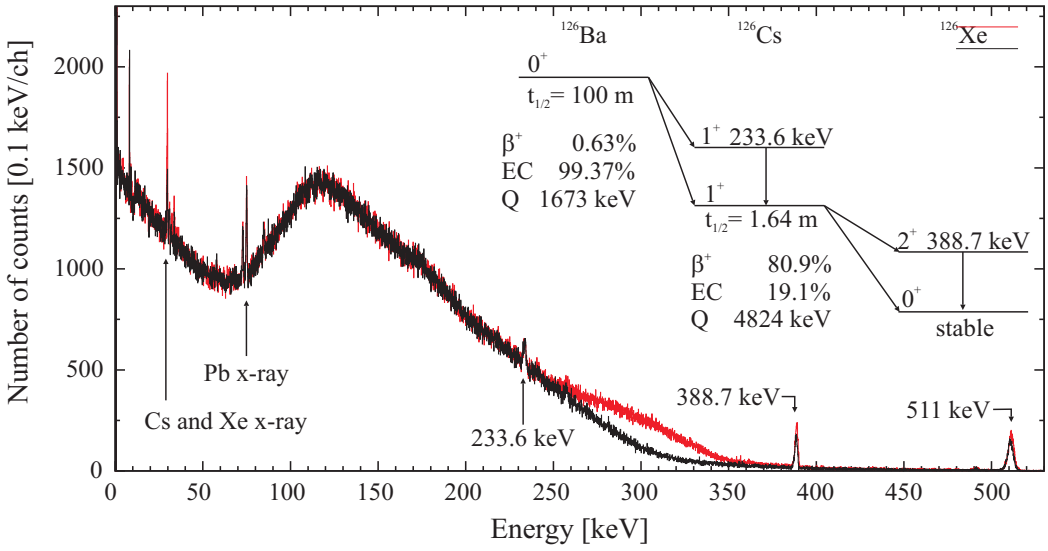

Figure 5.18: Photon spectrum of (red) ^{126}Cs in-trap decay and (black) background measurement. Displayed is the sum of all spectra (12 h).

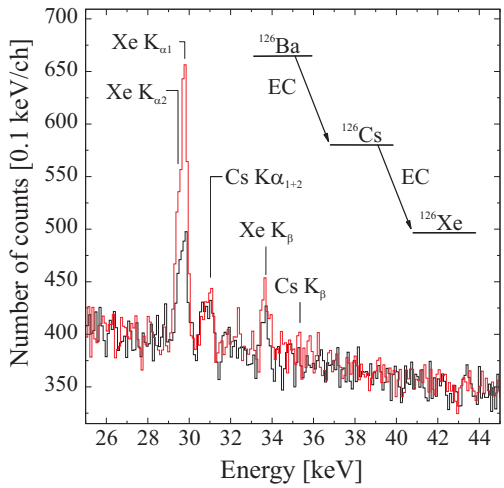

Figure 5.19: (Red) X-ray signature of ^{126}Cs EC in-trap decay and (black) background measurement.

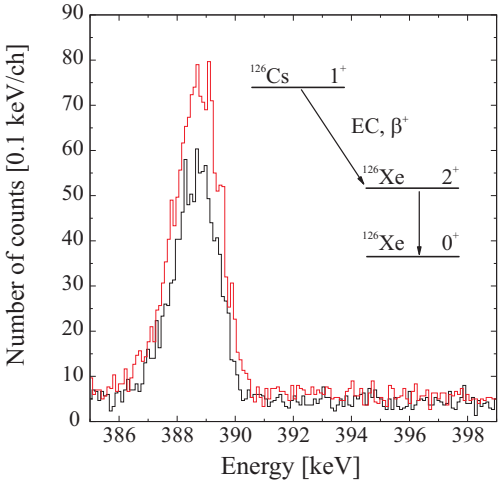

Figure 5.20: (Red) 388.7 keV line of ^{126}Cs $\xrightarrow{\beta^+}$ ^{126}Xe in-trap decay and (black) background measurement.

defined on either side of the photo peak with a range equal to the integration region. Based on the counts in the background regions the background subtracted peak area was determined. As a consistency check the peaks were also analyzed using [The] and [Sju09]. All determined peak areas agree within their uncertainties.

The results of this analysis are displayed in Table 5.2 for all ECBR relevant photo peaks of all ^{126}Cs blocks. The peak areas obtained for ^{124}Cs are listed in Table 5.3. The Xe x-ray peak areas were weighted with $\sqrt{\chi^2/\text{d.o.f.}}$ while the γ ray uncertainties were determined using [The].

Block	Duration [h]	x-ray peak	388 keV γ ray peak	
7	3	1219(73)	1038(42)	storage
8	3	400(66)	704(31)	BGND
9	1	591(53)	479(26)	storage
10	1	164(45)	382(22)	BGND
11	2	865(66)	896(34)	storage
12	2	495(62)	730(30)	BGND
13	3	1055(75)	947(35)	storage
14	3	514(62)	667(29)	BGND
15	3	964(69)	799(32)	storage
16	3	480(58)	603(27)	BGND
13+15	6	2129(104)	1741(57)	storage
14+16	6	1086(865)	1227(42)	BGND

Table 5.2: Peak areas recorded during the ^{126}Cs in-trap decay spectroscopy measurement. X-ray values were fitted using [Sju09] while γ ray peaks were integrated using [The].

The summed ^{124,126}Cs spectra are displayed in Fig. 5.15 and Fig. 5.18, respectively. X-ray and γ peaks are presented in detail in Fig. 5.16 and Fig. 5.17, and Fig. 5.19 and Fig. 5.20 for ^{124}Cs and ^{126}Cs, respectively. In these plots, both spectra of ion storage and background measurement are presented. Analyzing, these spectra some facts arose that are discussed in the following bulleted list:

- **Photo peaks in the background spectra**
  In principle, one expects photo peaks in the spectrum while ions were stored and no peaks during background measurements. However, in both storage and

Block	Duration [h]	x-ray peak	354 keV γ ray peak	
5	4	94(43)	549(28)	BGND
6	4	1074(66)	1152(40)	storage
7	2	490(42)	534(27)	storage
8	2	0(10)	285(19)	BGND
5+8	6	150(54)	817(34)	BGND
6+7	6	1657(77)	1661(58)	storage

Table 5.3: Peak areas recorded during the ^{124}Cs in-trap decay-spectroscopy measurement. X-ray values were fitted using [Sju09] while γ ray peaks were integrated using [The].

background spectra, photo peaks were present indicating ion losses. If ions were lost radially while being stored in the trap, they were deposited in direct detection range of the LeGe detector. Ions lost along the beam line or at the guard electrode were deposited out of direct detection range of the LeGe detector, i.e., photons were attenuated by the material between deposition site and detector. This was verified in Penelope2008 [Sal08] simulations with a ^{124g,124m,126}Cs source placed at the guard electrode (45 mm distance from the trap center along the trap axis). The source position is indicated in Fig. E.1. Simulated photons with 58 keV and less could not reach the detector, while 96 keV photons were detected. The detection efficiency increased with increasing photon energy. Simulated energies and their detected fractions are listed in Table E.4. Note that the fraction of detected photons is listed, not the fraction of photons reaching the detector. These simulations are described in detail in Appendix E.

Ions lost in the RFQ or along the beam line also contributed to the photon spectrum. This was found during background measurements with ^{126}Cs being deposited in the RFQ. The 388 keV and 511 keV lines were present in the LeGe detector spectrum as presented earlier. Based on this measurement and simulation one concludes that ^{124}Cs and ^{126}Cs were lost outside the trap and contributed to the background spectrum. The difference in the x-ray region between ^{124}Cs and ^{126}Cs indicated that ^{126}Cs was lost radially inside the trap (see Fig. 5.19) while ^{124}Cs was lost dominantly out of direct sight of the LeGe detector (see Fig. 5.16), i.e., outside the trap.

Both isotopes ^{124,126}Cs were injected with different tunes, the so-called $Tune(^{124}Cs)$ and $Tune(^{126}$Cs). Then, the photo peak fractions $R^{isotope}_{peak}(Tune)$ of in-trap decay spectrum and background measurement were calculated and compared for x-ray and γ photons. If ^{126}Cs was injected with $Tune(^{126}$Cs), $R^{^{126}\mathrm{Cs}}_{\mathrm{Xe}\ x-ray}$ was bout 1.5 times larger than when it was injected with $Tune(^{124}$Cs).

However, ^{124}Cs injected with $Tune(^{124}\mathrm{Cs})$ resulted in $R^{^{124}\mathrm{Cs}}_{^{\mathrm{Xe}}\ x-ray}$ that was about 4 times larger than $R^{^{126}\mathrm{Cs}}_{^{\mathrm{Xe}}\ x-ray}(Tune(^{126}\mathrm{Cs}))$ and about 8 times larger than $R^{^{126}\mathrm{Cs}}_{^{\mathrm{Xe}}\ x-ray}(Tune(^{126}\mathrm{Cs}))$. The fractions of the γ line at 354 keV and 389 keV for ^{124,126}Cs respectively, were calculated to 2.03(11), 1.42(6), and 1.54(9) for $R^{^{124}\mathrm{Cs}}_{^{\mathrm{Xe}}\ x-ray}(Tune(^{124}\mathrm{Cs}))$, $R^{^{126}\mathrm{Cs}}_{^{\mathrm{Xe}}\ x-ray}(Tune(^{124}\mathrm{Cs}))$, and $R^{^{126}\mathrm{Cs}}_{^{\mathrm{Xe}}\ x-ray}(Tune(^{126}\mathrm{Cs}))$, respectively. The presented results do not allow a conclusion on the correlation between tune and storage efficiency. The measured yields were similar so that the effect of the beam intensity was not investigated in this work. This effect should be investigated in further systematic studies on in-trap decay spectroscopy.

- **Shape of the spectrum**
  Considering the intrinsic detection efficiency displayed in Fig. 3.18, one expects a rather flat spectrum. Calibration spectra recorded with the LeGe detector as well as Penelope2008 simulations showed typical photon spectra with photo peaks, Compton peaks, and a flat Compton shoulder. However, the recorded spectra were camel-back shaped with an intensity minimum around 60 keV. The spectrum shape was similar in background measurements before the beam time and while ^{126}Cs was deposited in the RFQ, indicating that positron induced radiation, i.e., bremsstrahlung and annihilation, was causing this special shape.

- **Shoulder between 300 and 350 keV**
  For both Cs isotopes, a shoulder is visible in the energy range 300 to 350 keV of the stored ion spectra. Possible explanations are radiative electron capture (see for example [Gla56, Pac07]), synchrotron radiation, and the Compton edge [Kno00]. In Ref. [Mor40] the number of γ quanta emitted per captured K electron is approximated by $(\alpha/12\,\pi)(W/m\,c^2)^2$. With $W = Q + m\,c^2$ being the energy available in an electron capture and α the fine-structure constant, one calculates that in about 3% of all ^{124}Cs K shell EC, photons with continuous energy distribution were emitted. Therefore, the contribution of radiative electron capture to the spectrum was negligible. Synchrotron radiation can be excluded because the photon energy emitted by a positron with 4.9 MeV kinetic energy in a 5 T magnetic field calculates to < 6 meV, depending on the pitch angle of the positron in the magnetic field.

  The Compton edge of 511 keV photons from positron annihilation is located at 340.7 keV and lies within the range of the shoulder. In both cases ^{124,126}Cs, the shoulder is located at the same position. Therefore, this shoulder is identified as the Compton edge of 511 keV positrons.

The x-ray photo peak areas of ^{124,126}Cs, and the 89.5 keV and 96.6 keV lines of $^{124\mathrm{m}}$Cs were used to estimate the number of ions that were injected into the trap. These peaks were chosen to determine the ion bunch intensity since in the region below $\sim$ 120 keV, the signal was not truncated by the DSPEC. Only decays of stored ions were considered, i.e., the peak area recorded during the background measurement was subtracted from the in-trap decay spectroscopy. The detection efficiency was extracted

Isotope	Ion bunch intensity	Blocks	PIPS ion bunch intensity
^{124m}Cs	$4.48(63) \cdot 10^3$	6+7-5-8	
^{124g}Cs	$1.34(13) \cdot 10^5$	6+7-5-8	$2.8(11) \cdot 10^5$ †
^{126}Cs	$2.65(32) \cdot 10^5$ †	7-8	$4.4(21) \cdot 10^5$ †
	$2.54(54) \cdot 10^5$	9-10	
	$1.85(46) \cdot 10^5$	11-12	
	$1.80(32) \cdot 10^5$	13-14	
	$1.61(30) \cdot 10^5$	15-16	

Table 5.4: Ion bunch intensities derived from the measured ^{124g,m,126}Cs photo peak intensities. The column on the right lists intensities determined with the monitoring PIPS assembly for comparison. The values marked with † were recorded with ~ 10 Hz repetition rate. All other measurements were performed with ~ 20 Hz.

from Penelope simulations of the experimental setup. The determined photo peak intensities are presented in Table 5.4 along with those determined with the monitoring PIPS assembly listed in Table 5.1. The ion bunch intensities of ions stored inside the trap are about half of those measured at the PIPS assembly (48(20)% and 60(30)% for ^{124,126}Cs, respectively). This was expected because the ion beam was bent twice by 45° and had to be injected into the magnetic field of the trap. The determined efficiencies agree with efficiencies of ions ejected from the EBIT to the MPET-MCP [Lap10] where the ions travel the opposite direction through the two 45° bends.

Blocks 7 and 8 were recorded with $t_{\text{storage}} = t_{\text{BGND}} = 50$ ms instead of 25 ms like all other measurements, and agree with the determined intensities of blocks 9 and 10. After these measurements, the beam was off for several hours and ^{124}Cs was measured in between. When the experiment was continued with ^{126}Cs, the ion beam intensity was reduced. However, it is noted that the ion bunch intensity of blocks 11 through 16 remained constant, independent of the applied tune.

5.4.3 Electron-capture branching ratio measurement of Cs

Considering the previously presented systematic studies, the ECBR of ^{124}Cs was determined. The measurement periods $t_{\text{storage}} = t_{\text{BGND}}$ of 25 ms and 50 ms were short compared to the half lives of ^{124,126}Cs of 30.8(5) s and 1.64(2) m, respectively. Therefore, the decay rate was considered to be constant throughout these measurement periods. The validity of this assumption is valid to a level of the order of 10^{-4} and was verified in simulations. Based on this assumption, the peak intensity of the background

measurement D^{peak}_{BGND} recorded during t_{BGND} was subtracted from the peak intensity $D^{peak}_{\mathrm{storage}}$ recorded during t_{storage}.

Based on the measured ^{124}Cs photo peaks' intensities presented in Tab. 5.3 and the ^{126}Cs peak areas, the ECBR of ^{124}Cs was calculated according to Eq.(5.7). There, I^K only depends on the ratio of intrinsic γ ray detection efficiencies $\varepsilon^{int}_{det}(E_A)/\varepsilon^{int}_{det}(E_{A'})$. This ratio was determined with the calibration source ^{133}Ba and verified in Penelope simulations. Accounting for the probability $f_{\mathrm{K}} = 0.878$ [NND10] that an EC creates a vacancy in the K-shell and considering the fluorescence yield $\omega_{\mathrm{K}} = 0.888(5)$ [Sch00], the ECBR of ^{124}Cs was calculated separately for each block of ^{126}Cs listed in Table 5.2. This was done to identify possible systematic effects. Fig. 5.21 presents the determined ECBRs for the different ^{126}Cs reference blocks along with the statistical uncertainty. Based on these values, the ECBR of ^{124}Cs was determined to be $(17.8 \pm 2.5(\mathrm{stat.}) \pm 15(\mathrm{syst.}))\%$. This value agrees with the literature value of 10(9)% [NND10]. The large systematic uncertainty arises from the truncation of high energy photon events caused by the impedance mismatch between DSPEC and preamplifier. However, the statistical uncertainty was improved by a factor of 3 compared to previous measurements.

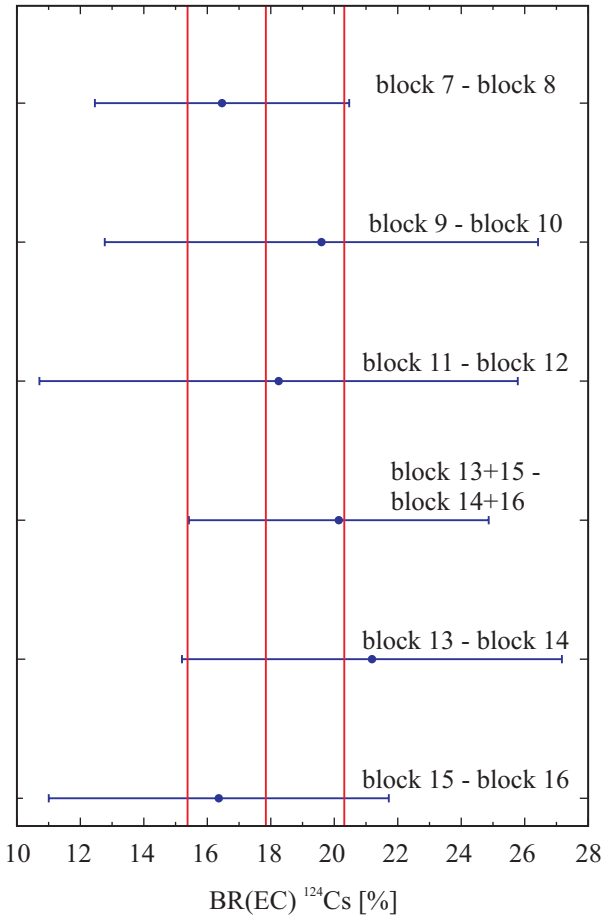

Figure 5.21: Calculated ECBRs of ^{124}Cs. This plot displays the ECBRs for each ^{124}Cs block as well as the summed blocks for different ^{126}Cs calibration files.

Chapter 6

Conclusion and Outlook

During the past years, ion traps were introduced to the field of nuclear physics with short lived radioactive ions. These traps were typically used as gas-filled Paul traps to cool and clean the ion beam or for high precision mass measurements in Penning traps. In further developments, the high resolving power of Penning traps was used to isobarically purify the sample before it was delivered to a spectroscopy setup [Kol04]. Since then, new Paul and Penning traps were designed to also perform decay spectroscopy on stored ions. At ISOLDE, a method for conversion-electron spectroscopy was developed [Wei01], and at GANIL a Paul trap with an open geometry was used to measure the decays of $^{6}He^{+}$ [Flé08]. Most recently, a new technique was developed in this work to measure ECBRs of ions stored in a Penning trap.

With TITAN-EC, a new technique was developed that allows the measurement of very weak electron capture branches. With this technique, the ECBRs of the intermediate nuclei in $\beta\beta$ decay listed in Table 1.3 will be measured during the next years. With these measurements, uncertainties on already existing values will be improved and unknown branching ratios will be measured. The measured ECBR will provide important input for theoretical calculations. In cases where a single-state dominance is present, the $2\nu\beta\beta$ transition matrix element can be determined with TITAN-EC.

In two online experiments with radioactive ^{107}In and ^{124,126}Cs the ECBRs of ^{107}In and ^{124}Cs were determined to be $(53 \pm 20)\%$ and $(17.8 \pm 2.5(\text{stat.}) \pm 15(\text{syst.}))\%$ and agree with 64(3)% and 10(9)% [NND10], respectively. These two measurements were performed using different detectors, different measurement cycles and different methods of efficiency calibration. The advantage of the Ge detector was the larger geometrical detection efficiency resulting in higher statistics. However, if isobaric contamination is present, the higher resolution of the LeGe detector allowed separation of peaks of different isotopes in the x-ray region. This dramatically helped to reduce uncertainties in the peak analysis because the peaks could be analyzed separately. The statistical uncertainty of the ECBR of ^{124}Cs is reduced by a factor of three compared to the literature value. However, due to an impedance mismatch between preamplifier and DSPEC, a systematic uncertainty of 15% had to be added.

	Ge detector	LeGe detector
ε_{geo}	$\sim 0.25\%$	$\sim 0.08\%$ @ 100 mm
Resolution at 30 keV	600 eV	300 eV
Isotope	^{107}In	^{124,126}Cs
Measurement time	69.19 min	6 h for ^{124}Cs
		12 h for ^{126}Cs
Calibration method	Relative to calibration sources	^{124}Cs relative to ^{126}Cs

Table 6.1: Physical properties of LeGe and Ge detectors used to determine the ECBRs of ^{124,126}Cs and ^{107}In, respectively.

The determined ECBR of ^{107}In was smaller than the literature value. This indicated that ion losses occurred along the beam line and in the trap that dominantly contributed to the normalization photo peak. This was verified by measuring the background while ^{126}Cs was deposited in the trap. With a modified measurement cycle, in-trap decays of ^{124,126}Cs and the background were measured in short sequences of 25 ms. This allowed determination of the number of counts that occurred while ions were stored in the trap by subtracting the measured background. Additionally, the ECBR of ^{124}Cs was determined using the measured ^{126}Cs peak intensities for efficiency calibration. The advantage of this method is that it is independent of the setup, i.e., both spectra were recorded with the same geometry and the same detector-source configuration. This procedure assumes a constant ion cloud size. Within the measurement uncertainty, this assumption is reasonable.

In both cases, ^{107}In and ^{124,126}Cs, a γ line was used to normalize the spectra and determine the total number of decays. This method is independent of the geometrical efficiency. The detection of β particles was found to be especially not suited for normalizing the spectra. Simulations showed that the amount of β particles reaching the detector varies depending on the ion cloud size. Due to the magnetic bottle and geometrical setup, the total β detection efficiency is about $\sim 20\%$ and varies depending on parameters during the experiment. The key features of both measurements are listed in Table 6.1.

The feasibility of the new technique was successfully demonstrated. Due to the strong magnetic field, β particles cannot reach the x-ray detectors providing a clear advantage compared to conventional techniques. However, these β particles are nevertheless responsible for an increased background in the photon spectrum below ~ 300 keV. In future developments it is necessary to shield the x-ray detectors. In the TITAN-EC setup this can be achieved by placing the x-ray detectors in tungsten cylinders. By

further installing tungsten cylinders inside the vacuum, one can assure that only photons originating from the trap center can reach the detector. This would significantly reduce the background in the x-ray detector.

In an in-trap decay spectroscopy experiment, ions are stored backing free in the trap. During the measurement of ^{126}Cs, two different ion optic settings were used. The amount of ions lost in the trap was different for each setting. However, the settings that resulted in greater losses in ^{126}Cs did not result in any losses in ^{124}Cs. The injected ion bunch intensities were comparable. The influence of injection and extraction parameters on the storage efficiency needs to be investigated in further online experiments with radioactive ions. Systematic studies with ion bunch intensities of $\sim 10^5$ ions cannot be performed precisely otherwise.

The extraction of ions from the spectroscopy trap onto the MPET-PIPS assembly during the ^{124,126}Cs experiment proved to be a powerful tool to monitor the experiment. If the ion intensity changes, the β count rate also changes and thus provides a direct feed back on the number of injected radioactive ions.

In order to measure ECBRs of the order of 10^{-5}, the setup needs further improvement. Seven Si(Li) detectors[1] are planned to be installed at all available access ports of the trap. This will increase the geometric acceptance to ∼2.5%. As a comparison, the geometric acceptance of the Ge and LeGe detectors used in this work were about $\sim 0.25\%$ and $\sim 0.08\%$, respectively. The total detection efficiency for photon energies present in the decay of ^{100}Tc was simulated with Penelope and is presented in Table E.2 and Table E.3 for one and seven Si(Li) detectors, respectively. Applying a cycle with $t_{\mathrm{storage}} = 50\,\mathrm{ms}$ and $t_{\mathrm{BGND}} = 10\,\mathrm{ms}$, and an ion bunch intensity of $1 \cdot 10^5$ ions, the number of in-trap decays computes to $N(1\,\mathrm{h}) = 1.15 \cdot 10^7$ applying Eq.(5.13). As a comparison, applying the cycle used for ^{124,126}Cs with $t_{\mathrm{storage}} = t_{\mathrm{BGND}} = 25\,\mathrm{ms}$, one calculates $N(1\,\mathrm{h}) = 6.7 \cdot 10^6$. Based on the expected number of decays, the photo peak intensities $I_{photopeak}$ [NND10], and the simulated total efficiencies from Table E.3, the expected counts were calculated and are presented in Table 6.2. Based on these numbers, the ECBR of ^{100}Tc can be deduced with an uncertainty of 10%-15% after $\sim$ 86 hours. However, in this detector configuration the detection efficiency at the calibration line of 539.52 keV is the limiting factor. If one of the Si(Li) detectors were replaced by a detector with similar diameter but thicker crystal, the detection efficiency of higher energetic photons would be increased dramatically. Alternatively, a stacked ZnCdTe-Ge detector setup could be installed with the ZnCdTe detector placed at an access port inside the vacuum. The Ge detector would then be placed behind it at the same access port but outside the vacuum vessel. X-ray photons would be detected with high efficiency by the ZnCdTe detector while the Ge detector would detect higher energetic photons with high efficiency.

[1] Canberra, ⌀ 50 mm, 2 mm thick

Origin	Energy [keV]	Counts per hour	σ
Mo K_{α_2}	17.374	0.68	0.48
Mo K_{α_1}	17.479	1.20	1.00
Mo K_{β_3}	19.59	0.09	0.08
Mo K_{β_1}	19.698	0.19	0.13
Mo K_{β_2}	19.965	0.04	0.03
^{92}Tc	85.0	591.7	39.4
^{92}Tc	148.0	601.9	35.8
^{92}Tc	329.3	60.8	4.4
^{100}Tc	539.52	1.17	0.07
^{92}Tc	773.0	6.31	1.38
^{94}Tc	871.05	5.70	0.61

Table 6.2: Expected number of detected ^{100}Tc decay events. Additionally, expected γ events were determined that are suited for efficiency calibration. These numbers were derived assuming $1 \cdot 10^5$ ions/bunch and using simulated efficiencies from Table E.3.

Independent of the detector setup, the efficiency of the detectors has to be calibrated, ideally with all detectors already installed at the experiment. The efficiency can be calibrated performing in-trap decay spectroscopy on isotopes with well known x-ray and γ intensities. In the case of ^{100}Tc, the isotope ^{92}Tc ($t_{1/2} = 4.25(15)$ min) is suited since the half life is short.

The cooler Penning trap (CPET) is currently being constructed. If the current design is modified, this trap can be used in future experiments for isobaric purification. One could imagine cycles where ECBRs are measured in the spectroscopy Penning trap while ions are accumulated and cleaned in the CPET. Then, the spectroscopy trap is emptied and a fresh and isobarically purified bunch is injected from the CPET for in-trap decay spectroscopy. This method would eliminate isobaric contaminates and further improve the ECBR measurement.

Appendix A

Ge Detector

The resolution of the Ge detector at several photo-peak energies was determined by recording spectra with the DSPEC. The determined values are listed in Table A.1. Fig. A.1 displays the FWHM of the Ge detector at various energies. Typically, the Ge

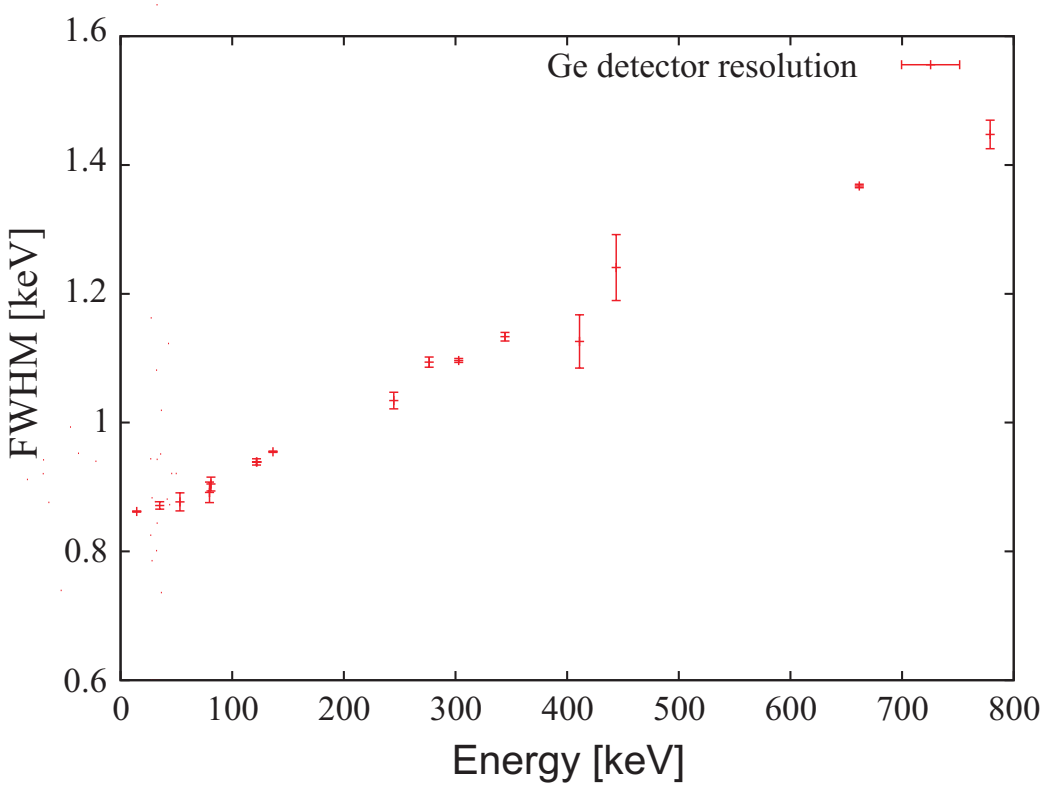

Figure A.1: Photo peak resolution of the Ge detector.

Position [keV]	PosErr [keV]	FWHM [keV]	FWHM error [keV]
14.246	0.015	0.887	0.009
122.059	0.002	0.984	0.001
136.485	0.002	0.978	0.006
1173.285	0.002	1.706	0.004
1332.522	0.002	1.796	0.005

Table A.1: FWHM of the Ge detector at different energies (^{60}Co and ^{57}Co) achieved using the DSPEC and fitted with Radware [Rad].

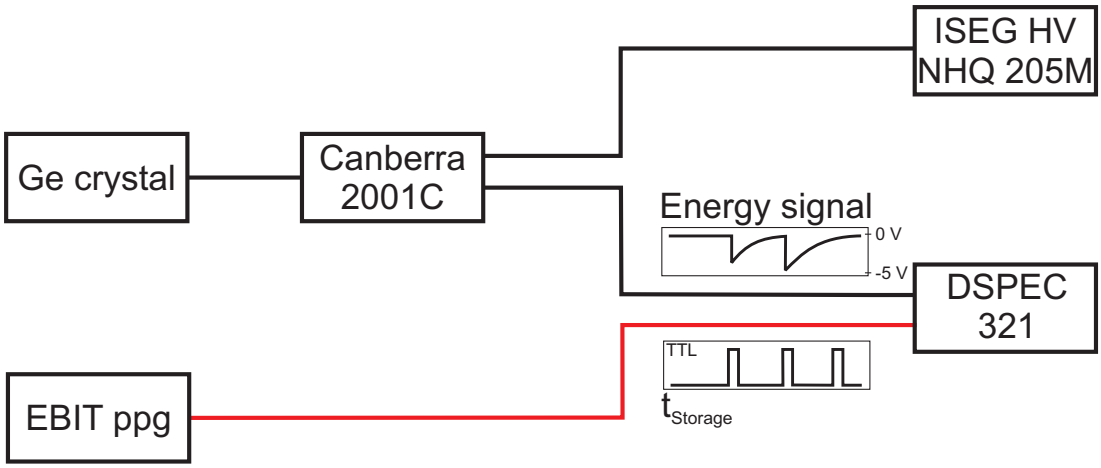

Figure A.2: Schematic of the DAQ setup of the Ge detector in combination with the DSPEC 321.

detector was read out with the DSPEC 321 in the setup illustrated in Fig. A.2. During the measurement of ^{124,126}Cs this DSPEC was used to record background spectra with the LeGe detector after ions were ejected from the trap. Meanwhile, the Ge detector signal was sampled and recorded by the tig10. The tig10 was gated such that it would only record data while ions were stored in the trap. The schematic of this setup is displayed in Fig. A.3.

Photons originating from the trap center need to penetrate two Be windows with a total thickness of 525 µm. The energy dependent transmission through these Be windows is displayed in Fig. A.4.

Fig. A.5 displays the efficiency curve of the Ge detector. It was determined with ^{142}Eu, ^{133}Ba and ^{137}Cs sources.

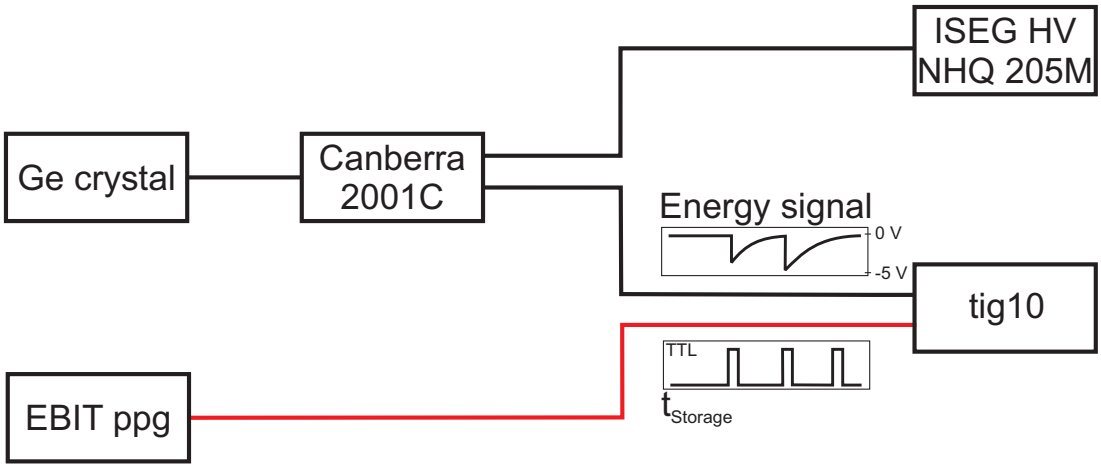

Figure A.3: Schematic of the DAQ setup of the Ge detector with the tig10.

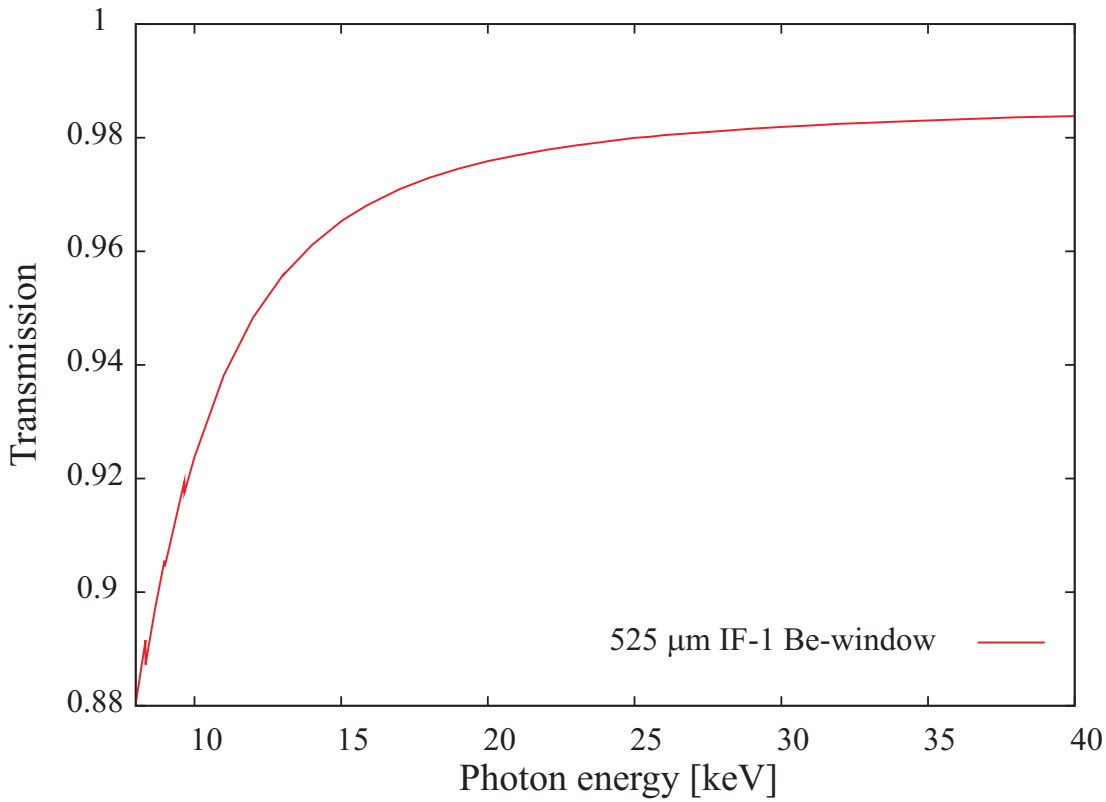

Figure A.4: Photon transmission through 525 µm a type IF-1 beryllium window calculated with mass attenuation coefficients determined by XCOM [Ber09].

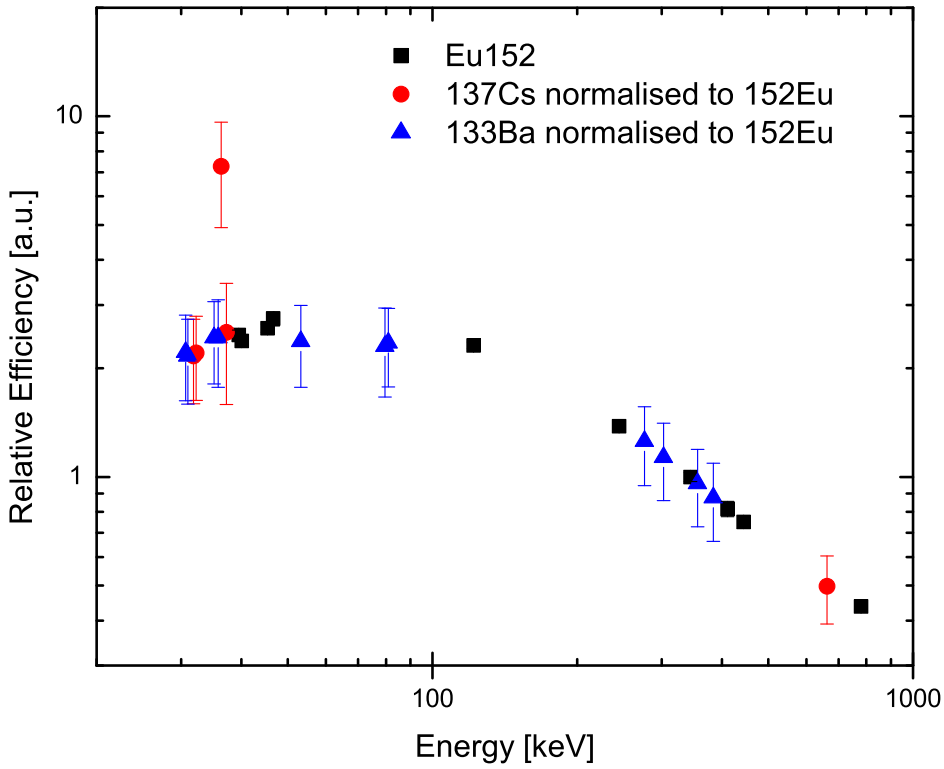

Figure A.5: Energy dependent intrinsic detection efficiency of the Ge detector. This curve was determined with the sources ^{142}Eu, ^{133}Ba and ^{137}Cs.

Appendix B

LeGe Detector

B.1 LeGe detection system

With a dead layer of 0.3 µm and a Be window of 25 µm [Canc], the low energy Ge detector (LeGe) was specifically designed to detect low energy x-ray photons down to about 1 keV. Its pre-amplifier is a Transistor-Reset-Preamplifier (TRP) that outputs a slowly rising signal that is reset to 0 V when it reaches ~ 5 V. If no energy is deposited in the Ge-crystal the signal is reset every ~ 5 s [Cana]. When photons deposit energy in the Ge-crystal the created charge is collected and a voltage step proportional to the charge is put out by the pre-amplifier. This voltage step is superimposed on top of the TRP's rising output signal and therefore, the reset rate increases with increasing photon rate. During the reset, the signal to the data acquisition has to be blocked by a TTL signal as illustrated in Fig. B.1. Otherwise, the reset pule would be recorded as well.

The Ortec DSPEC 319 was typically used to digitize the energy output signal of the LeGe detector. This unit internally deconvoluted wave forms and digitally calculated

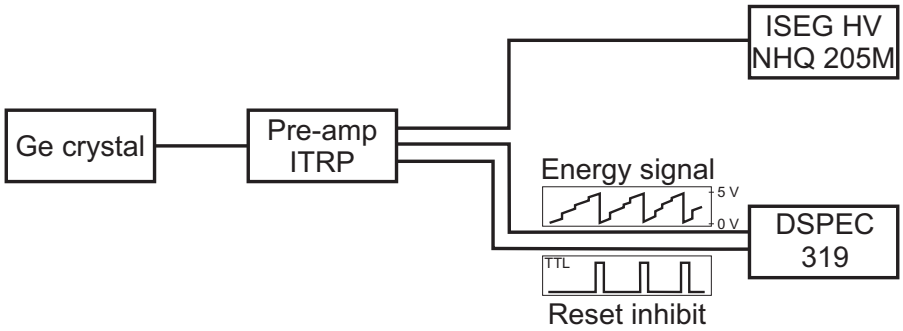

Figure B.1: Data acquisition setup that was typically used to digitize LeGe detector signals. A schematic of the Transistor-Reset-Preamplifier (TRP) energy output signal is shown as well as the corresponding TTL reset inhibit signal.

Coarse gain	2
Fine gain	0.725
Shaping time	4 µs

Table B.1: Typical settings of the DSPEC digitizing LeGe-energy signals.

the energy of each pulse. This energy information is then stored in a histogram of up to 16384 channels and was read out and saved with a computer via the software Maestro. Latter software also allows to calibrate and analyze recorded spectra. Maestro was mainly used to record and save spectra and to define the DSPEC settings. Usually the recorded spectra were analyzed using one of the programs described in Section 3.5. During the ^{107}In and ^{124,126}Cs beam times and for most systematic studies the DSPEC settings used to digitize the LeGe detector are listed in Table B.1. The relative detection efficiency was determined using radioactive sources and is displayed in Fig. B.2.

B.2 LeGe detector resolution

To determine the resolution of the LeGe detector a ^{133}Ba source was used. The spectrum was fitted in Origin with a Gaussian and a step function and the results are listed in Table B.2.

B.3 DAQ with the split LeGe detector signal

In order to record data while ions were stored inside the trap and right after the trap was emptied, the signal of the LeGe detector was split up and fed to DSPEC 319 and 321 (see Fig. B.3). In order to verify that both DSPEC would record data with the same efficiency ^{133}Ba spectra were recorded with this setup. The results are presented in Table B.3 and explained in more detail in Section 5.4.1.

Position [keV]		**FWHM [keV]**	
6.700	±0.003	0.162	±0.006
14.711	±0.003	0.208	±0.006
25.359	±0.003	0.282	±0.006
35.231	±0.000	0.314	±0.001
36.098	±0.001	0.334	±0.002
53.415	±0.001	0.358	±0.002
79.860	±0.005	0.441	±0.003
81.237	±0.000	0.450	±0.001
122.294	±0.002	0.579	±0.003
136.697	±0.011	0.615	±0.016
160.826	±0.012	0.685	±0.017
276.564	±0.003	1.001	±0.006
302.984	±0.030	1.049	±0.020
356.127	±0.030	1.123	±0.020

Table B.2: FWHM of the LeGe detector at different energies (^{133}Ba and ^{57}Co) achieved with the DSPEC and fitted with Origin.

Peak	A_{319}	A_{321}	R	A_{319}^{gated}	A_{321}^{gated}	R^{gated}
30.6 keV*	7717(94)	7690(94)	1.003(17)	1480(41)	1489(41)	0.994(39)
33 keV†	339(18)	340(18)	0.997(76)			
34.6 keV†	1490(39)	1489(39)	1.001(37)			
35.8 keV†	405(20)	411(20	0.985(69)			
36.2 keV†	2211(47)	2210(47)	1.000(30)			
79.6 keV*	254(18)	254(18)	0.997(100)			
81.0 keV*	3291(58)	3291(58)	1.000(25)	552(25)	558(25)	0.989(63)

Table B.3: ^{133}Ba photo peak areas A_{319} and A_{321} of spectra recorded with DSPEC 319 and DSPEC 321. R is the ratio A_{319}/A_{321}. Listed are the values for non-gated and gated data acquisition. Values marked with (*) were fitted using [Sju09] while values marked with (†) are the total integral over the peak region.

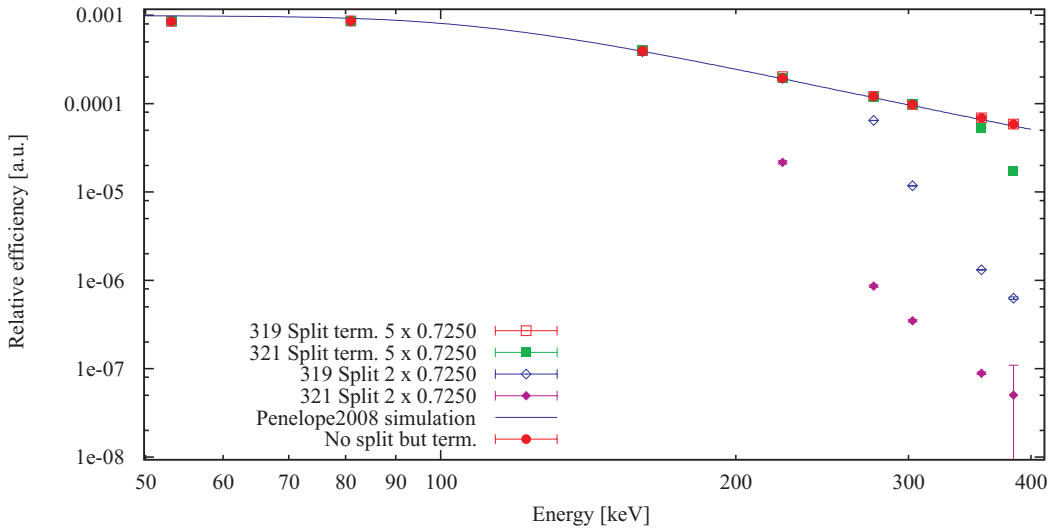

Figure B.2: LeGe detector efficiency above 50 keV determined with ^{133}Ba source. Displayed are relative detection efficiencies recorded with different DSPEC settings. Only if the LeGe preamp signal is terminated the efficiency can be reproduced by Penelope2008 simulations.

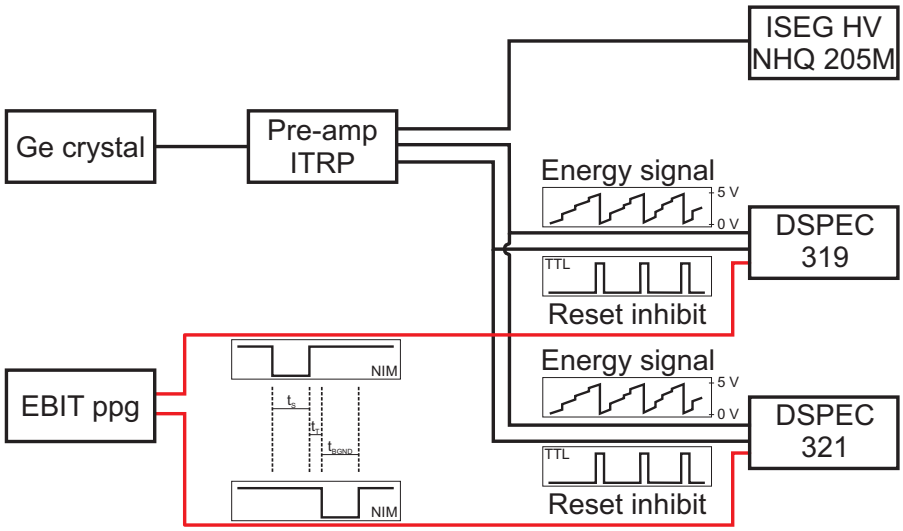

Figure B.3: Schematic of the data acquisition setup during the ECBR measurement of ^{124,126}Cs. While ions were stored inside the trap the DSPEC 319 was recording spectra. After the ions were extracted the DSPEC 321 was gated to take spectra of the background.

Appendix C

Passivated Implanted Planar Silicon Detector

In order to detect electrons originating from β decays happening in the Penning trap a beta detector was developed to be installed at the trap exit. This detector has to cover as much solid angle as possible while still fitting into the detection chamber described in Section 3.1.5. Based on SIMION simulations (see Section 3.3.1) a Canberra PIPS detector with an active area of 600 mm^2 has been purchased. The physical dimensions of the detector are listed in Tab. C.1.

Fig. C.1 displays the scheme of the DAQ that was used to determine the half lives of several isotopes. This setup was used with the PIPS-300 assembly in front of the

Nominal active area	600 mm^2
∅ nominal active area	27.6 mm
Total junction area	693 mm^2
∅ total junction area	29.7 mm
Thickness	500 µm
Capacitance	145 nF
Active area thin window	603 mm^2
∅ active area thin window	27.7 mm
Al coating ring $\varnothing_{in}$	27.8 mm
Al coating ring $\varnothing_{out}$	29.6 mm
Bias	-100 V
Leakage current	6 nA

Table C.1: Physical dimensions of the PIPS-600.

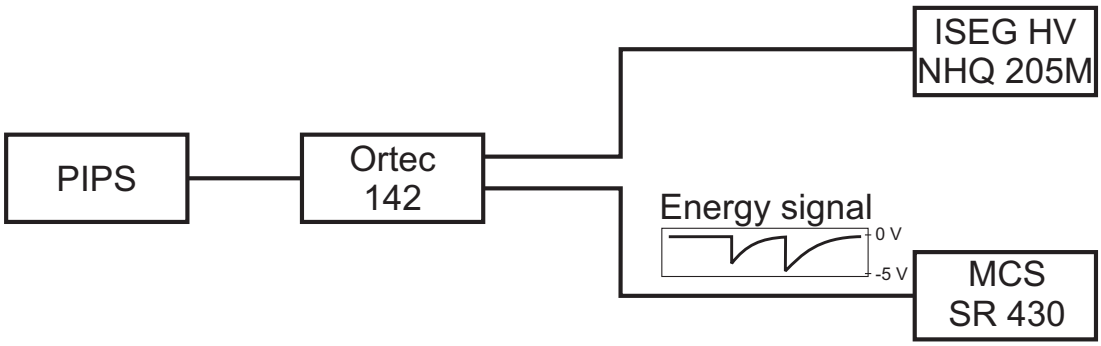

Figure C.1: Scheme of the SR430 DAQ setup used to record β decay data with a PIPS detector.

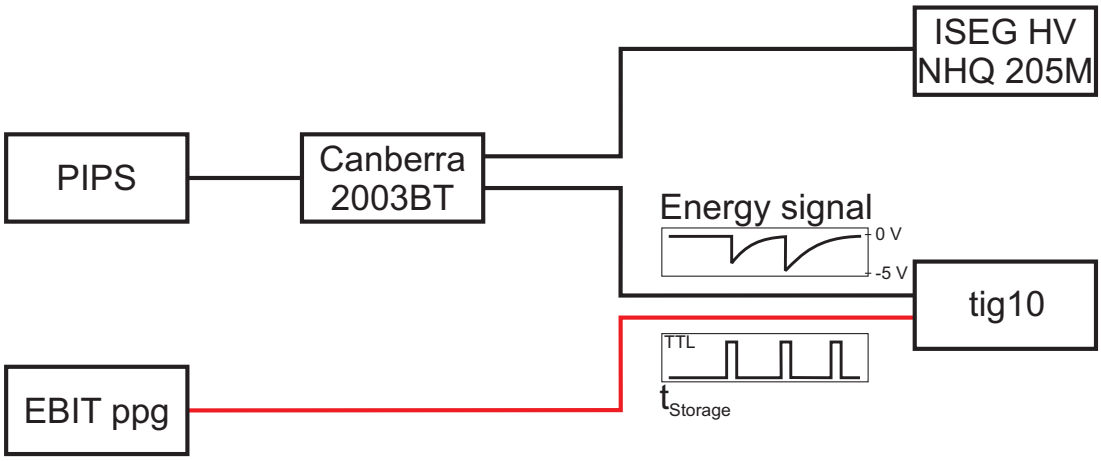

Figure C.2: Schematic of the tig10 DAQ setup to record β events during the ^{124,126}Cs experiment. The DAQ was gated with a signal from the EBIT to only record data during t_{storage}.

MPET as well as with the PIPS detector assembly after the EBIT. The β^+ signals during the ^{124,126}Cs measurement were recorded with the tig10. The schematic of this setup is shown in Fig. C.2.

Appendix D

Beta Detector Connector

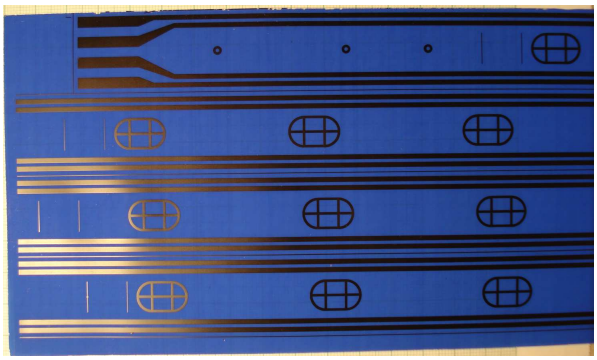

Figure D.1: This picture shows the circuit of the beta detector connection printed on the transfer sheet. The oval shapes are marks to later cut out holes in the circuit board. These holes then enable you to feed the circuit board onto the rod of the feed through.

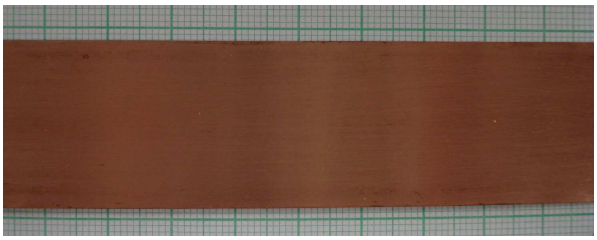

Figure D.2: A 1 inch wide strip is cut off the flexible circuit board. Onto this strip the printed circuit shown in Fig. D.1 will be transfered with an iron.

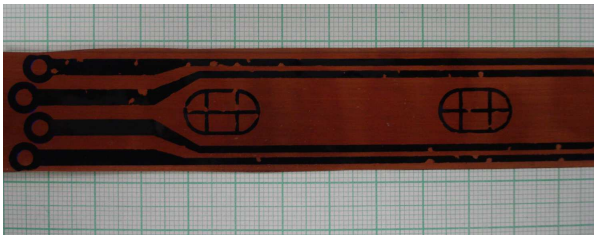

Figure D.3: After ironing the printed circuit onto the copper the transfer sheet is removed and leaves the laser-printer inc on the copper. Defects have to be covered with a protective layer afterwards with a circuit board drawing pen. After this step non-covered copper is etched off in an Iron(III) chloride-solution.

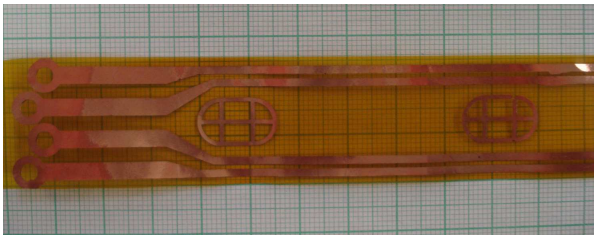

Figure D.4: After etching the circuit board is rinsed with water and afterwards residual ink is removed. This picture shows the side that will be connected on the detector side.

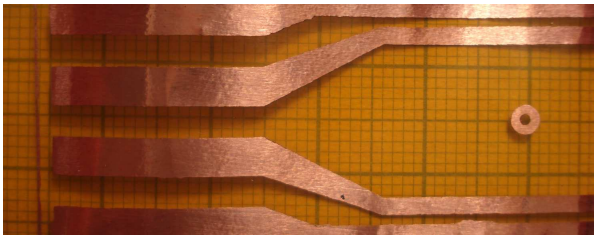

Figure D.5: This picture displays the end where Teflon-insulated wires are soldered to in order to connect the circuit board to the electrical-feed through.

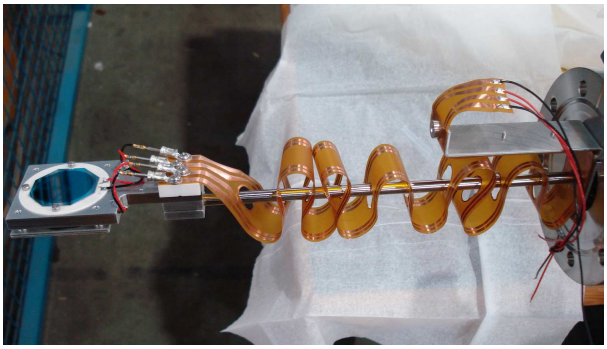

Figure D.6: PIPS-600-CB mounted on its holder and connected with the flexible circuit board. At the end leading to the electrical feed through wires are soldered to the circuit board.

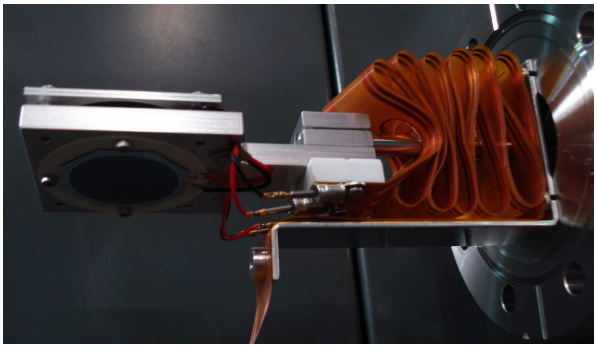

Figure D.7: The beta detector in the retracted position. It is cleaned and ready to be installed inside the UHV system.

Appendix E

Simulations

E.1 Penelope simulation

The TITAN-EC setup was created in Penelope2008 [Sal08] to simulate detection efficiencies and investigate effects of ion losses inside the trap on x-ray and γ ray spectra. Included in the simulation were the eight-fold segmented central drift tube, both guard electrodes, and the Helmholtz coils as well as their holding structure. Two detectors were included in the simulation. The LeGe detector was located at a distance of 100 mm from the trap center including a 25 µm Be window, a 0.5 µm thick front dead layer, and 0.5 mm thick dead layers at the side and the back of the crystal [Canc]. The front window thickness was chosen 0.2 µm thicker than quoted by Canberra to be conservative and account for possible contamination frozen to the surface. The Si(Li) detector was modeled according to the dimensions provided in [Canb] assuming a dead layer similar to that of the LeGe detector. Within the simulations, the Si(Li) detector was considered to consist only of Si. In front of the Si(Li) detector a C window (0.8 mm), the vacuum Be window (500 µm), and the Be window at the thermal shield (25 µm) including an Al mounting frame were placed. Detector and window locations are displayed in Fig. E.1.

In each simulation a defined number of mono-energetic photons with E_0 was emitted as defined by an input file. The simulation calculated the energy transport of each photon and put out the energy deposited in the detector body by each photon. To determine the detection efficiency, this output was then analyzed counting all photons that deposited energy in the interval $[E_0 - \Delta E, E_0]$ with ΔE being the FWHM as defined by the Fano factor in Eq.(3.3). This number was then used to determine the detection efficiency at that particular energy. In Penelope2008 simulations the following points were investigated.

- The intrinsic LeGe detection efficiency ε_{int},
- The total LeGe detection efficiency $\varepsilon_{\text{total}}$ for energies occurring in the decay of ^{124,126}Cs. The simulated efficiencies are listed in Table E.1.

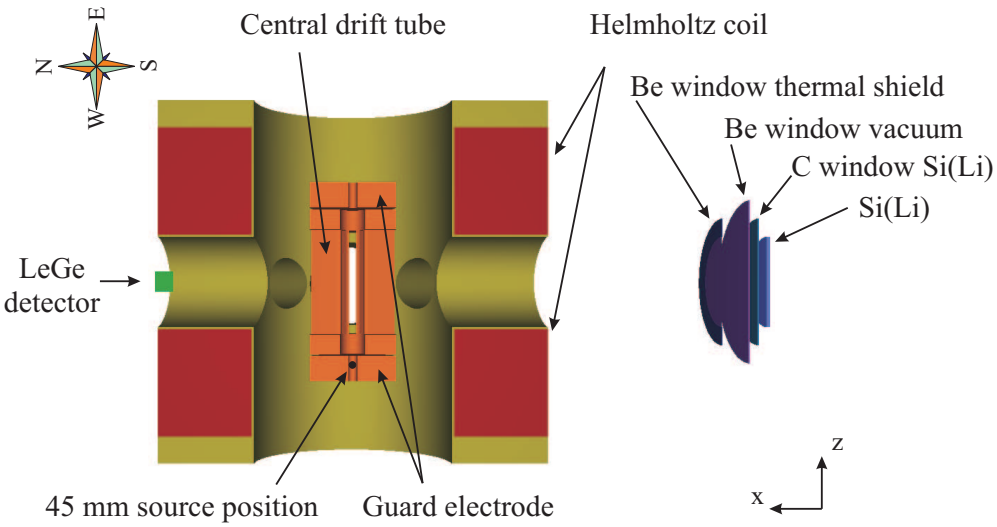

Figure E.1: Penelope geometry of the spectroscopy trap including the LeGe detector as well as a Si(Li) detector.

- total Si(Li) detection efficiency $\varepsilon_{\text{total}}$ for energies occurring in the decay of ^{94,100}Tc. They are listed in Table E.2.
- The possibility to detect photons from ions lost at the guard electrode during injection and extraction. In this simulation, a point source was placed along the beam axis 45 mm away from the trap center. Its position is indicated in Fig. E.1. A collimated beam of photons was emitted towards the LeGe detector. Low energetic photons were absorbed by the surrounding material while some of the higher energetic photons were detected by the LeGe detector. The fraction of detected photons is presented in Table E.4 for several photon energies.

E.2 Radial β-loss simulations

SimIon [Dah00] was used to simulate the behavior of electrons and positrons that were emitted of ions stored in the trap. These simulations focused on the ability of the magnetic field to confine fast electrons with an end-point energy of up to 7 MeV kinetic energy. In these simulations, positrons were created within a three dimensional Gaussian distribution of the size $\sigma_z = 2.5$ mm, $\sigma_x = \sigma_y = 0.25$ mm and emitted isotropically. The positron's kinetic energy was defined using a modified code from [Sju10] calculating

Origin	Energy [keV]	$\varepsilon_{\text{total}}$ [%]	$\sigma\varepsilon_{\text{total}}$ [%]
Xe K_{α_2}	29.458	0.0560010	0.0000413
Xe K_{α_1}	29.779	0.0559931	0.0000413
Cs K_{α_2}	30.625	0.0559301	0.0000413
Cs K_{α_1}	30.972	0.0559914	0.0000413
Xe K_{β_1}	33.624	0.0556956	0.0000412
Xe K_{β_2}	34.415	0.0555656	0.0000411
Cs K_{β_1}	34.987	0.0554762	0.0000411
Cs K_{β_2}	35.822	0.0553179	0.0000410
^{124m}Cs	58.20	0.0373275	0.0000337
^{124m}Cs	96.55	0.0128252	0.0000198
^{124m}Cs	188.98	0.0022808	0.0000083
^{124m}Cs	211.64	0.0017030	0.0000072
^{124g}Cs	354.01	0.0004750	0.0000038
^{126}Cs	388.66	0.0003903	0.0000034

Table E.1: Simulated total detection efficiency $\varepsilon_{\text{total}}$ of the LeGe detector in the TITAN-EC setup for energies present in the decay of ^{124,126}Cs.

Origin	Energy [keV]	$\varepsilon_{\text{total}}$ [%]	$\sigma\varepsilon_{\text{total}}$ [%]
Mo K_{α_2}	17.374	0.2494729	0.0001525
Mo K_{α_1}	17.470	0.2488035	0.0001523
Mo K_{β_3}	19.590	0.2342756	0.0001477
Mo K_{β_1}	19.608	0.2334180	0.0001475
Mo K_{β_2}	19.965	0.2307700	0.0001466
^{92}Tc	85.0	0.0060659	0.0000475
^{92}Tc	148.0	0.0010517	0.0000198
^{92}Tc	329.3	0.0000943	0.0000059
^{100}Tc	539.52	0.0000219	0.0000014
^{92}Tc	773.0	0.0000078	0.0000017
^{94}Tc	871.05	0.0000075	0.0000008

Table E.2: Simulated total detection efficiency $\varepsilon_{\text{total}}$ of one Si(Li) detector in the TITAN-EC setup for energies occurring in the decay of ^{92,94,100}Tc energies.

Origin	Energy [keV]	$\varepsilon_{\text{total}}^{7Si(Li)}$ [%]	$\sigma\varepsilon_{\text{total}}^{7Si(Li)}$ [%]
Mo K_{α_2}	17.374	1.75	0.01
Mo K_{α_1}	17.479	1.74	0.01
Mo K_{β_3}	19.59	1.64	0.01
Mo K_{β_1}	19.698	1.63	0.01
Mo K_{β_2}	19.965	1.62	0.01
^{92}Tc	85.0	$4.25 \cdot 10^{-2}$	$0.03 \cdot 10^{-2}$
^{92}Tc	148.0	$7.36 \cdot 10^{-3}$	$0.14 \cdot 10^{-3}$
^{92}Tc	329.3	$6.60 \cdot 10^{-4}$	$0.42 \cdot 10^{-4}$
^{100}Tc	539.52	$1.53 \cdot 10^{-4}$	$0.10 \cdot 10^{-4}$
^{92}Tc	773.0	$5.48 \cdot 10^{-5}$	$1.20 \cdot 10^{-5}$
^{94}Tc	871.05	$5.22 \cdot 10^{-5}$	$0.58 \cdot 10^{-5}$

Table E.3: Simulated total detection efficiency $\varepsilon_{\text{total}}$ of seven Si(Li) detectors in the TITAN-EC setup at energies present in the decays of ^{92,94,100}Tc. The variations in the uncertainty are due to different numbers of initial photons.

the β distribution according to Eq.(3.2) but including Coulomb corrections. Positron distributions were simulated for end-point energies from 3 to 7 MeV and the number of positrons hitting the radial wall of the central drift tube was recorded. Fig. E.2 displays the resulting fraction. Positrons emitted with an end-point energy below ~ 4 MeV are confined by the 5 T magnetic field. For β^+ distributions with a higher end-point energy the magnetic field cannot confine all positrons anymore. The increased fraction at ~ 4.8 MeV is due to smaller time-steps within the simulation. These simulations show a general behavior of fast positrons in the magnetic field of the spectroscopy trap but due to a limited time-step width the simulations are not accurate anymore for high energetic positrons and electrons.

Origin	Energy [keV]	Detected [%]	σ(detected) [%]
Xe K_{α_2}	29.458	0	0
Xe K_{α_1}	29.779	0	0
Cs K_{α_2}	30.625	0	0
Cs K_{α_1}	30.972	0	0
Xe K_{β_1}	33.624	0	0
Xe K_{β_2}	34.415	0	0
Cs K_{β_1}	34.987	0	0
Cs K_{β_2}	35.822	0	0
^{124m}Cs	58.20	0	0
^{124m}Cs	96.55	0.00295	0.00027
^{124m}Cs	188.98	0.21735	0.00233
^{124m}Cs	211.64	0.23000	0.00240
^{124g}Cs	354.01	0.15335	0.00196
^{126}Cs	388.66	0.05228	0.00114

Table E.4: Fraction of photons detected by the LeGe detector that were emitted by a source placed along the trap axis at a distance of 45 mm from the trap center. Included in the fraction is the intrinsic detection efficiency $\varepsilon_{\text{intrinsic}}$ of the LeGe detector. In this simulation the photons were emitted in a collimated beam aiming at the center of the LeGe detector to save computational time. Therefore, the numbers presented are of qualitative nature but not of quantitative one.

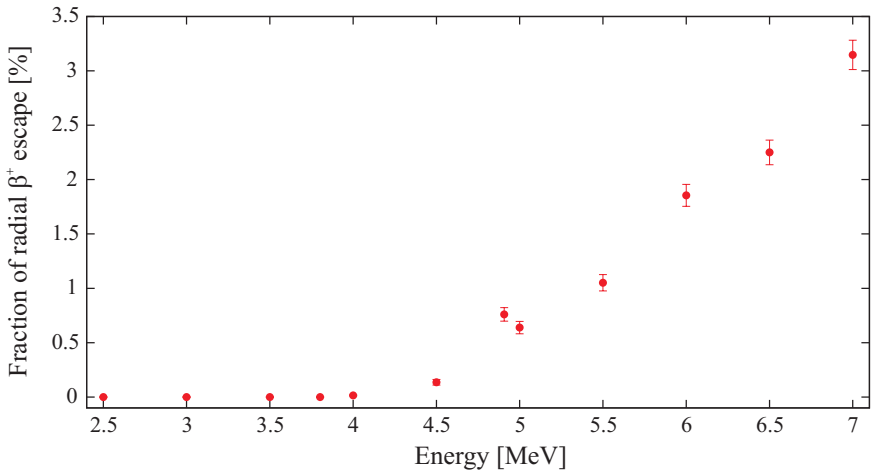

Figure E.2: Energy dependent fraction of radial β^+losses. Plotted is the fraction of positrons that could not be confined radially by the 5 T magnetic field and thus hit the wall of the central drift tube.

Appendix F

Drawings

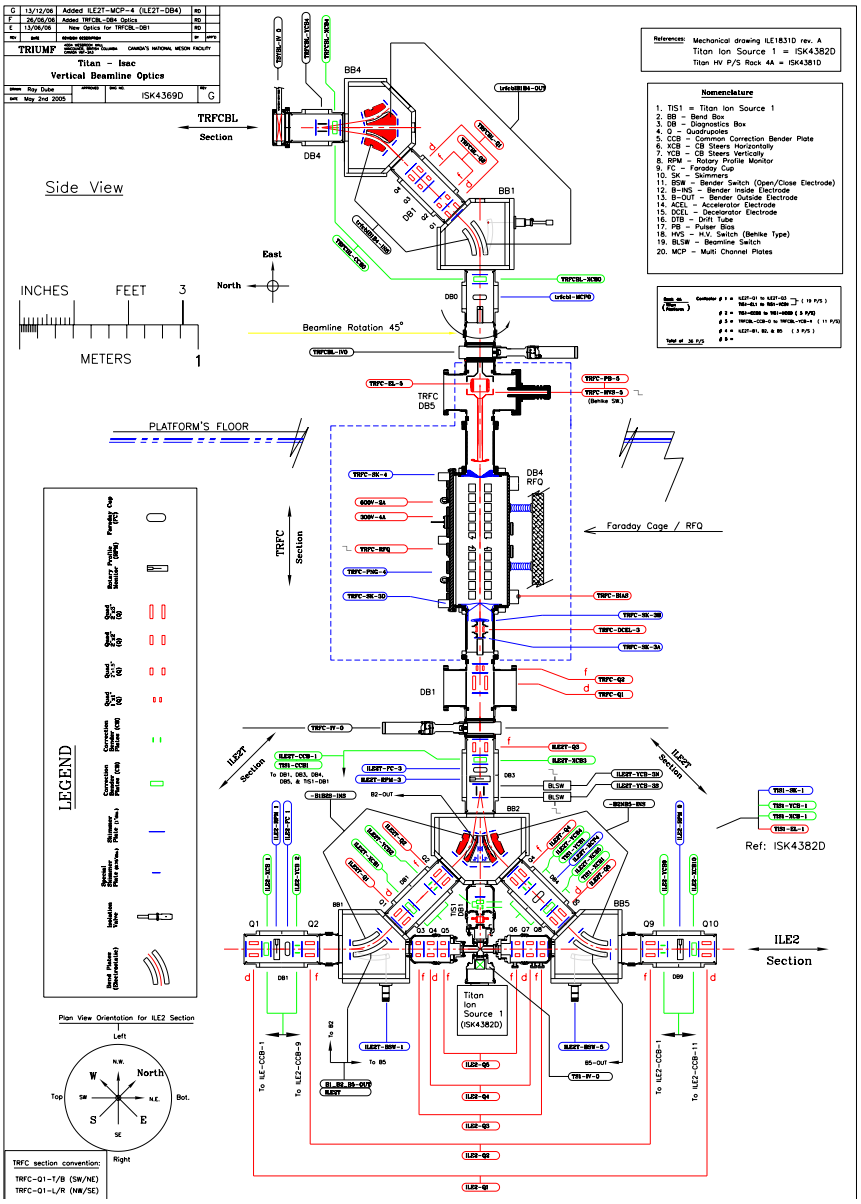

Figure F.1: **RFQ** - Schematic drawing of TITAN's RFQ and the associated beam line. Beam delivered from ISAC or OLIS enters the system horizontally from the left. TITAN's off-line ion source is mounted right below the RFQ and allows to vertically inject stable alkali ions into the ion cooler and buncher. This off-line ion source is typically used for systematic tests.

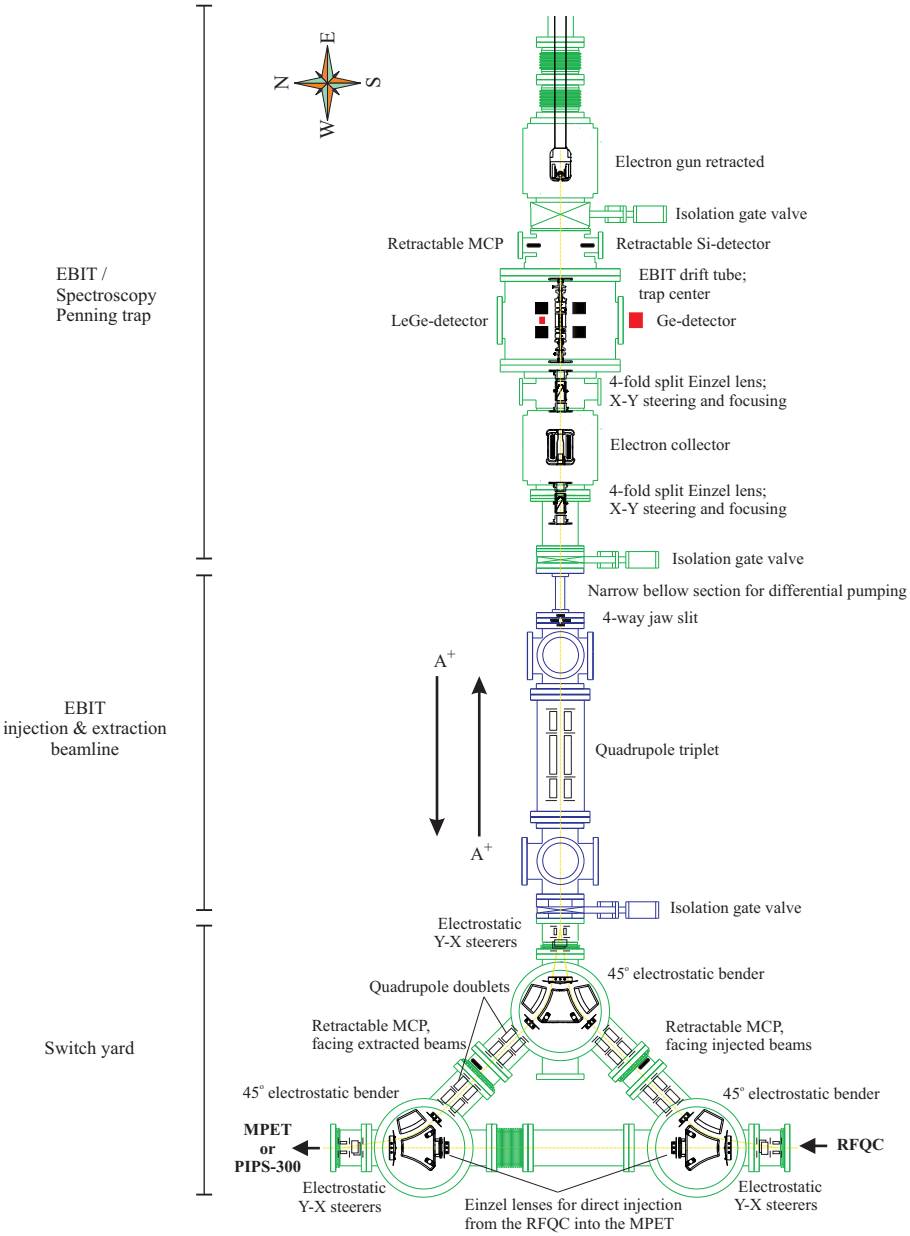

Figure F.2: **EBIT/Spectroscopy Penning trap** - Schematic drawing of the TITAN EBIT and connecting beam line. The beam is delivered from the RFQ at the bottom right. Ion-bunches can either be delivered directly to the MPET (straight) or to the EBIT/spectroscopy Penning trap (up). In the schematic the electron gun is at its retracted position. Also indicated are the positions of LeGe, Si and Ge-detector as well as the MCP.

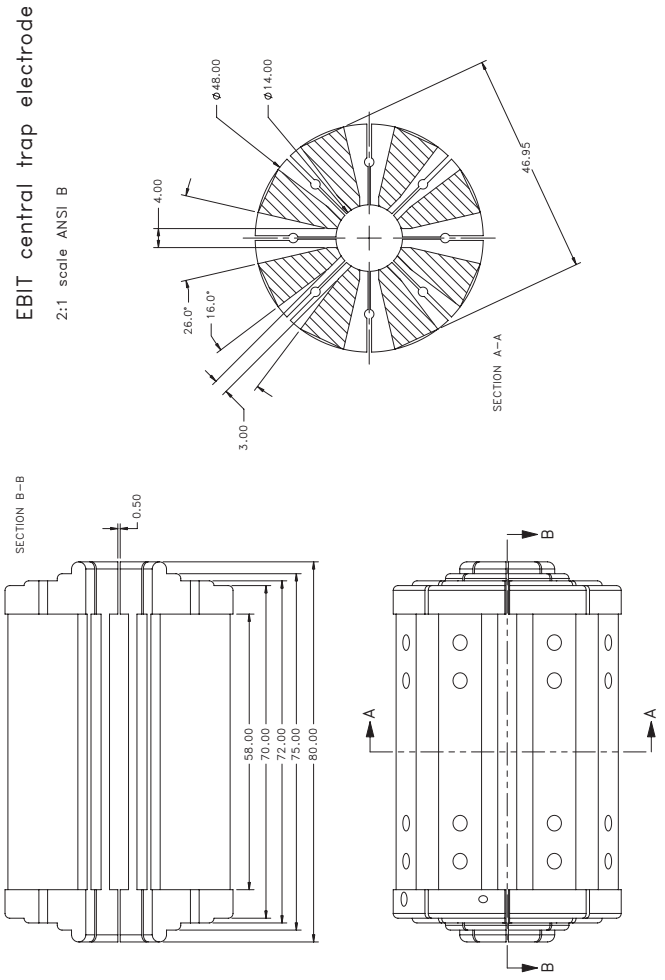

Figure F.3: Geometry and dimension of the central drift tube. The clearances at 0°, 90°, 180° and 270° have an opening angle of 26° whereas the others only have 16°.

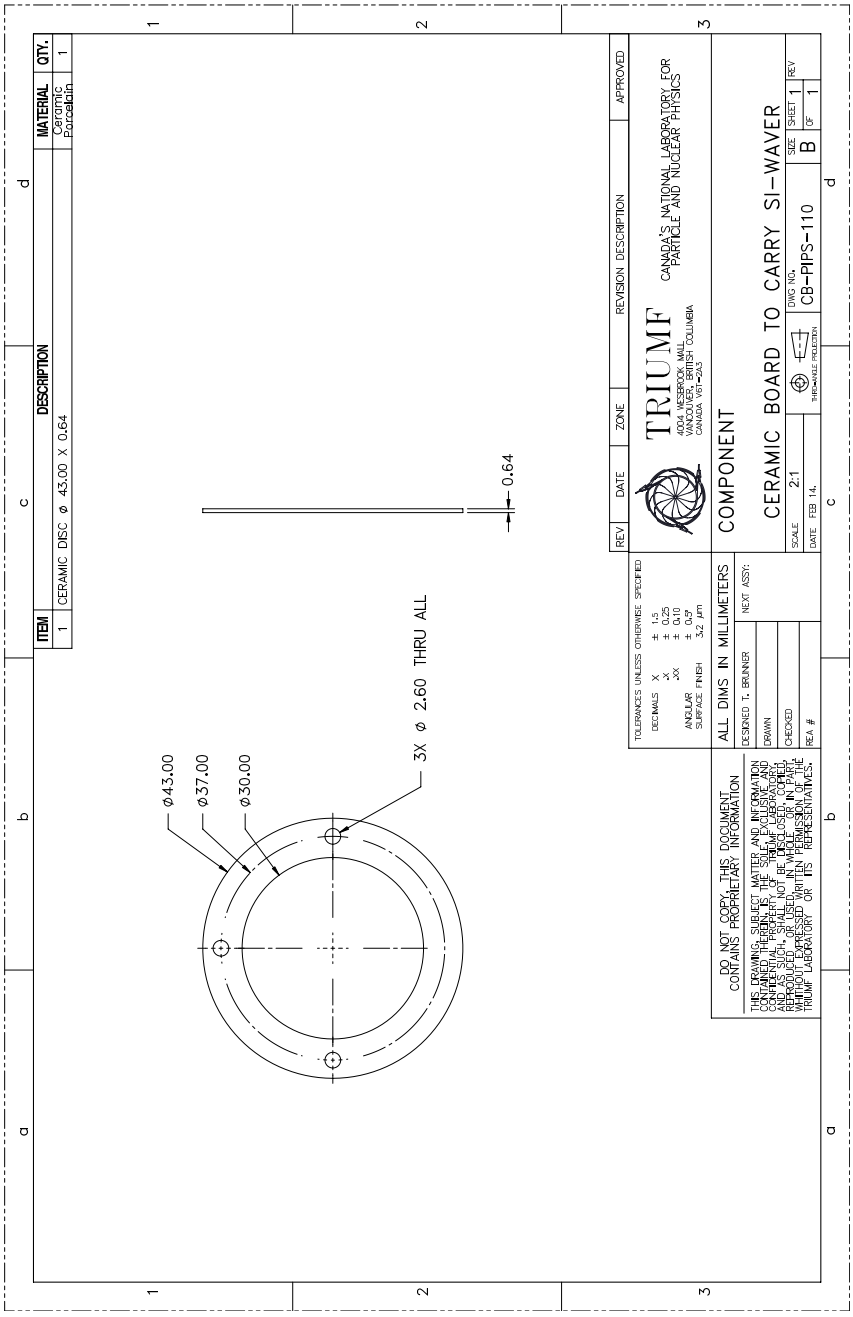

Figure F.4: Drawing of the ceramic carrier board for a 600 mm^2 PIPS detector.

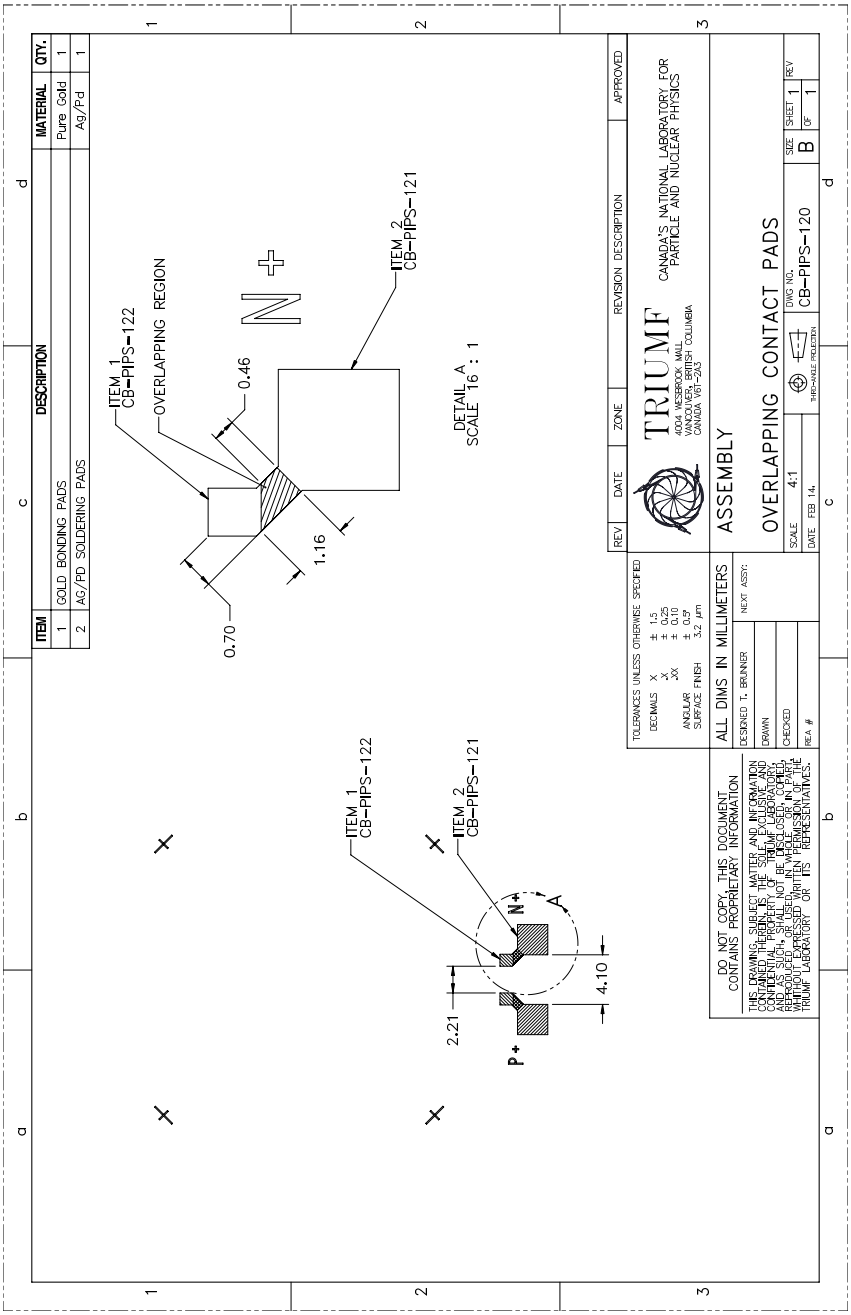

Figure F.5: Drawing of contacts for a 600 mm^2 PIPS detector.

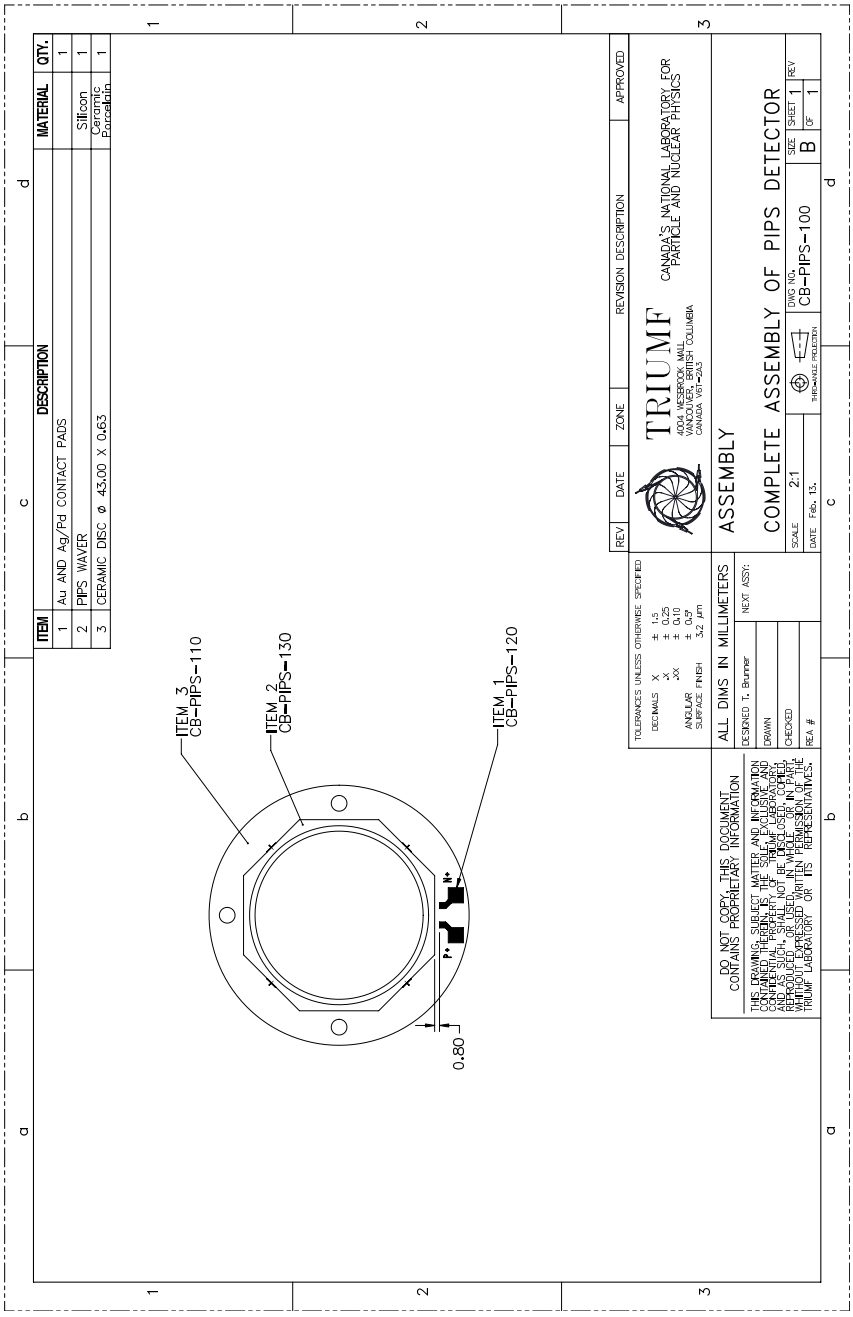

Figure F.6: Drawing of the 600 mm^2 PIPS detector.

Bibliography

[Aba84] J. Abad, A. Morales, R. Nunez-Lagos, and A. Pacheco. *Ann. Fis. A*, **80**, 9 (1984).

[Abe08] S. Abe, T. Ebihara, S. Enomoto, *et al.* Precision Measurement of Neutrino Oscillation Parameters with KamLAND. *Physical Review Letters*, **100**, 221803 (2008).

[Abt04] I. Abt, M. Altmann, A. Bakalyarov, *et al.* A New ^{76}Ge Double Beta Decay Experiment at LNGS. *arXiv:hep-ex/0404039v1*, (2004).

[Agn09] M. Agnello, E. Botta, T. Bressani, *et al.* Study of th eperformance of HP Ge detectors operating in very high magnetic fields. *Nuclear Instruments and Methods In Physics Research Section A*, **606**, 560 (2009).

[Ahm01] Q. R. Ahmad, R. C. Allen, T. C. Andersen, *et al.* Measurement of the Rate of $\nu_e + d \rightarrow p + p + e^-$ Interactions Produced by ^{8}B Solar Neutrinos at the Sudbury Neutrino Observatory. *Physical Review Letters*, **87**, 071301 (2001).

[Ahm02] Q. R. Ahmad, R. C. Allen, T. C. Andersen, *et al.* Direct Evidence for Neutrino Flavor Transformation from Neutral-Current Interactions in the Sudbury Neutrino Observatory. *Physical Review Letters*, **89**, 011302 (2002).

[Ahn06] M. H. Ahn, E. Aliu, S. Andringa, *et al.* Measurement of neutrino oscillation by the K2K experiment. *Physical Review D*, **74**, 072003 (2006).

[Aki97] H. Akimune, H. Ejiri, M. Fujiwara, *et al.* GT strengths studied by (^{3}He, t) reactions and nuclear matrix elements for double beta decays. *Physics Letters B*, **394**, 23 (1997).

[All90] S. Allison, P. Ramos, and G. Gillies. Microchannel plate intensifier response in transverse magneticfield. *Electronics Letters*, **26**, 770 (1990).

[Ame05] F. Ames, G. Bollen, P. Delahaye, *et al.* Cooling of radioactive ions with the Penning trap REXTRAP. *Nuclear Instruments and Methods In Physics Research Section A*, **538**, 17 (2005).

[And10] E. Andreotti, C. Arnaboldi, F. A. III, *et al.* Muon-induced backgrounds in the CUORICINO experiment. *Astroparticle Physics*, **34**, 18 (2010).

[Api10] Apiezon High Vacuum Sealants and Lubricants. Vacuum greases. http://www.apiezon.com/apiezon-vacuum-greases.htm (2010).

[Arn05] R. Arnold, C. Augier, J. Baker, *et al.* First Results of the Search for Neutrinoless Double-Beta Decay with the NEMO 3 Detector. *Physical Review Letters*, **95**, 182302 (2005).

[Arn08] C. Arnaboldi, D. R. Artusa, F. T. Avignone III, *et al.* Results from a search for the 0 $\nu\beta\beta$-decay of ^{130}Te. *Physical Review C*, **78**, 035502 (2008).

[Ash04] Y. Ashie, J. Hosaka, K. Ishihara, *et al.* Evidence for an Oscillatory Signature in Atmospheric Neutrino Oscillations. *Physical Review Letters*, **93**, 101801 (2004).

[Aud03] G. Audi, O. Bersillon, J. Blachot, and A. H. Wapstra. The evaluation of nuclear and decay properties. *Nuclear Physics A*, **729**, 3 (2003). The 2003 NUBASE and Atomic Mass Evaluations.

[Avi08] F. T. Avignone, III, S. R. Elliott, and J. Engel. Double beta decay, Majorana neutrinos, and neutrino mass. *Reviews of Modern Physics*, **80**, 481 (2008).

[Bar02] V. Bartsch, W. de Boer, J. Bol, *et al.* Lorentz angle measurements in silicon detectors. *Nuclear Instruments and Methods In Physics Research Section A*, **478**, 330 (2002).

[Bar09] J. Barea and F. Iachello. Neutrinoless double-beta decay in the microscopic interacting boson model. *Physical Review C*, **79**, 044301 (2009).

[Bar10a] A. Barabash. Double-beta decay: Present status. *Physics of Atomic Nuclei*, **73**, 162 (2010). 10.1134/S1063778810010187.

[Bar10b] A. S. Barabash. Precise half-life values for two-neutrino double-β decay. *Phys. Rev. C*, **81**, 035501 (2010).

[Ber09] M. Berger, J. Hubbell, S. Seltzer, *et al.* XCOM: Photon Cross Sections Database (2009).
URL `http://www.nist.gov/physlab/data/xcom/index.cfm`

[Bha98] M. Bhattacharya, A. García, M. M. Hindi, *et al.* Electron capture decay of ^{116}In and nuclear structure of double β decays. *Phys. Rev. C*, **58**, 1247 (1998).

[Bla06] K. Blaum. High-accuracy mass spectrometry with stored ions. *Physics Reports*, **425**, 1 (2006).

[Bla09] K. Blaum, S. Nagy, and G. Werth. High-accuracy Penning trap mass measurements with stored and cooled exotic ions. *Journal of Physics B: Atomic, Molecular and Optical Physics*, **42**, 154015 (2009).

[Boe00] W. Boer, de, V. Bartsch, J. Bol, *et al.* Lorentz angle measurements in irradiated silicon detectors between 77 K and 300 K. *arXiv:physics*, **0007059v2** (2000).

[Boe01] W. Boer, de, J. Bol, A. Dierlamm, *et al.* Lorentz angle measurements in irradiated silicon detectors between 77 and 300 K. *Nuclear Instruments and Methods In Physics Research Section A*, **461**, 200 (2001).

[Boh75] A. N. Bohr and B. R. Mottelson. *Nuclear Structure* (Reading, MA:Benjamin, 1975).

[Bol90] G. Bollen, R. Moore, G. Savard, and H. Stolzenberg. The accuracy of heavy-ion mass measurements using time of flight-ion cyclotron resonance in a Penning trap. *Journal of Applied Physics*, **68**, 4355 (1990).

[Bri08] P. Bricault, F. Ames, T. Achtzehn, *et al.* An overview on TRIUMF's developments on ion source for radioactive beams. *Review of Scientific Instruments*, **79**, 02A908 (2008).

[Bro82] L. S. Brown and G. Gabrielse. Precision spectroscopy of a charged particle in an imperfect Penning trap. *Phys. Rev. A*, **25**, 2423 (1982).

[Bro01] I. Bronstein, K. Semendjajew, G. Musiol, and H. Mühlig. *Taschenbuch der Mathematik* (Verlag Harri Detsch, 2001).

[Bro09] M. Brodeur, T. Brunner, C. Champagne, *et al.* New mass measurement of ^{6}Li and ppb-level systematic studies of the Penning trap mass spectrometer TITAN. *Phys. Rev. C*, **80**, 044318 (2009).

[Bro10a] M. Brodeur. First direct mass measurement of the two and four neutron halos ^{6}He and ^{8}He using the TITAN Penning trap mass spectrometer. Ph.D. thesis, University of British Columbia (2010).

[Bro10b] M. Brodeur. Private communication (2010).

[Bru08a] T. Brunner, M. Brodeur, C. Champagne, *et al.* Electron capture branching ratio measurements in an ion trap for double beta decay experiments at TITAN. *Nuclear Instruments and Methods In Physics Research Section B*, **266**, 4643 (2008).

[Bru08b] Brushwell. IF-1^{TM} Beryllium - Ultrahigh Purity Foil Specifications (2008).

[Bru09] T. Brunner, S. Ettenauer, and A. T. Gallant. tig10 performance report. Technical report, TRIUMF (2009).

[Bru10a] T. Brunner, M. Brodeur, P. Delheij, *et al.* In-trap decay spectroscopy for $2\nu\beta\beta$ decay experiments. *Hyperfine Interactions*, **submitted.** (2010).

[Bru10b] T. Brunner, M. Brodeur, S. Ettenauer, *et al.* Design of a β-detector for TITAN-EC and the first electron-capture branching ratio measurement in a Penning trap. *Journal of Physics: Conference Series*, **submitted** (2010).

[Bru10c] T. Brunner, M. Smith, M. Brodeur, *et al.* TITAN's Digital RFQ Ion Beam Cooler and Buncher. *Nuclear Instruments and Methods In Physics Research Section A*, **in preparation** (2010).

[Cana] Canberra. *Detector specifications and performance data for low energy Ge-detector, Model no. GUL0110P, Serial no. 08078301.*

[Canb] Canberra. *Edition Twelve Product Catalog.*

[Canc] Canberra. *Germanium Detector Chamber Typical Cross-Section View for low energy Ge-detector, Model no. GUL0110P, Serial no. 08078301.*

[Cand] Canberra. *Model no. GR2018, Serial no. 1086799.*

[Cane] Canberra. *Model no. GUL0110P, Serial no. 08078301.*

[Car09] C. D. Carone and R. F. Lebed. Optimal parametrization of deviations from the tribimaximal form of the neutrino mass matrix. *Phys. Rev. D*, **80**, 117301 (2009).

[Cau96] E. Caurier, F. Nowacki, A. Poves, and J. Retamosa. Shell Model Studies of the Double Beta Decays of ^{76}Ge, ^{82}Se, and ^{136}Xe. *Phys. Rev. Lett.*, **77**, 1954 (1996).

[Cau08] E. Caurier, J. Menéndez, F. Nowacki, and A. Poves. Influence of Pairing on the Nuclear Matrix Elements of the Neutrinoless beta beta Decays. *Physical Review Letters*, **100**, 052503 (2008).

[Cha08] K. Chaturvedi, R. Chandra, P. K. Rath, P. K. Raina, and J. G. Hirsch. Nuclear deformation and neutrinoless double-β decay of ^{94,96}Zr, ^{98,100}Mo, ^{104}Ru, ^{110}Pd, ^{128,130}Te, and ^{150}Nd nuclei within a mechanism involving neutrino mass. *Phys. Rev. C*, **78**, 054302 (2008).

[Cha09] R. Chandra, K. Chaturvedi, P. K. Rath, P. K. Raina, and J. G. Hirsch. Multipolar correlations and deformation effect on nuclear transition matrix elements of double-β decay. *EPL (Europhysics Letters)*, **86**, 32001 (2009).

[Che08] M. C. Chen for the SNO+ collaboration. The SNO+ Experiment. *arXiv:0810.3694v1 [hep-ex]*, (2008).

[Col82] C. I. Coleman. Effects of perturbing magnetic fields on the performance of photoelectronic sensors. *Review of Scientific Instruments*, **53**, 735 (1982).

[COM] COMSOL. Finite element simulation tool kit.

[Cow56] C. L. Cowan, Jr., F. Reines, F. B. Harrison, H. W. Kruse, and A. D. McGuire. Detection of the Free Neutrino: a Confirmation. *Science*, **124**, 103 (1956).

[Cow06] S. Cowell. Scaling factor inconsistencies in neutrinoless double beta decay. *Phys. Rev. C*, **73**, 028501 (2006).

[Cur03] F. J. Currell, editor. *The Physics of Multiply and Highly Charged Ions: Vol. 1: Sources, Applications and Fundamental Processes* (Springer, 2003), 1 edition.

[Dah00] D. A. Dahl. SIMION for the personal computer in reflection. *International Journal of Mass Spectrometry*, **200**, 3 (2000).

[Dan00] M. Danilov, R. DeVoe, A. Dolgolenko, *et al.* Detection of very small neutrino masses in double-beta decay using laser tagging. *Physics Letters B*, **480**, 12 (2000).

[Dav55] R. Davis. Attempt to Detect the Antineutrinos from a Nuclear Reactor by the $\mathrm{Cl}^{37}(\overline{\nu}, \overline{\mathrm{e}}^{-})\mathrm{A}^{37}$ Reaction. *Phys. Rev.*, **97**, 766 (1955).

[Daw95] P. Dawson, editor. *Quadrupole Mass Spectrometry and its Applications* (American Institute of Physics, New York (originally published by Elsevier, Amsterdam, 1976), 1995).

[Daw09] J. V. Dawson, C. Goessling, B. Janutta, *et al.* Experimental study of double-β decay modes using a CdZnTe detector array. *Phys. Rev. C*, **80**, 025502 (2009).

[Doi85] M. Doi, T. Kotani, and E. Takasugi. Double Beta Decay and Majorana Neutrino. *Progress of Theoretical Physics Supplement*, **83**, 1 (1985).

[Dom00] M. Dombsky, D. Bishop, P. Bricault, *et al.* Commissioning and initial operation of a radioactive beam ion source at ISAC. *Review of Scientific Instruments*, **71**, 978 (2000).

[Dom02] M. Dombsky, P. Bricault, T. Hodges, A. Hurst, and P. Schmor. Online isotope separation at ISAC with a 10 µA proton driver beam. *Nuclear Physics A*, **701**, 486 (2002).

[Dom05] P. Domin, S. Kovalenko, F. Simkovic, and S. Semenov. Neutrino accompanied $\beta^{\pm}\beta^{\pm}$, β^{+}/EC and EC/EC processes within single state dominance hypothesis. *Nuclear Physics A*, **753**, 337 (2005).

[Dro07] D. Drouin, A. R. Couture, D. Joly, *et al.* CASINO V2.42 - A Fast and Easy-to-use Modeling Tool for Scanning Electron Microscopy and Microanalysis Users. *Scanning*, **29**, 92 (2007).

[DuP01] DuPont Technical Information H-73241-2 (3/01) (2001).

[Ebe79] E. H. Eberhardt. Gain model for microchannel plates. *Applied Optics*, **18**, 1418 (1979).

[EBI08] *Articles summarizing 'The international workshop to mark the twentieth anniversary of the electron beam ion trap (EBIT)'*, volume 86 (Canadian Journal of Physics, 2008).

[Egu03] K. Eguchi, S. Enomoto, K. Furuno, *et al.* First Results from KamLAND: Evidence for Reactor Antineutrino Disappearance. *Phys. Rev. Lett.*, **90**, 021802 (2003).

[Ell87] S. R. Elliott, A. A. Hahn, and M. K. Moe. Direct evidence for two-neutrino double-beta decay in ^{82}Se. *Phys. Rev. Lett.*, **59**, 2020 (1987).

[Ell02] S. Elliott and P. Vogel. Double beta decay. *Annual Review of Nuclear and Particle Science*, **52**, 115 (2002).

[Eng88] J. Engel, P. Vogel, and M. R. Zirnbauer. Nuclear structure effects in double-beta decay. *Phys. Rev. C*, **37**, 731 (1988).

[Eng09] J. Engel and G. Hagen. Corrections to the neutrinoless double-beta-decay operator in the shell model. *Physical Review C*, **79**, 064317 (2009).

[Ett09] S. Ettenauer, T. Brunner, M. Brodeur, *et al.* In-trap decay spectroscopy of radioactive nuclei at titan/triumf for a determination of $2\nu\beta\beta$ matrix elements. *AIP Conference Proceedings*, **1182**, 100 (2009).

[Ett10a] S. Ettenauer. Private communication (2010).

[Ett10b] S. Ettenauer, M. Brodeur, T. Brunner, *et al.* Precision ground state mass of ^{12}Be and an isobaric multiplet mass equation (IMME) extrapolation for 2^+ and 2^+ states in the $T = 2$, $A = 12$ multiplet. *Phys. Rev. C*, **81**, 024314 (2010).

[Fan10] D.-L. Fang, A. Faessler, V. Rodin, and F. Šimkovic. Neutrinoless double-β decay of ^{150}Nd accounting for deformation. *Phys. Rev. C*, **82**, 051301 (2010).

[Fer34] E. Fermi. Versuch einer Theorie der β-Strahlen. I (An attempt of a theory of beta-decay). *Z.f.Physik*, **88**, 161 (1934).

[Flé08] X. Fléchard, E. Liénard, A. Méry, *et al.* Paul Trapping of Radioactive ^{6}He$^+$ Ions and Direct Observation of Their β Decay. *Phys. Rev. Lett.*, **101**, 212504 (2008).

[Fra90] G. Fraser. The gain, temporal resolution and magnetic-field immunity of microchannel plates. *Nuclear Instruments and Methods In Physics Research Section A*, **291**, 595 (1990).

[Fre07] D. Frekers, I. Tanihata, and J. Dilling. Electron capture branching ratios for the odd-odd intermediate nuclei in double-beta decay using the TITAN ion trap facility . *Canadian Journal of Physics*, **85**, 57 (2007).

[Fro91] T. Frommhold, W. Arnold, H. Friedrichs, *et al.* Response functions of Si detectors to monoenergetic electrons and positrons in the energy range 0.8-3.5 MeV. *Nuclear Instruments and Methods In Physics Research Section A*, **310**, 657 (1991).

[Fro06] M. Froese. Master's thesis, Department of Physics and Astronomy, University of Manitoba (2006).

[Fuk98] Y. Fukuda, T. Hayakawa, E. Ichihara, *et al.* Evidence for Oscillation of Atmospheric Neutrinos. *Phys. Rev. Lett.*, **81**, 1562 (1998).

[Fuk01] S. Fukuda, Y. Fukuda, M. Ishitsuka, *et al.* Solar ^{8}B and hep Neutrino Measurements from 1258 Days of Super-Kamiokande Data. *Phys. Rev. Lett.*, **86**, 5651 (2001).

[Fur39] W. H. Furry. On transition probabilities in double beta-disintegration. *Phys. Rev.*, **56**, 1184 (1939).

[Gar93] A. García, Y.-D. Chan, M. T. F. da Cruz, *et al.* Electron-capture decay of ^{100}Tc and the double-β decay of ^{100}Mo. *Phys. Rev. C*, **47**, 2910 (1993).

[GC10] J. Gómez-Cadenas, J. Martín-Albo, M. Sorel, *et al.* Sense and sensitivity of double beta decay experiments. *arXiv:1010.5112v2 [hep-ex]*, (2010).

[Geh07] V. M. Gehman and S. R. Elliott. Multiple-isotope comparison for determining $0\nu\beta\beta$ mechanisms. *Journal of Physics G: Nuclear and Particle Physics*, **34**, 667 (2007).

[Gho95] P. K. Ghosh. *Ion Traps* (Claredon Press, 1995).

[Gil01] J. Gillaspy, editor. *Trapping Highly Charged Ions: Fundamentals and Applications* (Nova Science Publishers, 2001).

[Gla56] R. J. Glauber and P. C. Martin. Radiative capture of orbital electrons. *Phys. Rev.*, **104**, 158 (1956).

[GM35] M. Goeppert-Mayer. Double beta-disintegration. *Phys. Rev.*, **48**, 512 (1935).

[Gre09] K. L. Green, P. E. Garrett, R. A. E. Austin, *et al.* Degeneracy at 1871 keV in ^{112}Cd and implications for neutrinoless double electron capture. *Phys. Rev. C*, **80**, 032502 (2009).

[Gus09] G. Gustafson. Private communication with Gus Gustafson (2009).

[Haa06] M. Haaks, T. Staab, and K. Maier. Analyzing the high-momentum part of positron annihilation Doppler spectra with a single germanium detector. *Nuclear Instruments and Methods In Physics Research Section A*, **569**, 829 (2006).

[Hal67] J. A. Halbleib and R. A. Sorensen. Gamow-Teller beta decay in heavy spherical nuclei and the unlike particle-hole RPA. *Nuclear Physics A*, **98**, 542 (1967).

[Hax84] W. C. Haxton and G. J. Stephenson. Double beta decay. *Progress in Particle and Nuclear Physics*, **12**, 409 (1984).

[Hel80] R. Helmer and M. Lee. Analytical functions for fitting peaks from ge semiconductor detectors. *Nuclear Instruments and Methods*, **178**, 499 (1980).

[Her01] F. Herfurth, J. Dilling, A. Kellerbauer, *et al.* A linear radiofrequency ion trap for accumulation, bunching, and emittance improvement of radioactive ion beams. *Nuclear Instruments and Methods In Physics Research Section A*, **469**, 254 (2001).

[Hir94] M. Hirsch, K. Muto, T. Oda, and H. V. Klapdor-Kleingrothaus. Nuclear structure calculation of $\beta^+\beta^+$, β^+/EC and EC/EC decay matrix elements. *Zeitschrift für Physik A Hadrons and Nuclei*, **347**, 151 (1994). 10.1007/BF01292371.

[Hor96] Y. S. Horowitz, Y. Weizman, and C. R. Hirning. A beta-ray spectrometer based on a two-or three silicon detector coincidence telescope. *Nuclear Instruments and Methods In Physics Research Section A*, **371**, 522 (1996).

[Ins] N. Instruments. Labview 8.6. Program.

[ISA08] ISAC operations Logbook Oct 31, 2008. Indium yield measurements (2008).

[Jen95] R. Jenkins, R. W. Gould, and D. Gedcke. *Quantitative X-ray Spectrometry* (Maecel Dekker, Inc., 1995).

[Kid08] M. F. Kidd, J. H. Esterline, and W. Tornow. Double-electron capture on ^{112}Sn to the excited 1871 keV state in ^{112}Cd: A possible alternative to double-beta decay. *Physical Review C*, **78**, 035504 (2008).

[Kim06] Y. Kim. The status of XMASS experiment. *Physics of Atomic Nuclei*, **69**, 1970 (2006). 10.1134/S106377880611024X.

[KK01] H. Klapdor-Kleingrothaus, A. Dietz, L. Baudis, *et al.* Latest results from the HEIDELBERG-MOSCOW double beta decay experiment. *The European Physical Journal A - Hadrons and Nuclei*, **12**, 147 (2001). 10.1007/s100500170022.

[KK04] H. V. Klapdor-Kleingrothaus, I. V. Krivosheina, A. Dietz, and O. Chkvorets. Search for neutrinoless double beta decay with enriched ^{76}Ge in Gran Sasso 1990-2003. *Physics Letters B*, **586**, 198 (2004).

[KK06] H. V. Klapdor-Kleingrothaus and I. V. Krivosheina. The Evidence for the Observation of $0\nu\beta\beta$ Decay:. the Identification of $0\nu\beta\beta$ Events from the Full Spectra. *Modern Physics Letters A*, **21**, 1547 (2006).

[Kno00] G. F. Knoll. *Radiation Detection and Measurement* (Wiley, 2000).

[Koe10] T. Koeppel. Helmholtz Coil - Wolfram Demonstraitons Project. http://demonstrations.wolfram.com/HelmholtzCoil/ (2010).

[Kol04] V. S. Kolhinen, S. Kopecky, T. Eronen, *et al.* JYFLTRAP: a cylindrical Penning trap for isobaric beam purification at IGISOL. *Nuclear Instruments and Methods In Physics Research Section A*, **528**, 776 (2004).

[Kön95] M. König, G. Bollen, H. J. Kluge, T. Otto, and J. Szerypo. Quadrupole excitation of stored ion motion at the true cyclotron frequency. *International Journal of Mass Spectrometry*, **142**, 95 (1995).

[Kra87] K. Krane. *Introductory Nuclear Physics* (Wiley, 1987).

[Kru00] K. Kruglov, L. Weissman, P. Van den Bergh, *et al.* A beam diagnostic system for low–intensity radioactive beams. *Nuclear Instruments and Methods In Physics Research Section A*, **441**, 595 (2000).

[Kun09] P. Kunz. ISAC-I yield measurements - ISAC e-log entry July 21, 2009 at 1:10am (2009).

[Kuo89] T. K. Kuo and J. Pantaleone. Neutrino oscillations in matter. *Reviews Of Modern Physics*, **61**, 937 (1989).

[Lap09] A. Lapierre. Private communication (2009).

[Lap10] A. Lapierre, M. Brodeur, T. Brunner, *et al.* The TITAN EBIT charge breeder for mass measurements on highly charged short-lived isotopes–First online operation. *Nuclear Instruments and Methods In Physics Research Section A*, **624**, 54 (2010).

[Leo08] D. Leonard, P. Grinberg, P. Weber, *et al.* Systematic study of trace radioactive impurities in candidate construction materials for EXO-200. *Nuclear Instruments and Methods In Physics Research Section A*, **591**, 490 (2008).

[Les08] E. L. Leslie Camilleri and J. F. Wilkerson. Neutrino masses and mixings: Status and prospects. *Annual Review of Nuclear and Particle Science*, **58**, 343 (2008).

[Lor07] A. S. Lorente, P. Achenbach, M. Agnello, *et al.* Performance of HPGe detectors in high magnetic fields. *Nuclear Instruments and Methods In Physics Research Section A*, **573**, 410 (2007).

[Maj37] E. Majorana. Teoria simmetrica dell'elettrone e del positrone. *Il Nuovo Cimento (1924-1942)*, **14**, 171 (1937). 10.1007/BF02961314.

[Maj04] F. Major, V. Gheorghe, and G. Werth. *Charged Particle Traps. Physics and Techniques of Charged Particle Field Confinement* (Springer, Berlin, 2004).

[Mak62] Z. Maki, M. Nakagawa, and S. Sakata. Remarks on the unified model of elementary particles. *Progress of Theoretical Physics*, **28**, 870 (1962).

[Man10] E. Mané, J. Behr, J. Billowes, *et al.* Collinear laser spectroscopy with reverse-extracted bunched beams at TRIUMF. *Hyperfine Interactions*, **submitted** (2010).

[Mar85] K. Marti and S. V. S. Murty. Double beta-decay half-life of ^{82}Se. *Physics Letters B*, **163**, 71 (1985).

[Mar08] J.-P. Martin, C. Mercier, N. Starinski, C. Pearson, and P.-A. Amaudruz. The TIGRESS DAQ/Trigger System. *Nuclear Science, IEEE Transactions on*, **55**, 84 (2008).

[Men09] J. Menéndez, A. Poves, E. Caurier, and F. Nowacki. Disassembling the nuclear matrix elements of the neutrinoless $\beta\beta$ decay. *Nuclear Physics A*, **818**, 139 (2009).

[Men10] J. Menendez, A. Poves, E. Caurier, and F. Nowacki. Novel Nuclear Structure Aspects of the Neutrinoless Double Beta Decay. *arXiv:1006.5631v3 [nucl-th]*, (2010).

[Mes01] A. P. Meshik, C. M. Hohenberg, O. V. Pravdivtseva, and Y. S. Kapusta. Weak decay of ^{130}Ba and ^{132}Ba: Geochemical measurements. *Physical Review C*, **64**, 035205 (2001).

[Mic06] D. G. Michael, P. Adamson, T. Alexopoulos, *et al.* Observation of muon neutrino disappearance with the minos detectors in the numi neutrino beam. *Phys. Rev. Lett.*, **97**, 191801 (2006).

[Mor40] P. Morrison and L. I. Schiff. Radiative K Capture. *Phys. Rev.*, **58**, 24 (1940).

[Mor09] O. Moreno, R. Álvarez-Rodríguez, P. Sarriguren, *et al.* Single- and low-lying-states dominance in two-neutrino double-beta decay. *Journal of Physics G: Nuclear and Particle Physics*, **36**, 015106 (2009).

[Mut88] K. Muto and H. V. Klapdor. Calculation of 2ν double beta decay of ^{76}Ge, ^{82}Se, ^{128,130}Te. *Physics Letters B*, **201**, 420 (1988).

[Nak10] K. Nakamura and P. D. Group. Review of particle physics. *Journal of Physics G: Nuclear and Particle Physics*, **37**, 075021 (2010).

[NND10] NNDC Chart of Nuclides (2010).
URL `http://www.nndc.bnl.gov/chart/`

[Ori] OriginLab. Origin 7.5. Data analysis program.

[Ott08] E. W. Otten and C. Weinheimer. Neutrino mass limit from tritium β decay. *Reports on Progress in Physics*, **71**, 086201 (2008).

[Ott10] E. Otten. Searching the absolute neutrino mass in tritium β-decay—interplay between nuclear, atomic and molecular physics. *Hyperfine Interactions*, **196**, 3 (2010). 10.1007/s10751-009-0150-2.

[Pac07] K. Pachucki, U. D. Jentschura, and M. Pfützner. Radiative orbital electron capture by the atomic nucleus. *Phys. Rev. C*, **75**, 055502 (2007).

[Pau30] W. Pauli. Pauli's letter 'Liebe Radioactive Damen und Herren'. http://www.library.ethz.ch/exhibit/pauli/neutrino_e.html (1930).

[Pau58] W. Paul, H. Reinhard, and U. von Zahn. Das elektrische Massenfilter als Massenspektrometer und Isotopentrenner. *Z. Phys. A*, , 143 (1958).

[Pon67] B. Pontecorvo. *Zh. Eksp. Teor. Fiz.*, **53**, 1717 (1967).

[Pov04] B. Povh, K. Rith, C. Scholz, and F. Zetsche. *Teilchen und Kerne* (Springer, 2004).

[Pri59] H. Primakoff and S. P. Rosen. Double beta decay. *Reports on Progress in Physics*, **22**, 121 (1959).

[Rad] D. Radford. Radware. Software package for interactive graphical analysis of gamma-ray coincidence data.

[Rad95] D. C. Radford. ESCL8R and LEVIT8R: Software for interactive graphical analysis of HPGe coincidence data sets. *Nuclear Instruments and Methods In Physics Research Section A*, **361**, 297 (1995).

[Rah09] S. Rahaman, V.-V. Elomaa, T. Eronen, *et al.* Accurate Q Value for the ^{112}Sn Double-β Decay and its Implication for the Search of the Neutrino Mass. *Phys. Rev. Lett.*, **103**, 042501 (2009).

[Rat09] P. K. Rath, R. Chandra, K. Chaturvedi, P. K. Raina, and J. G. Hirsch. Deformation effects and neutrinoless positron $\beta\beta$ decay of $Ru96$, $Pd102$, $Cd106$, $Xe124$, $Ba130$, and $Dy156$ isotopes within a mechanism involving Majorana neutrino mass. *Phys. Rev. C*, **80**, 044303 (2009).

[Rin07] R. Ringle, G. Bollen, A. Prinke, *et al.* A Lorentz steerer for ion injection into a Penning trap. *International Journal of Mass Spectrometry*, **263**, 38 (2007).

[Rin09] R. Ringle, M. Brodeur, T. Brunner, *et al.* High-precision Penning trap mass measurements of ^{9,10}Be and the one-neutron halo nuclide ^{11}Be. *Physics Letters B*, **675**, 170 (2009).

[Rod06] V. Rodin, A. Faessler, F. Šimkovic, and P. Vogel. Uncertainties in the $0\nu\beta\beta$-decay nuclear matrix elements. *Czechoslovak Journal of Physics*, **56**, 495 (2006). 10.1007/s10582-006-0113-7.

[Rod09] V. Rodin and A. Faessler. Can one measure nuclear matrix elements of neutrinoless double beta decay? *Physical Review C*, **80**, 041302 (2009).

[Rod10] T. R. Rodríguez and G. Martinez-Pinedo. Energy density functional study of nuclear matrix elements for neutrinoless $\beta\beta$ decay. *arXiv:1008.5260v1 [nucl-th]*, (2010).

[Ryj08] V. L. Ryjkov, M. Brodeur, T. Brunner, *et al.* Direct Mass Measurement of the Four-Neutron Halo Nuclide ^{8}He. *Physical Review Letters*, **101**, 012501 (2008).

[Sai91] T. Saito, Y. Kiwamoto, T. Honda, *et al.* Use of a silicon surface–barrier detector for measurement of high-energy end loss electrons in a tandem mirror. *Review of Scientific Instruments*, **62**, 2350 (1991).

[Sal08] F. Salvat, J. M. Fernández-Varea, and J. Sempau. PENELOPE-2008: A Code System for Monte Carlo Simulation of Electron and Photon Transport. *Workshop Proceedings, Barcelona, Spain*, (2008).

[Sav91] G. Savard, S. Becker, G. Bollen, *et al.* A new cooling technique for heavy ions in a Penning trap. *Physics Letters A*, **158**, 247 (1991).

[Sch82] J. Schechter and J. W. F. Valle. Neutrinoless double-β decay in SU(2)×U(1) theories. *Phys. Rev. D*, **25**, 2951 (1982).

[Sch96a] P. V. Schmidt, L. Willmann, R. Abela, *et al.* An efficient position sensitive detector for 3-30 keV positrons and electrons. *Nuclear Instruments and Methods In Physics Research Section A*, **376**, 139 (1996).

[Sch96b] E. Schönfeld and H. Janßen. Evaluation of atomic shell data. *Nuclear Instruments and Methods In Physics Research Section A*, **369**, 527 (1996).

[Sch00] E. Schönfeld and H. Janßen. Calculation of emission probabilities of X-rays and Auger electrons emitted in radioactive disintegration processes. *Applied Radiation and Isotopes*, **52**, 595 (2000).

[Sch08] S. Schwarz, G. Bollen, J. C. López-Urrutia, *et al.* An electron beam ion trap for the NSCL reaccelerator. *Nuclear Instruments and Methods In Physics Research Section B*, **266**, 4466 (2008). Proceedings of the XVth International Conference on Electromagnetic Isotope Separators and Techniques Related to their Applications.

[Sju08a] S. K. L. Sjue. The Electron-Capture Branch of ^{100}Tc and Implications for Neutrino Physics. Ph.D. thesis, University of Washington, Seattle (2008).

[Sju08b] S. K. L. Sjue, D. Melconian, A. García, *et al.* Electron-capture branch of ^{100}Tc and tests of nuclear wave functions for double-beta decays. *Physical Review C*, **78**, 064317 (2008).

[Sju09] S. K. L. Sjue and A. García. X-ray fitting code applying the method of maximum likelihood. Program developed at the University of Washington (2009).

[Sju10] S. K. L. Sjue. Fortran code to calculate a $\beta^{\pm}$ energy distribution. Fortran code (2010).

[Smi05] M. Smith. Master's thesis, University of British Columbia, Vancouver (2005).

[Smi06] M. Smith, L. Blomeley, P. Delheij, and J. Dilling. First tests of the TITAN digital RFQ beam cooler and buncher. *Hyperfine Interactions*, **173**, 0304 (2006).

[Smi08] M. Smith, M. Brodeur, T. Brunner, *et al.* First Penning-Trap Mass Measurement of the Exotic Halo Nucleus ^{11}Li. *Physical Review Letters*, **101**, 202501 (2008).

[Stö00] H. Stöcker. *Taschenbuch der Physik* (Verlag Harri Detsch, 2000).

[Str99] H. Straub, M. Mangan, B. Lindsay, K. Smith, and R. Stebbings. Absolute detection efficiency of a microchannel plate detector for kilo-electron volt energy ions. *Review of Scientific Instruments*, **70**, 4238 (1999).

[Suh88] J. Suhonen, T. Taigel, and A. Faessler. pnQRPA calculation of the β^+/EC quenching for several neutron-deficient nuclei in mass regions A = 94-110 and A =146-156*. *Nuclear Physics A*, **486**, 91 (1988).

[Suh98] J. Suhonen and O. Civitarese. Weak-interaction and nuclear-structure aspects of nuclear double beta decay. *Physics Reports*, **300**, 123 (1998).

[Suh05] J. Suhonen. Nuclear matrix elements of $\beta\beta$ decay from β-decay data. *Physics Letters B*, **607**, 87 (2005).

[Suj04] Z. Sujkowski and S. Wycech. Neutrinoless double electron capture: A tool to search for Majorana neutrinos. *Phys. Rev. C*, **70**, 052501 (2004).

[Szy08] K. Szymanska, P. Achenbach, M. Agnello, *et al.* Resolution, efficiency and stability of HPGe detector operating in a magnetic field at various gamma-ray energies. *Nuclear Instruments and Methods In Physics Research Section A*, **592**, 486 (2008).

[Tak84] E. Takasugi. Can the neutrinoless double beta decay take place in the case of Dirac neutrinos? *Physics Letters B*, **149**, 372 (1984).

[Ter08] A. Terashima, Y. Takemoto, E. Yonezawa, *et al.* R&D for possible future improvements of KamLAND. *Journal of Physics: Conference Series*, **120**, 052029 (2008).

[The] J. Theuerkauf, S. Esser, S. Krink, *et al.* Fitting software for photon spectra. Program Tv, Institute for Nuclear Physics, Cologne.

[The03] The Majorana collaboration. White Paper on the Majorana Zero-Neutrino Double-Beta Decay Experiment. *arXiv:nucl-ex/0311013v1*, (2003).

[Tho09] A. C. Thompson, D. T. Attwood, E. M., *et al.* The X-Ray Data Booklet (2009).
URL `http://xdb.lbl.gov/`

[Tor90] R. Tornow. A new method to measure and increase the detection efficiency of a microchannel plate for 100 keV electrons. *Measurement Science and Technology*, **1**, 576 (1990).

[Ume06] S. Umehara, T. Kishimoto, I. Ogawa, *et al.* CANDLES for double beta decay of ^{48}Ca. *Journal of Physics: Conference Series*, **39**, 356 (2006).

[VdB01] P. Van den Bergh, M. Huyse, K. Krouglov, P. Van Duppen, and L. Weissman. The REX-ISOLDE beam diagnostic system. *AIP Conference Proceedings*, **576**, 235 (2001).

[Vog08] P. Vogel. Nuclear physics aspects of double beta decay. *arXiv:0807.2457v1 [hep-ph]*, (2008).

[Š08] F. Šimkovic, A. Faessler, V. Rodin, P. Vogel, and J. Engel. Anatomy of the 0ν beta beta nuclear matrix elements. *Physical Review C*, **77**, 045503 (2008).

[Š09] F. Šimkovic, A. Faessler, H. Müther, V. Rodin, and M. Stauf. $^{0\nu\beta\beta}$-decay nuclear matrix elements with self-consistent short-range correlations. *Physical Review C*, **79**, 055501 (2009).

[Š10] F. Šimkovic. Private communication at the 'International Student Workshop on Neutrinoless Double Beta Decay', November 11-13, 2010 at LNGS (2010).

[vW35] C. F. v. Weizsäcker. Zur Theorie der Kernmassen. *Zeitschrift für Physik*, **96**, 431 (1935).

[Wal04] C. Waltham. Teaching neutrino oscillations. *American Journal of Physics*, **72**, 742 (2004).

[Wei01] L. Weissman, F. Ames, J. Äysto, *et al.* Feasibility of In-Trap Conversion Electron Spectroscopy. *Hyperfine Interactions*, **132**, 531 (2001).

[Wen03] K. D. A. Wendt, K. Blaum, C. Geppert, *et al.* Laser resonance ionization for efficient and selective ionization of rare species. *Nuclear Instruments and Methods In Physics Research Section B*, **204**, 325 (2003).

[Win55] R. G. Winter. Double K Capture and Single K Capture with Positron Emission. *Phys. Rev.*, **100**, 142 (1955).

[Wiz79] J. Wiza. Microchannel plate detectors. *Nuclear Instruments and Methods*, **162**, 587 (1979).

[Yao06] W.-M. Yao and et al. Review of Particle Physics. *Journal of Physics G: Nuclear and Particle Physics*, **33**, 1 (2006).

[You09] M. S. Yousef, V. Rodin, A. Faessler, and F. Šimkovic. Two-neutrino double beta decay of deformed nuclei within the quasiparticle random-phase approximation with a realistic interaction. *Physical Review C*, **79**, 014314 (2009).

[Zub04] K. Zuber. *Neutrino Physics. Series in High Energy Physics, Cosmology and Gravitation* (CRC Press, 2004).

Acknowledgement

This thesis would not exist without the help of many people. First of all, I would like to thank my supervisors Jens Dilling and Reiner Krücken for their help and support over the last four years. I enjoyed working on this project as part of the TITAN group and E12, with my colleagues Maxime Brodeur, Christian Champaign, Usman Chowdhury, Paul Delheij, Benjamin Eberhardt, Stephan Ettenauer, Aaron Gallant, Roman Gernhäuser, Alexander Grossheim, Martin Kossick, Alain Lapierre, Dave Lunney, Ernesto Mané, Ryan Ringle, Vladimir Ryjkov, Vanessa Simon, Martin Simon, Mathew Smith and Matt Pearson. A big thank you to them and the support groups at TRIUMF, especially Pierre Amaudruz and Chris Pearson. A special thanks to Mel Good for teaching me how to produce proper construction drawings, how to machine parts and many other things. Thanks to Smarajit Triambak for his help in setting up the Penelope code and Sky Sjue for his help with simulations, the analysis of the Cs data and many fruitful discussions. And a thanks to all the people I haven't mentioned.

In Vancouver, I stayed at the Orphanage most of the time. Stefan Albrecher, Thomas Fritz, Shawn Hood, and Bram van Straaten, thanks for all the great food you prepared for me and for the great time we spent together.

I also want to acknowledge the support of all my friends in Canada and Germany during my stay at the hospital and in the recovery process afterwards. Your friendship got me through this rough time.

Thank you Tiffany Angus, Maxime Brodeur, Kathrin Buchner, Jens Dilling, Aaron Gallant, Alexander Grossheim, Reiner Krücken, Alain Lapierre and Kai Zuber for their thorough reading as well as their input and corrections to this thesis.

Thanks to the 'Evangelisches Studienwerk Villigst, e.V.' for their financial support and the nice time I spent at Villigst. I always enjoyed my visits to Villigst.

Last but not least I want to thank my parents and siblings for their never-ending love and support.